

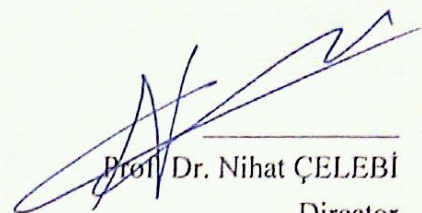
TIME EFFECTS IN Ag-DOPED $\text{YBa}_2\text{Cu}_3\text{O}_{7-x}$ CERAMIC SUPERCONDUCTORS
INDUCED BY THE APPLIED CURRENT AND MAGNETIC FIELD

by
ATILGAN ALTINKÖK

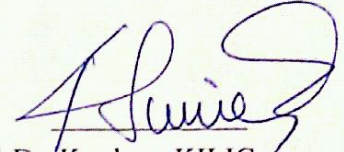
THESIS SUBMITTED TO
THE GRADUATE SCHOOL OF NATURAL AND APPLIED SCIENCES
OF
THE ABANT İZZET BAYSAL UNIVERSITY
IN PARTIAL FULFILLMENT OF THE REQUIREMENTS FOR THE DEGREE OF
DOCTOR OF PHILOSOPHY
IN
THE DEPARTMENT OF PHYSICS

SEPTEMBER 2011

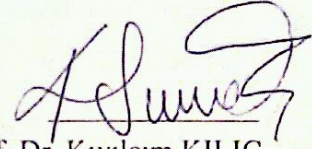
Approval of the Graduate School of Natural and Applied Science


Prof. Dr. Nihat ÇELEBİ
Director

I certify that this thesis satisfies all the requirements as a thesis for the degree of Doctor of Philosophy.

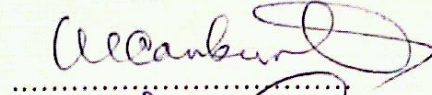

Prof. Dr. Kıvılcım KILIÇ
Head of Physics Department

This is to certify that we have read this thesis and that in our opinion it is fully adequate, in scope and quality, as a thesis for the degree of Doctor of Philosophy.

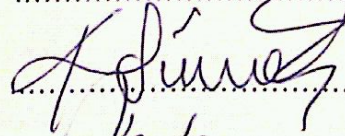

Prof. Dr. Kıvılcım KILIÇ
Supervisor

Examining Committee Members

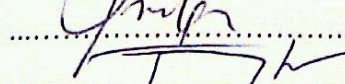
1- Prof. Dr. Mehmet CANKURTARAN



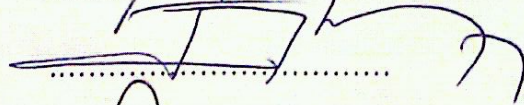
2- Prof. Dr. Kıvılcım KILIÇ



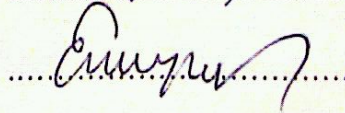
3- Prof. Dr. Atilla KILIÇ



4- Prof. Dr. Oktay ÇETİN



5- Doç. Dr. Ercan YILMAZ



ABSTRACT

TIME EFFECTS IN Ag-DOPED $\text{YBa}_2\text{Cu}_3\text{O}_{7-x}$ CERAMIC SUPERCONDUCTORS INDUCED BY THE APPLIED CURRENT AND MAGNETIC FIELD

Altinkök, Atılgan
Ph.D., Department of Physics
Supervisor: Prof. Dr. Kıvılcım KILIÇ

September 2011, 171 pages

In this thesis, current-voltage ($I - V$) curves with different sweeping rates (dI/dt) of transport current in Ag-doped $\text{YBa}_2\text{Cu}_3\text{O}_{7-x}$ sample (YBCO/Ag) were investigated. During the measurements, the transport current was cycled up and down. In addition, in measuring the $I - V$ curves, two different procedures were applied: Standard and reverse procedures. At moderate dissipation levels, we did not observe any difference between these two procedures. This experimental observation suggests that the surface effects are weakened by adding Ag into the superconducting matrix.

The time effects were investigated by means of transport relaxation measurements ($V - t$ curves). At well-defined values of transport current (I), temperature (T) and external magnetic field (H), an abrupt rise in the sample voltage was observed at

the early stage of the relaxation process. After reducing the initial current to a finite value, the sample voltage levels off within a very short time. The rapid voltage drops observed in the $V - t$ curves were attributed to the rapid dynamic reorganization of flux lines traversing the sample edges. These observations were also interpreted as easy suppression of superconducting order parameter due to the presence of Ag. As the transport current was reduced to a finite value, the time evolution of the quenched state YBCO/Ag is quite different from that of undoped YBCO. This difference in the $V - t$ curves was interpreted in terms of presence of Ag which destroys the order parameter in the whole sample.

We also investigated the influence of bi-directional square wave (BSW) current on the evolution of the $V - t$ curves at different periods (P), temperatures and external magnetic fields. The nonlinear voltage response seen in the $V - t$ curves to the BSW current with sufficiently short periods or sufficiently low amplitude reflects itself as regular sinusoidal-type voltage oscillations, which were discussed mainly in terms of the dynamic competition between pinning and depinning.

Magnetovoltage ($V - H$ curves) measurements were performed at selected values of the magnitude of transport current (I), temperature (T) and magnetic field-sweep rate (dH/dt) to investigate the intergranular region and weak-link profile. It was observed that there were clockwise (CW) hysteresis effects in the forward region (FR) of $V - H$ curves, and counterclockwise (CCW) effects in the reverse region (RR).

Keywords: Type-II superconductors, Ag-doped $\text{YBa}_2\text{Cu}_3\text{O}_{7-x}$, $I - V$ curves, magnetovoltage, transport relaxation curves, time effects, magnetic field effects, vortex dynamics.

ÖZET

Ag KATKILI $YBa_2Cu_3O_{7-x}$ SERAMİK SÜPERİLETKENLERDE UYGULANAN AKIM VE MAGNETİK ALAN TARAFINDAN İNDÜKLENEN ZAMAN ETKİLERİ

Altınkök, Atılğan
Doktora, Fizik Bölümü
Tez Danışmanı: Prof. Dr. Kıvılcım KILIÇ

Eylül 2011, 171 Sayfa

Bu tezde, gümüş (Ag) katkılı $YBa_2Cu_3O_{7-x}$ örnek (YBCO/Ag) üzerinde taşıma akımının farklı akım tarama hızlarında (dI/dt) akım-voltaj ($I - V$) eğrileri incelendi. Ölçümler süresince, taşıma akımı yukarı ve aşağı bir döngü içerisinde uygulandı. Buna ek olarak, $I - V$ eğrilerinin ölçümünde iki farklı yöntem uygulandı: Standart ve ters yöntem. Bununla birlikte, orta harcanım düzeyinde, bu iki yöntem arasında hiçbir fark gözlenmedi. Bu deneysel gözlem, YBCO süperiletken matrise gümüşün katılmasıyla, yüzey etkilerinin zayıfladığını işaret etmektedir.

Zaman etkileri, taşıma durulma ölçümleri ($V - t$ eğrileri) yardımıyla incelendi. Taşıma akımı (I), sıcaklık (T) ve uygulanan manyetik alanın (H) belirli

değerlerinde, durulma sürecinin başlangıcında Ag katkılı örneğin voltajında ani bir artış gözlemlendi. Başlangıç akımını sonlu bir değere azalttıktan sonra, örneğin voltajı çok kısa bir zaman içerisinde düştü. $V - t$ eğrilerinde görülen hızlı voltaj düşmesi örneği boydan boya geçen akı çizgilerinin hızlı dinamik yeniden organizasyonu ile ilişkilendirildi. Bu gözlemler, gümüşün varlığından dolayı YBCO' da süperiletken düzen parametresinin kolaylıkla bastırılmasına atfedildi. Taşıma akımı sonlu bir değere düşürüldüğünde, YBCO/Ag örneğinde, ani çakılma durumunun (quenched state) zamanla gelişiminin saf YBCO'dan oldukça farklı olduğu görüldü. $V - t$ eğrilerindeki bu farklılık, bütün örnek boyunca düzen parametresini bozan Ag'nin varlığına dayanarak yorumlandı.

Ayrıca $V - t$ eğrilerinin gelişimi üzerine iki yönlü kare dalganın (İKD) etkilerini farklı periyot (P), sıcaklık ve dış manyetik alan değerlerinde incelendik. Yeterince kısa periyotlu ve yeterince düşük genlikli İKD akımı uygulanarak ölçülen, $V - t$ eğrilerinde, lineer olmayan voltaj tepkisi düzgün sinüzoidal tipte voltaj osilasyonları olarak gözlemlendi. Bu deneysel gözlem akı tutulma (pinning) ve tutulmaması (de-pinnig) süreçleri arasındaki dinamik rekabete dayanılarak tartışıldı.

YBCO/Ag örnekte taneler arası bölgeyi ve zayıf eklem profilini incelemek için manyetovoltaj ölçümleri ($V - H$ eğrileri) taşıma akımının büyüklüğünün, sıcaklığın ve manyetik alan tarama hızının (dH/dt) fonksiyonu olarak ölçüldü. $V - H$ eğrilerinin ileri bölgesinde saat yönünde histerisis etkileri ve ters bölgesinde saat yönünün tersi histerisis etkileri gözlemlendi.

Anahtar Kelimeler: Tip-II süperiletkenler, Ag katkılı $\text{YBa}_2\text{Cu}_3\text{O}_{7-x}$, $I-V$ eğrileri, manyetovoltaj, taşıma durulma eğrileri, zaman etkileri, manyetik alan etkileri, akı dinamiği.

ACKNOWLEDGEMENTS

I would like to thank my supervisor Prof. Dr. Kıvılcım KILIÇ for her wisdom, knowledge, and commitment to high standards which have shaped the way I think scientifically and professionally. It has been an honor to be her Ph.D. student. I appreciate all her contributions and ideas.

I would like to thank Prof. Dr. Atilla KILIÇ for his encouragement, his helpful discussions. He has also trained me most of the equipment I used to complete this work. He has taught me consciously how good experimental physics is done.

I would like to thank Prof. Dr. Mehmet CANKURTARAN for valuable discussions and contributions to this work.

I would like to thank Prof. Dr. Oktay ÇETİN for his friendship and contributions. I am grateful to my colleagues, Assistant Prof. Dr. Hakan YETİŞ and Dr. Murat OLUTAŞ for their valuable supports and intimacy throughout my PhD works.

I would like to thank the supports of Prof. Dr. Ahmet VARILCI for XRD measurements and SEM images.

Finally, I would like to thank my wife Sevgi ALTINKÖK and my family for all their love and encouragement.

TABLE OF CONTENTS

ABSTRACT	iii
ÖZET	vi
ACKNOWLEDGEMENTS	ix
TABLE OF CONTENTS	x
LIST OF TABLES	xiii
LIST OF	xiv
FIGURES	
CHAPTER	
1. INTRODUCTION	1
2. SUPERCONDUCTIVITY	8
2.1 Basic Concepts of Superconductivity.....	8
2.1.1 Meissner effect.....	10
2.1.2 London theory.....	12
2.1.3 Type-I and type-II superconductors.....	15
2.1.4 The mixed state.....	18
2.2 Phenomenological Theories of Superconductivity.....	20
2.2.1 Ginzburg – Landau theory.....	20
2.2.2 BCS theory of superconductivity.....	22
2.3 Theoretical Models for Non-Linear Current–Voltage Measurements ($I-V$ curves)	24
2.3.1 Thermally assisted flux flow (TAFF), flux creep and flux flow in superconductors.....	25
2.3.2 Proximity effect.....	28

2.4	Transport Relaxation and Glassy State.....	29
2.5	Magnetoresistance in Granular Superconductors.....	31
2.5.1	The two-level magnetic system and intra- and inter-granular flux trapping model	31
2.6	YBa ₂ Cu ₃ O _{7-x} (YBCO-123) System	35
2.7	Grain Boundaries in YBCO.....	37
2.8	Effect of Doping Ag in YBCO-123.....	39
3.	EXPERIMENTAL TECHNIQUES.....	42
3.1	Sample Preperation.....	42
3.2	Structure Analysis.....	44
3.2.1	Scanning electron microscopy (SEM) and energy dispersive spectroscopy (EDS) of YBCO-123 samples	44
3.2.2	X-ray diffraction (XRD).....	46
3.3	Measurement Set-up.....	48
3.4	Current – Voltage Characteristics ($I - V$ curves) Measurements.....	50
3.5	Electrical Transport Relaxation ($V - t$ curves) Measurements.....	50
3.6	Magnetovoltage ($V - H$ curves) Measurements.....	51
4.	EXPERIMENTAL RESULTS.....	52
4.1	Resistivity versus Temperature Measurements on the Ag-Doped YBCO Sample.....	52
4.2	Current – Voltage ($I - V$ curves) Measurements.....	53
4.3	Time Effects and Transport Relaxation Measurements.....	69
4.3.1	Time evolution of the sample voltage ($V - t$ curves).....	69
4.3.2	The effect external magnetic field on the evolution of $V - t$ curves.....	75
4.4	Voltage Oscillations and Influence of Bidirectional Square Wave (BSW) Current on The Evolution of $V - t$ Curves.....	79
4.4.1	Influence of the period of BSW current on $V - t$ curves.....	79
4.5	Magnetovoltage Measurements ($V - H$ curves).....	83

4.5.1	Hysteresis effects in the $V - H$ curves measured at different sweep rates of the external magnetic field (dH/dt).....	84
5.	DISCUSSION	95
5.1	Current – Voltage Characteristics ($I - V$) Measurements.....	95
5.1.1	Flux dynamics and hysteresis effects.....	95
5.1.2	Instabilities in the $I - V$ curves: Voltage jumps and drops....	104
5.1.3	Reverse procedure in the $I - V$ curves	107
5.2	Transport Relaxation ($V - t$ curves) Measurements.....	112
5.2.1	Evolution of the $V - t$ curves of the YBCO/Ag sample.....	113
5.2.1.1	Time effects for $I_1 > I_2$	113
5.2.1.2	Time evolution of the quenched state created for $I_1 > I_2$	115
5.2.2	Current and magnetic field induced voltage oscillations.....	120
5.2.3	Relationship between the voltage oscillations and charge density waves.....	129
5.3	Magnetovoltage Measurements.....	130
5.3.1	Hysteresis effects in the $V - H$ curves and intra and intergranular flux trapping.....	133
6.	CONCLUSIONS	146
	REFERENCES	153
	CURRICULUM VITAE	168

LIST OF TABLES

TABLE

2.1	Main superconducting parameters of $\text{YBa}_2\text{Cu}_3\text{O}_{7-x}$ (YBCO-123) in the ab-plane and along the c-axis direction at zero temperature. ξ is the coherence length, λ the penetration length, J_c is the critical current density, and H_{c1} and H_{c2} are the lower and upper critical magnetic fields, respectively (data extracted from references [108-110]).....	37
3.1	The lattice parameters a , b and c for undoped and Ag-doped samples.....	47
3.2	The lattice parameters a , b and c for Ag-doped YBCO-123 samples (data extracted from ref. [130]).....	48
5.1	The phase angles ϕ obtained by fitting Eq. 5.6 to the $V-t$ data in Fig. 4.18.....	126
5.2	The phase angles ϕ obtained by fitting Eq. 5.6 to the $V-t$ data in Fig. 4.19.....	127
5.3	The phase angles ϕ obtained by fitting Eq. 5.6 to the $V-t$ data in Fig. 4.20.....	128

LIST OF FIGURES

FIGURE		
2.1	The Meissner effect. (a) Magnetic field applied at $H < H_c$ to a superconductor at the condition of $T > T_c$. (b) The magnetic field lines are excluded by the superconductor yielding $B = 0$ inside the superconductor as when both conditions of $H < H_c$ and $T < T_c$ are satisfied. Applied magnetic field lines are represented as arrows.....	11
2.2	Variation of magnetic flux density from the surface to the interior of a superconductor [88].....	14
2.3	Magnetic field dependence of magnetization for type-I superconductor [89].....	15
2.4	Magnetization of an ideal type-II superconductor. The $M - H$ curve is reversible upon cycling of H . The state of perfect diamagnetism exists below H_{c1} , whereas, for $H > H_{c2}$, the material is in the normal state. (b) Magnetization of a real type-II superconductor. The $M - H$ curve is reversible only above H_{irr} . The magnetic flux at $H = 0$ is “trapped” or “pinned” in the material [90].....	17
2.5	The mixed state, showing normal cores and encircling supercurrent (I_s) vortices. The vertical lines represent the flux threading the cores. The surface current maintains the bulk magnetism [91].....	19
2.6	Passing electron attracts the cation lattice, causing a distortion in the lattice [95].....	23
2.7	Another electron passing in the opposite direction is attracted to this lattice distortion (phonon): the electron-phonon interaction [95].....	23
2.8	A schematic representation of the $I - V$ curves (or $E - V$ curves) of superconductors. The curve has a linear region at low I , followed by a highly nonlinear region at intermediate values of I , and finally a linear relation again. The definition of I_c or J_c is given	

	on the curve by using the criterion of $V = 1 \mu\text{V}$, or $E = 1 \mu\text{V/cm}$ [97].....	25
2.9	Different stages of flux motion, depending on the magnitude of transport current J . The presence of current in a magnetic field generates a Lorentz force F_L which tilts the staircase allowing the flux lines to hop out of their wells more easily [98]. Here F_0 is the pinning force and x is the position of moving flux line system.....	27
2.10	Schematic plot for magnetovoltage ($V - H$ curve). The increasing and decreasing external magnetic fields corresponding to the same sample voltage value are labeled as H^+ and H^- , respectively. ΔH is the difference between H^+ and H^- for a given value of measured sample voltage. $\Delta H = H^- - H^+$ is the width of the hysteresis loop.....	34
2.11	Structures of (a) tetragonal $\text{YBa}_2\text{Cu}_3\text{O}_6$, (b) orthorhombic $\text{YBa}_2\text{Cu}_3\text{O}_7$ (xy is ab -plane, z is c -axis of the unit cell) [108].....	36
3.1	Schematic thermal profile of (a) sintering and (b) annealing of Ag doped YBCO-123 sample.....	43
3.2	SEM photomicrographs of (a) undoped and (b) 3 wt % Ag-doped polycrystalline YBCO-123 bulk samples. White shiny regions observed in SEM are the images of Ag. The magnification of SEM images is 1500.....	45
3.3	X – ray diffraction (XRD) patterns of (a) undoped, (b) Ag-doped YBCO-123 samples.....	47
3.4	Block diagram of the experimental set-up used in the measurements.....	49
4.1	The resistivity of the bulk polycrystalline YBCO/Ag sample as a function of temperature. The inset shows the derivative of resistivity with respect to temperature ($d\rho / dT$). ρ_g is defined as the grain boundary resistivity.....	53
4.2	The $I - V$ curves of the YBCO/Ag sample measured using the standard procedure with $dI/dt = 0.312 \text{ mA/s}$ and applied magnetic field $H = 10 \text{ mT}$ and 20 mT , at (a) $T = 85 \text{ K}$, (b) $T = 84 \text{ K}$, (c) $T = 82 \text{ K}$. The arrows show the direction of sweeping of the applied current. CI and CD with the arrows indicate the current-increase and current-decrease branches of the $I-V$ curves upon cycling of the transport current, respectively.....	54

4.3	The $I - V$ curves of the YBCO/Ag sample measured by the standard procedure at $T = 84$ K and $H = 10$ mT with (a) $dI/dt = 1.25$ mA/s, (b) $dI/dt = 0.625$ mA/s, and (c) $dI/dt = 0.312$ mA/s; at $T = 84$ K and $H = 20$ mT with (d) $dI/dt = 1.25$ mA/s, (e) $dI/dt = 0.625$ mA/s and (f) $dI/dt = 0.312$ mA/s. The arrows show the direction of sweeping of the applied current.....	56
4.4	The $I - V$ curves of the YBCO/Ag sample measured at $T = 84$ K and $H = 20$ mT by the standard procedure for (a) $dI/dt = 1.25$ mA/s, (b) $dI/dt = 0.625$ mA/s, and (c) $dI/dt = 0.312$ mA/s. The maximum current I_{\max} was 40 mA. The arrows show the direction of sweeping of the applied current.....	58
4.5	The $I - V$ curves of the YBCO/Ag sample measured at $T = 84$ K and $H = 20$ mT by the standard procedure for (a) $dI/dt = 1.25$ mA/s, (b) $dI/dt = 0.625$ mA/s, and (c) $dI/dt = 0.312$ mA/s. The maximum current I_{\max} was 50 mA. The arrows show the direction of sweeping of the applied current.....	60
4.6	The $I - V$ curves of the YBCO/Ag sample measured at $T = 82$ K by the standard procedure for $dI/dt = 1.25, 0.625$ and 0.312 mA/s at $H = 10$ mT (a)-(c) and at $H = 20$ mT (d)-(f) . The maximum current I_{\max} is taken as 40 mA. The arrows show the direction of sweeping of the applied current.....	61
4.7	The $I - V$ curves of the YBCO/Ag sample measured at $T = 84$ K by the reverse procedure for $dI/dt = 1.25, 0.625$ and 0.312 mA/s at $H = 10$ mT (a)-(c) and at $H = 20$ mT (d)-(f) . I_{\max} is taken as 20 mA. The arrows show the direction of sweeping of the applied current.....	63
4.8	The $I - V$ curves of the YBCO/Ag sample measured at $T = 82$ K and $H = 10$ mT by reverse procedure for (a) $dI/dt = 1.25$ mA/s, (b) $dI/dt = 0.625$ mA/s, (c) $dI/dt = 0.312$ mA/s. I_{\max} was 20 mA. The arrows show the direction of sweeping of the applied current.....	65
4.9	The $I - V$ curves of the YBCO/Ag sample measured at $T = 82$ K and $H = 10$ mT by reverse procedure for (a) $dI/dt = 1.25$ mA/s, (b) $dI/dt = 0.625$ mA/s, (c) $dI/dt = 0.312$ mA/s. I_{\max} was 30 mA. The arrows show the direction of sweeping of the applied current.....	66

4.10	The $I - V$ curves of the YBCO/Ag sample measured at $T = 82$ K by reverse procedure for $dI/dt = 1.25, 0.625$ and 0.312 mA/s at $H = 10$ mT (a)-(c) and at $H = 20$ mT (d)-(f) . I_{\max} is taken as 50 mA. The arrows show the direction of sweeping of the applied current.	68
4.11	The $V - t$ curves of the YBCO/Ag sample measured at $T = 89$ K and $H = 0$ for selected currents of I_2 with $I_1 = 50$ mA. The bold solid lines are, for $t > 60$ s, the curves calculated from Eq. 2.13 The inset shows a schematic representation of the driving current applied to the sample.....	70
4.12	The $V - t$ curves of the YBCO/Ag sample measured at $T = 89$ K and $H = 0$ for selected currents of I_2 with $I_1 = 40$ mA. Bold solid lines, for $t > 60$ s, are the curves calculated from Eq. 2.13. The inset shows a schematic representation of applied current.....	71
4.13	The $V - t$ curves of the YBCO/Ag sample measured at $T = 89$ K and $H = 0$ for selected currents $I_1 = 30$ mA and $I_2 = 10, 18, 22$ and 26. Bold solid line, for $t > 60$ s, is the curve calculated from Eq. 2.13. The inset shows a schematic representation of applied current.....	72
4.14(a)	The $V - t$ curves of the YBCO/Ag sample measured at $T = 88$ K and $H = 0$ for $I_2 = 46, 42, 38, 34, 30, 18,$ and 0 mA. The inset shows a schematic presentation of applied current. Bold solid lines are the curves calculated from Eq. 2.13	74
4.14(b)	The variation of critical time t_s with I_2 . The data are extracted from the $V - t$ curves given in Fig. 4.14(a). The full line through the experimental data is a guide for the eyes	74
4.15(a)	The $V - t$ curves of the YBCO/Ag sample measured at $T = 85$ K and $H = 10$ mT, for $I_1 = 20$ mA and $I_2 = 12$ and 16 mA. The bold solid line is calculated from Eq. 2.13.....	76
4.15(b)	The $V - t$ curves of the YBCO/Ag sample measured at $T = 85$ K and $H = 10$ mT, for $I_1 = 6$ mA and $I_2 = 4$ mA.	76
4.16	The $V - t$ curves of the YBCO/Ag sample measured at $T = 84$ K and $H = 10$ mT for $I_1 = 20$ mA and $I_2 = 12$ mA, and 16 mA. The bold solid line is calculated from Eq. 2.13.....	77
4.17	The $V - t$ curves of the YBCO/Ag sample measured at $T = 84$ K and $H = 14$ mT for $I_1 = 20$ mA and $I_2 = 4, 8, 12,$ and 16 mA....	78
4.18	Time evolution of the sample voltage measured for a BSW	

	current with amplitude $I = 15$ mA and period P_I : a) 10 s, b) 14s, c) 20 s, and d) 40 s. The measurements were made at $T = 89$ K and $H = 0$. The top panel shows schematically the BSW current applied to the sample.....	80
4.19	Time evolution of the sample voltage measured at $T = 89$ K and $H = 0$ for BSW current with fixed period of $P_I = 20$ s and different amplitudes a) $I = 16$ mA, b) $I = 18$ mA. The top panel represents schematically the BSW current applied to the sample.....	81
4.20	Time evolution of the sample voltage measured for BSW current (with amplitude $I = 4$ mA and period $P_I = 10$ s) at $T = 89$ K and external magnetic fields: a) $H = 10$ mT, b) $H = 16$ mT, and c) $H = 20$ mT. The top panel shows schematically BSW current.....	83
4.21(a)	Magnetovoltage ($V - H$) curves of the YBCO/Ag sample measured at $T = 88$ K for selected values of the transport current $I = 10, 15, 20, 30$ and 40 mA, with a fixed magnetic field sweep rate $dH/dt = 0.50$ mT/s. The arrows show the direction of sweeping of the external magnetic field.	85
4.21(b)	Replotted of magnetovoltage ($V - H$) curve given in Fig. 4.21(a) for better observation of the stages of hysteresis cycle. The current is taken as $I = 20$ mA.....	85
4.22	Magnetovoltage ($V - H$) curves of the YBCO/Ag sample measured at $T = 88$ K for selected values of the transport current $I = 10, 15, 20, 30$ and 40 mA, with a fixed magnetic field sweep rate $dH/dt = 1.30$ mT/s. The arrows show the direction of sweeping of the external magnetic field.	87
4.23	Magnetovoltage ($V - H$) curves of the YBCO/Ag sample measured at $T = 88$ K for selected values of the transport current $I = 10, 15, 20, 30$ and 40 mA, with a fixed magnetic field sweep rate $dH/dt = 2.60$ mT/s. The arrows show the direction of sweeping of the external magnetic field.	88
4.24	Magnetovoltage ($V - H$) curves of the YBCO/Ag sample measured at $T = 84$ K for $I = 30, 40, 50$ and 60 mA, and $dH/dt = 0.50$ mT/s. The arrows show the direction of sweeping of the external magnetic field.....	89
4.25	Magnetovoltage ($V - H$) curves of the YBCO/Ag sample measured at $T = 84$ K for $I = 20, 30, 40, 50$ and 60 mA, and $dH/dt = 1.30$ mT/s. The arrows show the direction of sweeping of the external magnetic field.....	89

4.26	Magnetovoltage ($V - H$) curves of the YBCO/Ag sample measured at $T = 84$ K for $I = 20, 30, 40, 50$ and 60 mA, and $dH/dt = 2.60$ mT/s. The arrows show the direction of sweeping of the external magnetic field.....	90
4.27	Magnetovoltage ($V - H$) curves of the YBCO/Ag sample measured at $T = 82$ K for $I = 20, 30, 40, 50$ and 60 mA, and $dH/dt = 0.50$ mT/s. The arrows show the direction of sweeping of the external magnetic field.....	91
4.28	Magnetovoltage ($V - H$) curves of the YBCO/Ag sample measured at $T = 82$ K for $I = 30, 40, 50$ and 60 mA and $dH/dt = 1.30$ mT/s. The arrows show the direction of sweeping of the external magnetic field.....	92
4.29	Magnetovoltage ($V - H$) curves of the YBCO/Ag sample measured at $T = 82$ K for $I = 20, 30, 40, 50$ and 60 mA and $dH/dt = 2.60$ mT/s. The arrows show the direction of sweeping of the external magnetic field.....	93
4.30	Magnetovoltage ($V - H$) curves of the undoped YBCO sample measured at $T = 82$ K for $I = 30, 40, 50, 60, 70$ and 75 mA and $dH/dt = 1.00$ mT/s. The arrows show the direction of sweeping of the external magnetic field [51].....	94
5.1	(a) Hysteresis effect observed in $I - V$ curve of polycrystalline sample of YBCO measured at $T = 88$ K and zero magnetic field for $dI/dt = 1.25$ mA/s (b) Hysteresis effect observed in $I - V$ curve of polycrystalline sample of MgB ₂ measured at $T = 34$ K and zero magnetic field for $dI/dt = 1.25$ mA/s [148, 149].....	103
5.2	Hysteresis effect observed in the $I - V$ curve of polycrystalline sample of undoped YBCO measured at $T = 85$ K and $H = 0$ for $dI/dt = 1.25$ mA/s [148].....	109
5.3	The $I - V$ curves of the undoped YBCO sample measured by the reverse procedure at $T = 84$ K, and $H = 10$ and 20 mT for (a) $dI/dt = 1.25$ mA/s (b) $dI/dt = 0.625$ mA/s. The arrows show the direction of sweeping of the applied current [28].....	110
5.4	Variation of the characteristic time t_0 with current I_2 . The values of t_0 were extracted from $V - t$ curves given in (a) Fig. 4.11, (b) Fig. 4.12 (c) Fig. 4.13. The dashed lines are a guide for the eyes..	117
5.5	The $V - t$ curve for the undoped YBCO sample measured at $T = 89$ K and $H = 0$ for $I_1 = 50$ mA and $I_2 = 34$ mA. The inset shows schematic presentation of the applied current. The bold solid line	

	is the curve calculated from Eq. 2.13. [28].....	120
5.6	Fast Fourier Transform (FFT) of the $V - t$ curves given in Fig. 4.18(a) – 4.18(c). The fundamental frequency is marked on each curve. The fundamental period $P_{Vosc, FFT}$ found from FFTs is given for each curve with the period of applied BSW currents.....	129
5.7	$\Delta H = f(H^-)$ curves of the YBCO/Ag sample determined at $T = 88$ K for different current values and magnetic field sweep rates of a) $dH/dt = 0.50$ mT/s b) $dH/dt = 1.30$ mT/s c) $dH/dt = 2.60$ mT/s. The data were extracted from the $V - H$ curves in Figs. 4.21-4.23.....	140
5.8	$\Delta H = f(H^-)$ curves of the YBCO/Ag sample determined at $T = 84$ K for different current values and magnetic field sweep rates a) $dH/dt = 0.50$ mT/s b) $dH/dt = 1.30$ mT/s c) $dH/dt = 2.60$ mT/s. The data were extracted from the $V - H$ curves in Figs. 4.24-4.26.....	142
5.9	$\Delta H = f(H^-)$ curves of the YBCO/Ag sample determined at $T = 82$ K for different current values and magnetic field sweep rates a) $dH/dt = 0.50$ mT/s b) $dH/dt = 1.30$ mT/s c) $dH/dt = 2.60$ mT/s. The data were extracted from the $V - H$ curves in Figs. 4.27-4.29.....	142
5.10	The variation of ΔH_{max} with dH/dt determined at different temperatures: a) $T = 88$ K, b) $T = 84$ K and c) $T = 82$ K. ΔH_{max} is the maximum value of the $\Delta H - H$ curves presented in Figs. 5.7-5.9.....	143
5.11	$\Delta H = f(H^-)$ curves of undoped the YBCO/Ag sample determined at $T = 82$ K for different current values and magnetic field sweep rate $dH/dt = 1.00$ mT/s. The data were extracted from the $V - H$ curves in Fig. 4.30.....	145

CHAPTER 1

INTRODUCTION

The pinning and motion of flux lines in a type-II superconductor are quite interesting and include many fascinating properties. The dynamic ordering and also the steady state properties of flux lines in a type-II superconductor can be probed via experimental techniques such as fast [1-10] and slow [11-14] transport measurements. Recent studies provide detailed understanding of the non-equilibrium physics [1, 2, 15], dynamic phase transitions [15-17], metastability [3, 5, 9, 18], and transient effects [3, 5] in type-II superconductors and have brought a new physical insight into the dynamic competition between the pinning and depinning. It has been demonstrated that the presence of weak disorder can promote the short-lived metastable states [12], whereas introducing of strong pinning centers may cause the formation of the long-lived ones, which can be probed by means of the fast transport measurements carried out on sufficiently short time scales [7]. Experimental observations reveal that the presence of strong metastability reflects itself as memory effects [19], history dependence [6], irreversibility [20, 21], current-induced annealing [12, 13, 22], and glassy state relaxation [3, 6, 19, 20]. The driving (transport) current can release the vortex system out of the metastable state and thus enable exploration of new accessible stable states in a distribution of energy landscape [6, 14].

In order to determine the current carrying capacity of superconductors, one way is to measure the current-voltage ($I - V$) curves. The measurements of $I - V$ curves also provide important information on the dissipation mechanisms in superconducting materials. In addition, the evolution of the $I - V$ curves exhibits several interesting features upon cycling the transport current. It was observed that significant instabilities such as voltage jumps and drops and hysteresis effects (which evolve as counterclockwise (ccw) or clockwise (cw) in character) could appear in the $I - V$ curves of type-II superconductors [3, 7, 21, 23-33]. Furthermore, depending on the sweep rate of the transport current (dI/dt), prominent time effects develop in the $I - V$ curves of superconductors at low and moderate dissipation levels [9, 11, 34-41]. Depending on the value of dI/dt , the decrease or increase in the height of hysteresis loop in the $I - V$ curves and the change in the measured dissipation are indications of the time effects. The current sweep rate dependence of the $I - V$ curves in high temperature superconductors (HTSCs) has been attributed to the presence of giant flux creep and high operating temperatures [41].

Recent transport relaxation ($V - t$ curves) studies [42-46] showed that there are remarkable time effects in transport measurements of type-II superconductors which deserve further investigation. The $V - t$ curves introduce a new method to monitor all details of flux dynamics evolving in the structure as the time progresses. The evolution of non-linear $V - t$ curves in polycrystalline samples of HTSCs is generally interpreted in terms of the formation of resistive and non-resistive flow channels and spatial re-organization of flux lines (or current-

induced flux lines) in a multiply connected network of weak-link structure [42, 43]. In other words, such a dynamic re-organization of flux lines causes an enhancement or suppression in the superconducting order parameter depending on the magnitude of the driving current and the coupling strength of weak-link structure with the chemical and anisotropic states of the sample.

On the other hand, recent experimental studies show that a quenched disorder in the moving entity (i.e., flux lines or current-induced flux lines) which is unstable in time can be created by interrupting the driving current [6, 14] or the applied magnetic field during the course of the experiment [47], and, thus, a non-equilibrium system can be obtained. The time evolution of the quenched state which shows many interesting properties can be investigated via $V - t$ measurements [3, 5, 6, 14]. It is observed that the relaxation of the quenched state reflects itself as a decaying response, which reminds the classical spin glasses, i.e., the glassy state relaxation [3, 5, 6, 14].

The flux lines in motion induced by different kinds of current modulations cause different motional re-organization in type-II superconductors. Fast transport measurements performed by using bi-directional square wave (BSW) currents showed nicely the current-driven re-ordering of vortices [48]. Gordeev *et al.* [2, 49] demonstrated experimentally that asymmetrical square wave currents cause slow voltage oscillations on long time scale in a de-twinned single-crystalline $Y_1Ba_2Cu_3O_{7-x}$ (YBCO) sample. A similar study on polycrystalline YBCO sample has been carried out by Kilic *et al.* [50] by using BSW current. They observed that

regular sinusoidal type oscillations evolve in well-defined ranges of amplitudes and periods of the BSW drive, and temperature.

Time effects were observed in the evolution of hysteresis loops in magnetoresistance (or magnetovoltage) measurements. The sweep rate of the applied magnetic field (dH/dt) plays a crucial role in this type of measurements, because it controls the number of the flux lines penetrating into the superconducting material [51, 52]. It is well known that strong irreversibilities appear in the magnetovoltage ($V - H$) curves upon cycling applied magnetic field. The hysteresis loops observed in the $V - H$ curves evolve generally in cw character and include the details of the pinning and depinning processes developed inside the material. We note that there is a close relation between the $V - H$ curves (resistivity technique) and magnetization ($M - H$) curves (magnetic technique) so that the same physical mechanisms should control the measured voltage dissipation [51, 52].

In granular superconductors, the two level critical state model [53] could explain successfully the irreversibility effects and the evolution of $V - H$ curves. In this model, it is assumed that the sample is composed of intergranular junction network and superconducting grains. The measured voltage dissipation is correlated to the flux motion and flux trapping evolving in both intergranular and intragranular regions, due to the magnitude of the applied magnetic field [51, 53-57].

In this thesis, the transport properties together with the time effects in silver (Ag) doped polycrystalline ceramic superconducting sample of $Y_1Ba_2Cu_3O_{7-x}$ (YBCO/Ag) were investigated. In the Ag-doped YBCO samples used in this study, the amount of Ag corresponds to 3 wt % of the weight of Cu in undoped YBCO compound. There are several reasons of doping YBCO with Ag. In 1990's, it was found that doping of YBCO with Ag is one of the best ways to improve the superconducting properties of $Y_1Ba_2Cu_3O_{7-x}$ [58-65]. It was shown that mechanical properties of YBCO could be improved [65-67] and its normal state resistivity could be reduced enormously [68, 69] by doping with Ag. In addition, the intergranular critical current density J_c was considerably increased by doping with Ag [70-72]. The experimental studies established that Ag diffuses into the grain boundary as a metal during thermal processing and it is responsible for the enhancement of coupling between the grains [64]. In other words, number of weak links in the structure is decreased by increasing the grain connectivity. The improvement in the grain structure of YBCO is strongly related to the amount of Ag added. Enough amount of Ag is responsible for providing interconnection between the grains by filling into the pores in the structure.

In order to understand the mechanisms of flux pinning and flux motion, systematic current–voltage ($I - V$ curves) measurements with various sweeping rates (dI/dt) of driving current were performed in YBCO/Ag in the neighborhood of the critical temperature T_c as functions of temperature (T), applied magnetic field (H), and maximum current driving I_{max} . Two different procedures; the standard procedure where the transport current (I) is cycled up and down (from

the zero to a max current value and then to the zero again) and the reverse procedure where I is cycled down and up (from a max current value to zero and then to the max current value again) were used to measure the $I - V$ curves. We note that the reverse procedure used in $I - V$ curves enables us to investigate the details of flux motion from the outer surface of the superconducting sample to its interior, i.e., the surface pinning effect.

The time effects induced by the driving current and magnetic field were investigated by means of voltage–time ($V - t$) curves in YBCO/Ag sample. The $V - t$ curves give all details of time evolution of organization of flux lines inside the sample and also average response of how the transport current distributes itself along sample. In the first part of transport relaxation measurements, the $V - t$ curves were measured for direct currents. In the second part, the influence of BSW current with various ranges of its amplitude and period on the flux dynamics was investigated in details at different temperatures and external magnetic fields. In order to understand the mechanisms of irreversible properties of YBCO/Ag, the magnetovoltage ($V - H$ curves) measurements with different sweeping rate dH/dt of external magnetic field were carried out at different temperatures below T_c by varying the transport current I .

Finally, for a better understanding of the influence of Ag on the superconducting properties, the experimental results obtained for YBCO/Ag were compared with those of undoped YBCO sample. Finally, we would like to note that experimental methods introduced in this thesis provide a useful tool to investigate how the

doping of Ag into the superconducting YBCO affects the flux dynamics and reorganization of transport current.

This thesis consists of six chapters, which provide the reader with a background on the subject before the experimental results are presented. The chapter 2 includes the basic properties of the superconductivity and the presentation of some of the pioneering theories of superconductivity. In chapter 3, the sample preparation of Ag doped YBCO and experimental set-up are given. This chapter also contains a description of the procedures used to perform the low temperature measurements and a detailed analysis of sample characterization, which includes scanning electron microscopy (SEM), energy dispersive spectroscopy (EDS) and x-ray diffraction (XRD), is given. In chapter 4, current–voltage characteristic ($I - V$) measurements, voltage–time ($V - t$) measurements, the effect of BSW driving current on $V - t$ curves and magnetovoltage ($V - H$) measurements are presented. In chapter 5, the experimental results are discussed. Finally in chapter 6, the experimental results and findings of this work are summarized.

CHAPTER 2

SUPERCONDUCTIVITY

2.1 Basic Concepts of Superconductivity

Superconductivity was first discovered in Hg (at a critical temperature of $T_c = 4.2$ K) as a sudden disappearance of measurable electrical resistance. The discovery was made in 1911 by the Kamerlingh Onnes group [73] when studying the low temperature behavior of pure metals. The new state observed in mercury was called as superconducting state. Afterwards, it was discovered that many other metallic elements exhibit superconductivity at very low temperatures. However, the industrial applications of these low critical temperature (T_c) superconductors (LTSCs) were restricted by the cost of the liquid helium and the complicated operation of the cooling system. After twenty two years later, another intrinsic property of a superconductor was called as the Meissner effect which is the exclusion of external magnetic field from the interior of the superconductor, i.e., perfect diamagnetism discovered by the Meissner and Ochsenfeld [74].

In the 1920s and 1930s, new superconducting alloys and compounds were discovered. In 1957, in a theoretical study of the effects of applied magnetic field on superconductors, Abrikosov [75] discovered that there are two types of superconductors: Type-I, where the magnetic flux is completely expelled from the

interior of the superconducting sample for values less than a critical magnetic field value H_c ; and type-II, where the magnetic flux is completely expelled for small fields (below H_{c1}) and partially in higher external fields (up to H_{c2}). Such a state in type-II superconductor is called as mixed state or vortex state.

The critical temperatures remained rather low as ~ 23 K in Nb_3Ge [76] until 1986. In 1986, Bednorz and Muller discovered high T_c superconductivity in the ceramic material of La-Ba-Cu-O [77]. They found evidence for superconductivity at about 30 K in LaBaCuO ceramics. In February 1987, Wu and Chu discovered superconductivity in $YBa_2Cu_3O_{7-x}$ ceramics with a T_c of about 90 K [78]. This was the existence of a superconductor with a critical temperature above that of liquid nitrogen, which is much cheaper coolant than the liquid helium. In 1988, $Bi_2Sr_2Ca_2Cu_3O_{10}$, $Tl_2Ba_2Ca_2Cu_3O_{10}$ and; in 1993, $HgBa_2Ca_2Cu_3O_8$ cuprate oxides were discovered with $T_c \approx 110$ K, 120 K, and 134 K, respectively [79-81]. The $HgBa_2Ca_2Cu_3O_{8+x}$ compound under 15 GPa hydrostatic pressure shows the onset of superconductivity at 164 K, the highest T_c known today [82]. Thus a new class of materials, copper oxide ceramics with a layered perovskite structure had rapidly arisen. In 2001, a new intermetallic superconductor was discovered by Nagamatsu *et al.* [83]: The magnesium diboride MgB_2 with $T_c = 39$ K. Further, newly found Fe-based superconductors have T_c above 30 K, for instance, $Sr_{0.5}Sm_{0.5}FeAsF$ has a T_c of 56 K [84].

2.1.1 Meissner effect

In 1933, Meissner and Ochsenfeld measured the flux distribution of metal superconductors cooled down to their T_c in an external magnetic field (H). They found out that a material in the superconducting state never allows the magnetic field lines to exist in its interior provided that the external magnetic field (H) is less than a critical field value H_c and it exhibits perfect diamagnetism, i.e., $B = 0$, where B is the magnetic induction inside the sample [85].

This property could not be explained by the basic properties of perfect conductors and therefore was called as *Meissner effect*. The magnetic behavior of a superconductor in an external magnetic field is shown in Fig. 2.1. The expulsion of applied magnetic field lines is a result of the existence of induced circulating currents in a superconductor which generate an induced magnetic field opposite in direction, but equal in magnitude to the external field H , so that the total magnetic induction inside the superconductor is zero. The state of *perfect diamagnetism* evolves at the conditions only if $T < T_c$ and $H < H_c$. The pattern of the external magnetic field lines depends on the shape of the specimen, which is characterized by the demagnetizing factor N_D of the geometry.

The magnetic induction B inside a magnetic material can be written as [86]

$$\vec{B} = \mu_0 (\vec{H} + \vec{M}) \quad (\text{in SI units}). \quad (2.1)$$

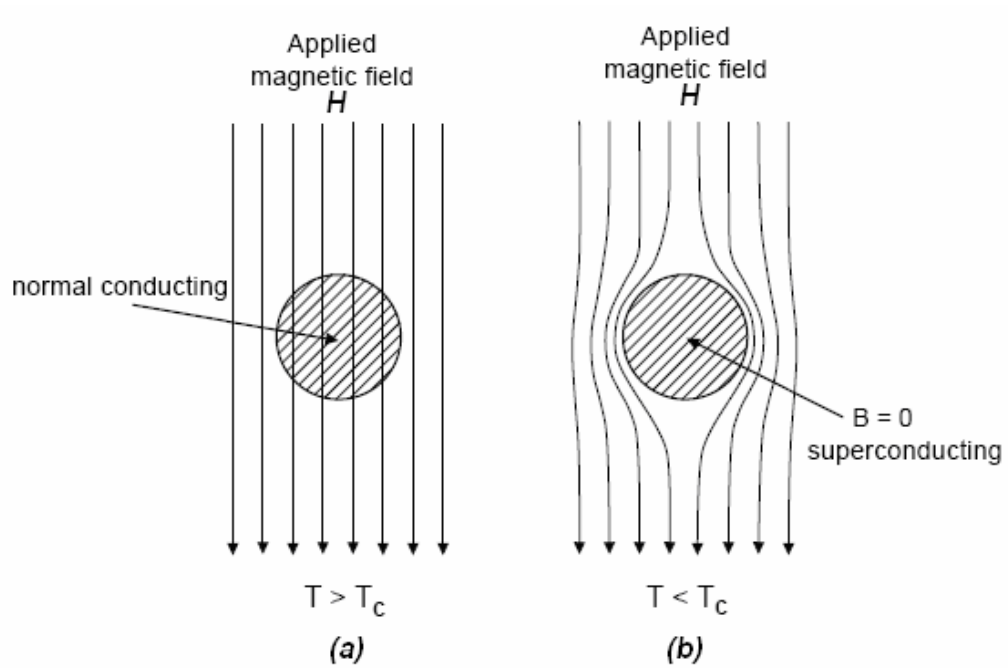


Figure 2.1 The Meissner effect. **(a)** Magnetic field applied at $H < H_c$ to a superconductor at the condition $T > T_c$. **(b)** The magnetic field lines are excluded by the superconductor yielding $B = 0$ inside the superconductor when both conditions $H < H_c$ and $T < T_c$ are satisfied. Applied magnetic field lines are represented as arrows.

Here, μ_0 is the magnetic permeability in vacuum, \vec{H} is the external magnetic field and \vec{M} is the magnetization of the sample. In the Meissner state, since the magnetic induction inside the superconductor is zero, Eq. 2.1 can be written as

$$M = \chi H = -H \quad (\text{in SI units}). \quad (2.2)$$

Here, χ is defined as magnetic susceptibility M/H and thus,

$$\chi = -1. \quad (2.3)$$

The result of $\chi = -1$ is a measure of perfect diamagnetism and therefore, it can be concluded that type-I superconductors are perfect diamagnetic materials at the conditions of $H < H_c$ and $T < T_c$.

2.1.2 London theory

The Meissner effect was explained by London [87]. He showed that the Meissner state can be described in terms of supercurrents (J_s) circulating in a thin surface layer of the superconductor which opposes to the external magnetic field. The thickness of this surface layer turned out to be a temperature-dependent material parameter called the London penetration depth, λ_L . The external magnetic field is thus allowed to penetrate in a distance of order of λ_L into the superconductor. The London equations describing perfect conductivity and flux expulsion are given by [86]

$$\frac{\partial}{\partial t} \vec{J}_s = \frac{n_s e^2}{m} \vec{E} = \frac{1}{\mu_0 \lambda_L^2} \vec{E} \quad (2.4)$$

and

$$\nabla \times \vec{J}_s = -\frac{1}{\mu_0 \lambda_L^2} \vec{B}, \quad (2.5)$$

where

$$\lambda_L = \sqrt{\frac{m_e}{\mu_0 n_s e^2}}. \quad (2.6)$$

Here, \vec{J}_s is supercurrent density, \vec{E} is the local electrical field and \vec{B} is the total magnetic induction. The parameters m_e , n_s , e are the mass, charge density and charge of superelectrons, respectively. As mentioned above, λ_L is a temperature

dependent parameter, i.e, $\lambda_L(T) \cong \lambda_L(0) \left[1 - \left(\frac{T}{T_c} \right)^4 \right]^{-1/2}$ for $T \leq T_c$. The penetration

depth diverges at the critical temperature, indicating that the number of superconducting charge carriers goes to zero at T_c .

By using Eq. 2.5 and the Maxwell equation $\vec{\nabla} \times \vec{B} = \mu_0 \vec{J}$ [86], we can obtain

$$\nabla^2 \vec{B} - \frac{1}{\lambda_L^2} \vec{B} = 0. \quad (2.7)$$

Equation 2.7 can be solved in one dimension for a semi-infinite superconductor in the shape of rectangular prism in a field parallel to its cross section area by using suitable boundary conditions. The local field penetrated into the superconductor can be found as

$$B(x) = B(0) \exp\left(-\frac{x}{\lambda_L}\right), \quad (2.8)$$

where $B(x)$ is the magnetic flux density at a distance x inside the metal, $B(0)$ is the flux density at the surface of the sample. Note that at the surface of the sample $B(x = 0) = H$. The position dependence of magnetic induction given in Eq. 2.8 is shown in Figure 2.2.

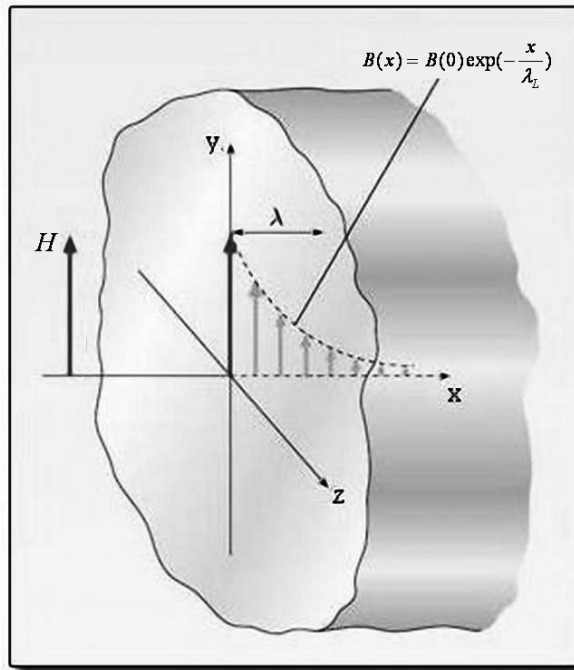


Figure 2.2 Variation of magnetic flux density from the surface to the interior of a superconductor [88].

The London equations predict an exponential decay of the flux density from the surface of a superconductor to its interior and also describe many features of the superconducting state well, but they do not explain why a material becomes superconducting.

2.1.3 Type-I and type-II superconductors

There are two kinds of superconductors namely type-I and type-II, which are classified with respect to their magnetic properties. The magnetization of a type-I superconductor is shown in Figure 2.3 [89]. When the external magnetic field H is lower than the critical field H_c , the magnetization is given by $M = -H$ (see Eq. 2.2) and the superconductor shows perfect diamagnetism (the Meissner state): $B = 0$. The transition from the superconducting state to the normal state occurs at $H = H_c$ with a discontinuous variation in the magnetization to $M = 0$ when $B = \mu_0 H$.

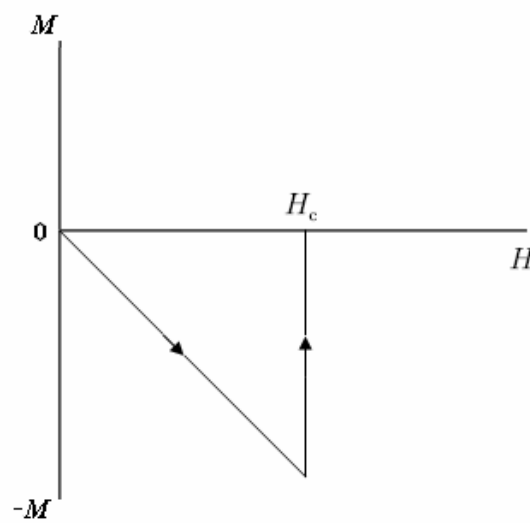


Figure 2.3 Magnetic field dependence of magnetization for type-I superconductor [89].

In 1957, Abrikosov published a paper describing some new phenomena related to the Ginzburg-Landau theory, quite different from the behavior of type-I superconductors [75]. He pointed out the existence of some new materials which exhibit a continuous increase in flux penetration starting at a first critical field H_{c1}

by reaching $B = \mu_0 H$ at a second critical field H_{c2} , instead of showing a discontinuous disappearance of superconductivity at the thermo-dynamical critical field H_c . Later, it was understood that the behavior of these materials could not be described simply due to impurities in their chemical composition. The experimental studies showed that they possess entirely new and different electric and magnetic properties and therefore, they were called as type-II superconductors [52].

Figure 2.4(a) shows that, in an idealized type-II superconductor, \vec{B} , \vec{H} , and \vec{M} are uniquely related to one another [89]. According to this figure, the state of perfect diamagnetism, $\vec{B} = \mu_0(\vec{H} + \vec{M}) = 0$, exists only below H_{c1} . For $H > H_{c1}$, the flux lines start to penetrate into the structure in a complicated way. As $H > H_{c2}$, the magnetization becomes totally zero so that the magnetic fields inside and outside the material are equal to each other and the material returns to its normal state. As the magnetic field is decreased slowly below H_{c2} , the reverse magnetization path will exactly retrace the forward one. However, no real material exhibits the exact retracing of such an idealized curve. Structural imperfections, chemical impurities and anisotropic states of the material act as barriers for both flux entry and exit through the material, referred to as flux pinning, and bring strong irreversibilities in the $M - H$ curves [52].

A real type-II superconductor has a more complicated magnetization curve, which is shown in Figure 2.4(b). A noticeable difference is the absence of sudden change in magnetization M as H passes through H_{c1} . Only the slight deviation from

linearity of the $M - H$ curve is a measure of that the diamagnetic state is no longer perfect and χ is less than -1. In this case, it can be suggested that the magnetic flux lines have already started to penetrate into the material. The increase of H leads to more extensive flux penetration, and, at H_{c2} , the state of full penetration is achieved: $B = \mu_0 H$ and the material becomes normal.

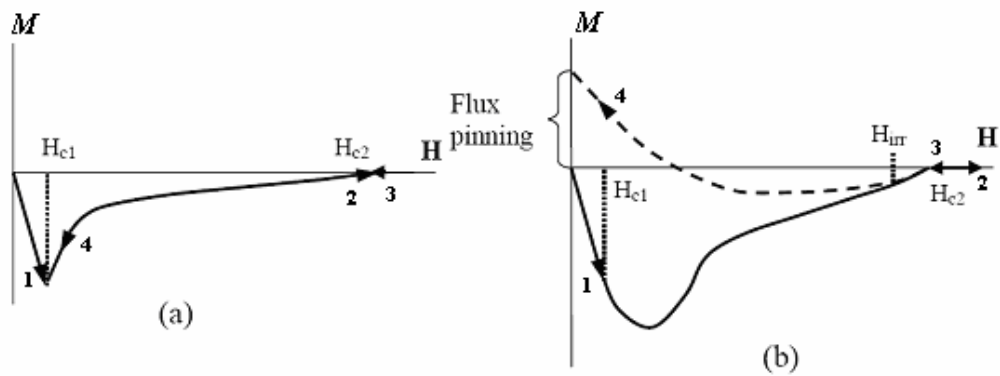


Figure 2.4 (a) Magnetization of an ideal type-II superconductor. The $M - H$ curve is reversible upon cycling of H . The state of perfect diamagnetism exists below H_{c1} , whereas, for $H > H_{c2}$, the material is in the normal state. **(b)** Magnetization of a real type-II superconductor. The $M - H$ curve is reversible only above H_{irr} . The magnetic flux at $H = 0$ is “trapped” or “pinned” in the material [90]. Numbers show different branches of the magnetization curve.

In the superconducting state, some of the flux lines are trapped within the material due to the presence of the imperfections and defects. When H is reduced from H_{c2} , the flux lines are free to move at first, and, so, the $M - H$ curve retraces its path until a field point H_{irr} referred to as *irreversibility field* [52]. When the flux pinning becomes stronger, B declines slower than the variation of H , and, M deviates from the forward curve. As H is further decreased, B remains high due to

the large flux pinning evolving inside sample and further, since $B = \mu_0(H+M)$, M rises to a positive value. At the end of the reverse cycle, when $H = 0$, the value of B remains finite due to the magnetic flux trapped by the superconductor

While the type-I superconductors are composed entirely of the metallic elements, type-II superconductors may be metal alloys or even some pure metals such as Niobium (Nb) and Vanadium (V), and also oxide compounds. Most metals and metal alloys have their critical temperature T_c below 25 K and are referred to as *low temperature superconductors* (LTSCs), while oxide superconductors (cuprates), MgB_2 and newly found Fe-based superconductors have their T_c above 30 K and are referred to as *high temperature superconductors* (HTSCs).

2.1.4 The mixed state

Structural imperfections or chemical impurities inside the superconducting material act as barriers for flux motion and this case is called as *flux pinning*. Apart from the normal and superconducting states, type-II superconductors exhibit a new state called the mixed state (or vortex state), which allows the existence of normal regions in the material. In the mixed state, the Meissner effect is no longer present and the magnetic flux may penetrate partially the superconductor. However, the superconductivity does not disappear completely. The existence of the mixed state can be explained by the fact that the material tries to keep itself in a state with the lowest total free energy. When the surface energy between the normal and superconducting regions is negative, the appearance of

normal regions will reduce the total free energy and lead to more favorable energy states [91]. The mixed state is an intrinsic feature of type-II superconductors and exists for magnetic fields such that $H_{c1} < H < H_{c2}$. It was predicted by Abrikosov [75] that the magnetic flux would penetrate the sample in a regular array of flux tubes, named *fluxons*, each one having the quantum of flux

$$\phi_0 = \frac{h}{2e} = 2.6678 \times 10^{-15} \text{ Wb} \text{ (} h \text{: Planck's constant and } e \text{: electron charge). Figure$$

2.5 shows the mixed state of a superconductor at $H_{c1} < H < H_{c2}$.

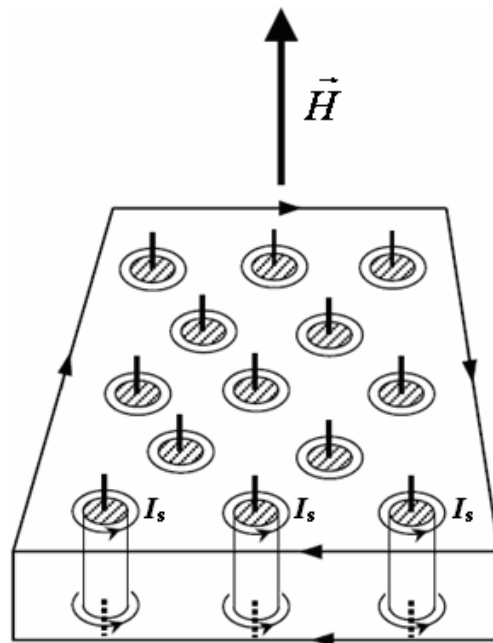


Figure 2.5 The mixed state, showing normal cores and encircling supercurrent (I_s) vortices. The vertical lines represent the flux threading the cores. The surface current maintains the bulk magnetism. [91]

The flux tubes forming in the shape of cylinder parallel to the external magnetic field thread the superconductor and include normal regions. These cylindrical normal cores are arranged in a regular pattern forming a lattice called as “flux line

lattice”. Within each core of flux tube, the magnetic flux has the same direction as that of the applied magnetic field and is shielded from the neighboring superconducting regions by a circulating induced current I_s . These supercurrents together with the surface current circulating at the perimeter of specimen maintain the bulk diamagnetism as shown in Fig. 2.5.

2. 2 Phenomenological Theories of Superconductivity

2.2.1 Ginzburg – Landau theory

Although the London theory explains the Meissner effect, it is unable to explain the coexistence of the normal and superconducting states in the mixed state of type-II superconductors. Ginzburg – Landau (G – L) theory is one of the phenomenological theories, which describes many properties of the superconductors. The G – L theory was based on the Landau theory of second order phase transitions [92]. It considers a phenomenological Hamiltonian which depends only on the symmetries of the system together with an order parameter taken into account. In this theory, it is assumed that a macroscopic wave function $\psi(r)$ is taken to be equivalent to order parameter and the free energy of the superconductor is expressed in terms of $\psi(r)$. In addition, it is assumed that $|\psi|^2$ is equal to the density of the Cooper pairs n_s . The free energy f of a superconductor can be written as

$$f_s = f_n + \alpha|\psi|^2 + \beta|\psi|^4 + \varepsilon|(-i\hbar\nabla + e^* A)\psi|^2, \quad (2.9)$$

where the subscripts n and s refer to normal and superconducting states, respectively, α , β and ε are phenomenological parameters. The behavior of free energy near the critical temperature T_c requires that α and β are temperature-dependent parameters. Conventionally ε is taken as $1/2(m_e)$ and e^* is the effective charge (which turns out to be twice the electronic charge). Minimizing Eq. 2.9 with respect to $\psi(r)$ over all space gives

$$\frac{1}{2m_e}(-i\hbar\nabla + e^* A)^2\psi + (\alpha + \beta|\psi|^2)\psi = 0. \quad (2.10)$$

Eq. 2.10 is known as Schrödinger-like Ginzburg – Landau equation and also defines a characteristic length depending on the variation of the order parameter $|\psi|^2$. This characteristic length is known as the coherence length $\xi(T)$ which depends on temperature. The Ginzburg–Landau coherence length ξ_{GL} is given as

$$\xi_{GL} = \sqrt{\frac{\hbar^2}{2m_e|\alpha|}}. \text{ On the other hand, minimizing Eq. 2.9 with respect to vector}$$

potential A gives a relation associated with supercurrent density J_s :

$$J_s = \frac{q^*}{m^*} \text{Re} \left\{ \Psi^*(\mathbf{r}) \left(\frac{\hbar}{i} \nabla - q^* \mathbf{A} \right) \Psi(\mathbf{r}) \right\}. \quad (2.11)$$

Here the pair charge and mass are $q^* = 2e$ and $m^* = 2m$, Re denotes the real part.

Another length scale which is referred to penetration depth $\lambda(T)$ can be found

from Eq. 2.11. The Ginzburg – Landau penetration depth (λ_{GL}) which depends on

temperature is given as
$$\lambda_{GL} = \sqrt{\frac{m_e \beta}{4\mu_0 e^2 |\alpha|}}.$$

The G–L parameter which classifies the superconductors is defined as $\kappa = \lambda_{GL}(T)/\xi_{GL}(T)$. The ratio $\kappa = \lambda_{GL}(T)/\xi_{GL}(T)$ determines whether the superconducting material behaves as a type-I ($\kappa < 1/\sqrt{2}$) or type-II superconductor ($\kappa > 1/\sqrt{2}$) [86].

2.2.2 BCS theory of superconductivity

The properties of type-I superconductors were modeled by a theory developed by Bardeen, Cooper, and Schrieffer in the 1950's [93]. In this theory, it was assumed that, at $T < T_c$ and $H < H_c$, an attractive force exists between electrons so that electrons can travel through the superconductor in pairs with opposite spins [93]. In this interaction between electrons, the attractive force developed was attributed to Coulombic attraction between the electrons and the crystal structure. This is because moving electron in the lattice creates a slight positive charge around it originating from the lattice atoms. This positive charge density then attracts a second electron (Figure 2.6 and Figure 2.7). This pair of electrons known as a *Cooper pair* travels through the lattice [94]. The crystal lattice must have small thermal vibrations in order to make the Cooper pairs exist and this explains why superconductivity occurs at low temperatures. As the superconductor is warmed

above T_c , the Cooper pairs separate into individual electrons and the material becomes non-superconducting.

The Cooper pairs act like bosons and can condense into a state with zero electrical resistance. The effective net attraction between two electrons produces a pair binding energy on the order of milielectron volts, enough to keep them paired at temperatures below T_c .

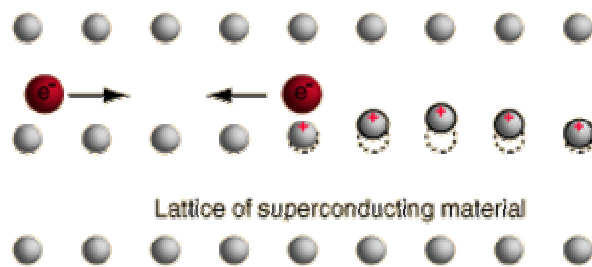


Figure 2.6 Passing electron attracts the cation lattice, causing a distortion in the lattice [95].

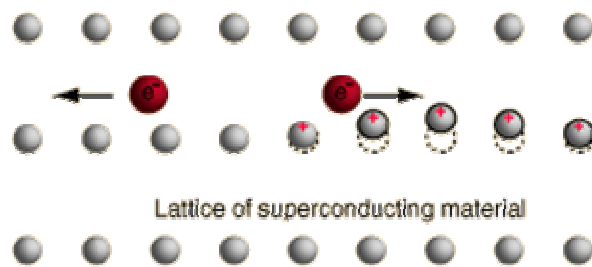


Figure 2.7 Another electron passing in the opposite direction is attracted to this lattice distortion (phonon): The electron-phonon interaction [95].

2.3 Theoretical Models for Non-Linear Current–Voltage measurements ($I - V$ Curves)

Transport measurements have always a central place in characterizing the superconductors. One of them is to measure the current–voltage ($I - V$) curves below T_c . The critical current which is a very important parameter for practical applications is extracted from the analysis of $I - V$ curves of superconductors. Figure 2.8 shows a schematic representation of sample voltage V versus current I (alternatively, electric field E versus current density J) [96].

The $E - J$ curve (or $I - V$ curve) includes three different regimes: First, thermally assisted flux flow (TAFF) in the low current region and second, the flux flow in the high current region. The third regime is the flux creep which lies between the two regimes. The flux creep and flux flow regimes were commonly used in describing the $I - V$ curves of low temperature superconductors. The new term TAFF was defined to understand the general behavior of the $I - V$ characteristics of high- T_c ceramic superconductors [97].

In Fig. 2.8, the critical current I_c is marked at the point where the sample voltage $V = 1 \mu\text{V}$, or equally, $E = 1 \mu\text{V/cm}$. In fact, it is quite reasonable to define I_c and the corresponding critical current density J_c as the point where the flux flow regime is just about to begin.

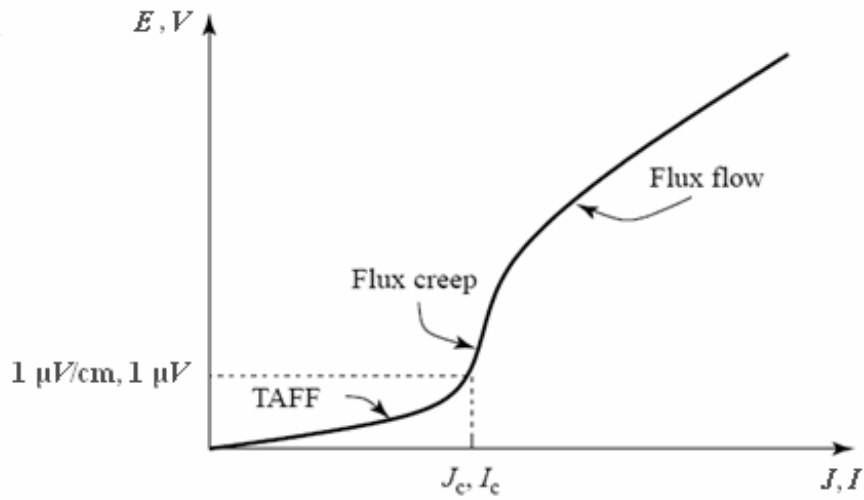


Figure 2.8 A schematic representation of the $I - V$ curves (or $E - J$ curves) of superconductors. The curve has a linear region at low I , followed by a highly nonlinear region at intermediate values of I , and finally a linear relation again. The definition of I_c or J_c is given on the curve by using the criterion of $V = 1 \mu\text{V}$, or $E = 1 \mu\text{V/cm}$ [97].

2.3.1 Thermally assisted flux flow (TAAF), flux creep and flux flow in superconductors

In a perfect (type-I) superconductor, the flux lines would be able to move easily and adjust their density according to the applied magnetic field. However, an energy barrier is created due to impurities and inhomogeneities in a real type-II superconductor, which prevents the flux motion. The energy of flux lines and type of pinning centers and also their distributions determine the pinning and de-pinning processes. The flux lines can be pinned by only suitable pinning centers.

At low dissipation levels corresponding to the first regime of thermally assisted flux flow (TAFF) regime in $I - V$ curve (Fig. 2.8), the measured voltage is caused mainly by the creep of flux lines. However, in addition to this process, increase in the temperature will provoke thermal fluctuations and, hence, the flux motion along the sample. Such a case will lead to the temperature dependence of resistivity $\rho(T)$ in Arrhenius type which is a measure of TAFF: $\rho(T) = \rho(0)\exp(-U_0/k_B T)$, where U_0 is the activation energy and k_B is the Boltzmann constant [97]. The TAFF process affects significantly both the transport and magnetic measurements of HTSC cuprates.

When a transport current with density J is applied to a type-II superconductor, it interacts with the flux lines and creates a Lorentz force $\vec{F}_L = \vec{J} \times \hat{n} \Phi_0$, where \hat{n} is the unit vector along the flux quantum Φ_0 . In order to observe a flux motion in the flux creep regime, the energy of flux lines should be less than (or comparable to) the effective pinning energy. In addition to \vec{F}_L , the thermal activation makes the flux bundles jump from one pinning site to another by causing a measurable dissipation (Figure 2.9) [98]. In this regime, the current density is not larger than J_c and also the Lorentz force \vec{F}_L is weaker than the pinning force \vec{F}_0 . Under these conditions, it can be anticipated that most of the flux lines do not participate the flux movement.

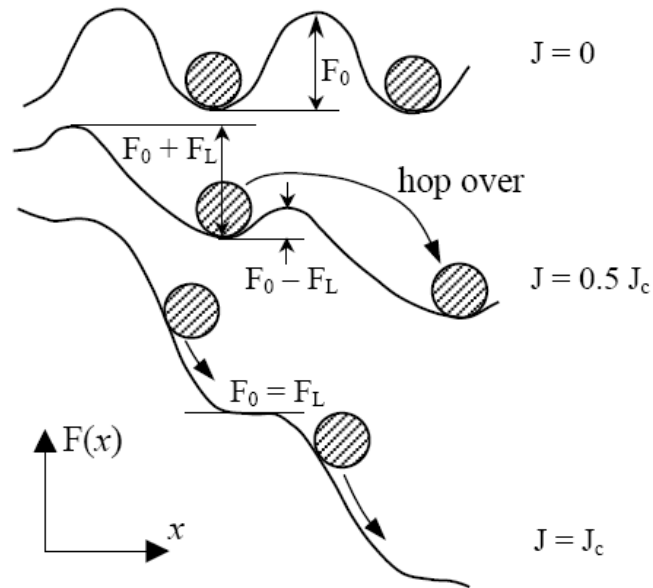


Figure 2.9 Different stages of flux motion, depending on the magnitude of transport current J . The presence of current in a magnetic field generates a Lorentz force F_L which tilts the staircase allowing the flux lines to hop out of their wells more easily [98]. Here F_0 is the pinning force and x is the position of moving flux line system.

As the current density is increased, the depth of the pinning wells becomes relatively smaller because the effective pinning potential depends explicitly on J . At a certain value of $J = J_c$, the Lorentz force becomes equal to (or greater than) the pinning force ($F_L \geq F_0$), and all flux lines start to move as is shown in Fig. 2.9. This is known as *flux-flow regime* which corresponds to a correlated motion of whole flux line system. J_c is called the *critical current density* which is a very important parameter for practical applications since it gives the maximum current carrying capacity of the superconductor.

2.3.2 Proximity effect

The proximity effect occurs when a superconductor (S) is in contact with a normal metal (N). If the contact between the superconductor and normal metal is sufficiently good in quality, the order parameter associated with the wave function $\psi(r)$ of the superconductor close to the interface will alter. The superconducting region will induce superconductivity in the metal which is in the normal state before the contact. This induced superconductivity exists only in a thin surface layer of the normal metal near the S – N interface. The distance measured from the S to N in the interface is in the order of the coherence length ξ [99].

When a normal metal and a superconductor are in good contact, it is assumed that the Cooper pairs penetrate into the normal metal from the superconductor, then stay and live there for a while [99]. This results in a reduction of the Cooper pair density in the superconductor. This also means that some part of a material, which is not a superconductor, can have a superconducting state under certain conditions. Thus, the proximity effect for a S – N structure gives rise to an induced superconductivity below T_c and it is the strongest at the temperatures $T \ll T_c$ [99].

In a granular superconducting material, such as polycrystalline samples of HTSC cuprates, the junction type between the grains evolves mostly in the form of Superconductor–Insulator–Superconductor (SIS) junction and rarely Superconductor–Normal–Superconductor (SNS) one. The effective junction type

of granular systems can be found from the comparison of experimental temperature dependence of I_c with the relationship $I_c = \text{const}(1 - T/T_c)^m$, where m is an exponent [100]. For instance, if $m = 1$, the effective junction inside the granular system is assumed to be mostly SIS type or if $m = 2$, the intergrain junctions develop mostly in SNS type. In addition, due to the sample preparation, the intergrain junction can be of Superconductor–Insulator–Normal Metal–Superconductor type (SINS) for $m = 1.5$.

2.4 Transport Relaxation and Glassy State

In the glassy state, it is assumed that there are several energy states developed inside the material, which affect dramatically the motion of flux lines. Such an energy landscape includes a broad distribution of both long- and short-lived metastable states separated by several energy barriers [14, 19, 20, 27, 28, 42, 47]. The energy barriers between the neighboring energy states can be small while the difference between the more distant barriers can be higher. In a polycrystalline superconducting sample, the energy landscape corresponds to the frustrated superconducting domains coupled by weak links, and such a description can lead to the concept of the superconducting glass model. Due to the driving force F_L together with thermal activation, the flux lines can easily overcome the neighboring barriers, but may fall in a deeper energy well. Thus, bundle of flux lines remaining at the bottom of deeper wells can not overcome these wells and give no contribution to the measured voltage. In this process, it is observed that the sample voltage decreases as the time progresses. The relaxation of sample

voltage with time can be correlated with decrease in the number of the flux lines which lose their capability of motion [47].

In glassy state relaxation, the time evolution of the sample voltage is described by [14, 19, 20, 27, 28, 42, 47]

$$V(t) = V(0) \exp(-t/t_0), \quad (2.12)$$

where t_0 is the characteristic time. Some experimental observations provide evidence that the glassy state relaxation fits to a stretched exponential time dependence [44-46] in the form:

$$V(t) = V(0) \exp(-t/t_0)^\alpha. \quad (2.13)$$

Here the exponent α is a constant which depends on temperature and magnetic field. Equation 2.13 describes well the time decay in the remnant magnetic moment of ordinary spin glasses. In this expression, the time evolution and degree of ordering of individual magnetic moments can be determined mainly via the exponential term. A glassy state (or quenched disorder) in superconducting state can be created by decreasing of current (or external magnetic field) to a finite value or zero. The decrease in sample voltage corresponding to quenched disorder which evolves to low dissipation values can be described well by the expression given by Eq. 2.13. It is noted that such a time dependence of glassy state is reminiscent of spin glasses.

2.5 Magnetoresistance in Granular Superconductors

2.5.1 The two-level magnetic system and intra- and inter-granular flux trapping model

In this model, it is assumed that the granular sample is composed of superconducting grains and weak-link junction network [53-57, 101-103]. It is based on the fact of two distinct critical current densities: The larger one locally evolving inside the grains (i.e., intra-grain current density) and the other one, which is relatively lower than that in the grains, is the macroscopic intergranular current density. Since the gradient of flux density inside the grains is larger than that in the intergranular region, the analytical solution of the usual critical state model is manipulated on the basis of magnetic states associated with both intra-grain and inter-granular regions of the sample. The two-level magnetic system was originally proposed by Ji *et al.* [53], and, later, was extended by Mahel and Pivarc [54] to explain the hysteresis effects in HTSC cuprates.

In the following, we introduce the two-level magnetic system which has been modified and adopted to HTSC cuprates by Balaev *et al.* [55-57]. In this model, it is assumed that the pinning in Josephson barriers (i.e., inter-granular boundaries) is weak and the magnetic flux is trapped mainly in the superconducting grains. It is also assumed that the contribution of grain boundaries to the diamagnetic response of the sample is negligibly small. In this case, for $H > H_{c1}^w$, where H_{c1}^w is the first critical field of the junction network, a local field B_i develops along

the junction network, which is equal to the vector sum of the applied magnetic field H and the field B_g induced by the magnetization of the grains:

$$\vec{B}_i = \mu_0(\vec{H} + \vec{B}_g). \quad (2.14a)$$

Since $\vec{B}_g = G\vec{M}_g$,

$$\vec{B}_i = \mu_0(\vec{H} + G\vec{M}_g). \quad (2.14b)$$

Here G is a coefficient depending on the location and shape of the superconducting grains and M_g is the magnetization of HTSC grains [54-57, 101-103].

The effective field B_{eff} in the intergranular region can be found as an average of the distribution of local field B_i over all grain boundaries:

$$B_{\text{eff}} = \langle B_i \rangle = \mu_0[H - M_g(H)f(H)]. \quad (2.15)$$

Here $f(H)$ is the average value of G over the junction network and depends on the magnitude of the external magnetic field. The magnetization $M_g(H)$ is produced by the shielding currents and the associated flux gradient evolving inside the sample.

In the case of flux trapping in junction network, the pinning of flux lines requires the magnetization of intergranular region M_i , and the local field \vec{B}_i^w in the junction network which is the superposition of the external field \vec{H} and the field \vec{B}_g induced by the grains. In the region of grain boundaries considered, \vec{M}_i makes a contribution to \vec{B}_i^w opposite to that of \vec{B}_g . Thus, the effective field B_{eff}^w in the junction network can be found by averaging the distribution of local field B_i^w and can be written as [55]

$$B_{\text{eff}}^w = \langle B_i^w \rangle = \mu_0 (H - [M_g(H)f(H) - M_i(H,I)]). \quad (2.16)$$

At low applied magnetic field values, when the self-field induced by the transport current is comparable to the first and second critical fields H_{c1}^w and H_{c2}^w of the junction network, respectively, we note that the magnetization of intergranular region of HTSC sample (M_i) becomes current (I) dependent.

In the hysteresis loops of $V - H$ curves, the equality of voltage values $V(H^+)$ and $V(H^-)$ corresponding to the increasing and decreasing fields H^+ and H^- , respectively, indicates the equality of effective fields, i.e., $B_{\text{eff}}(H^+) = B_{\text{eff}}(H^-)$ (Fig. 2.10). When the pinning in the junction network is small, the contribution to the total magnetization from this medium will be small too, and, therefore, the equality can be written by using Eq. 2.15 [55]

$$H^+ - M_g(H^+)f(H^+) = H^- - M_g(H^-)f(H^-). \quad (2.17)$$

The width of the hysteresis loop $\Delta H = H^- - H^+$ observed in the $V - H$ curve for a given value of measured sample voltage V can be written as

$$\Delta H = [M_g(H^-)f(H^-) - M_g(H^+)f(H^+)]. \quad (2.18)$$

It can be seen from Eq. 2.15 that the value of B_{eff} is determined only by the applied magnetic field and the magnetization of grains, and, therefore, ΔH in Eq. 2.18 must be independent of the transport current [55].

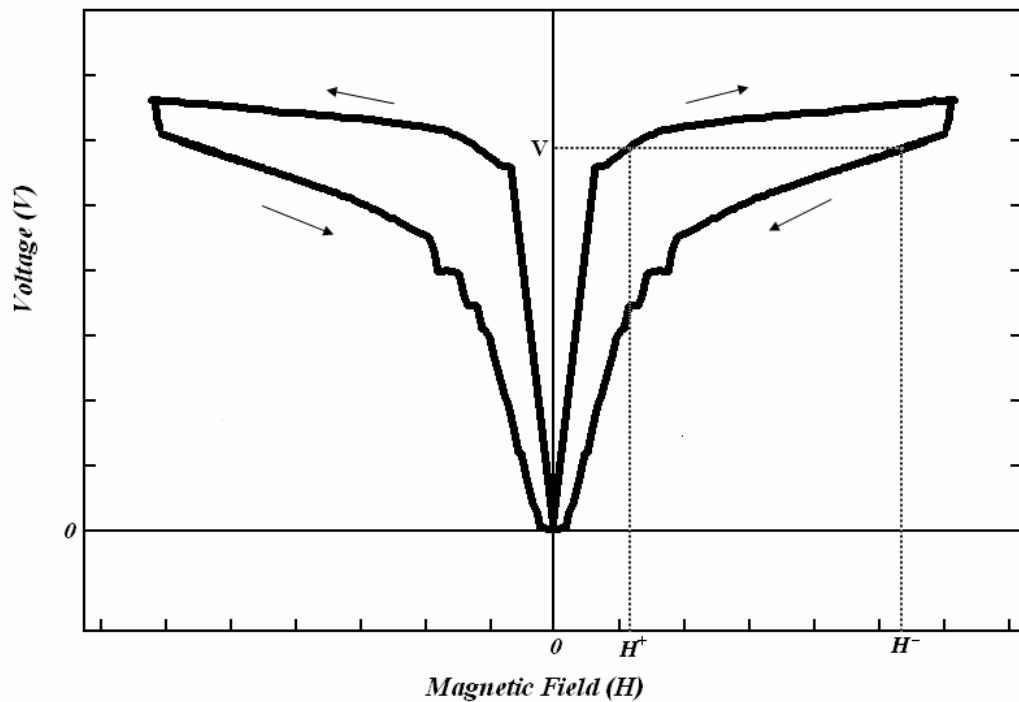


Figure 2.10 Schematic plot for magnetovoltage ($V - H$ curve). The increasing and decreasing external magnetic fields corresponding to the same sample voltage value are labeled as H^+ and H^- , respectively. ΔH is the difference between H^+ and H^- for a given value of measured sample voltage. $\Delta H = H^- - H^+$ is the width of the hysteresis loop.

If the flux trapping in the intergranular medium is negligible, then, ΔH expected to be independent of the variation in the transport current. However, if ΔH becomes current dependent, this may imply that there is a flux pinning in the junction network which contributes to the effective field (B_{eff}^w) in the intergranular region, and, thus, B_{eff}^w will change with the transport current. In this case, ΔH can be written [55]

$$\Delta H = [M_g(H^-)f(H^-) - M_i(H^-, I)] - [M_g(H^+)f(H^+) - M_i(H^+, I)]. \quad (2.19)$$

In order to observe the current dependent $\Delta H - H^-$ curves, at a given temperature, the self-field induced by the transport current and the applied magnetic field must be sufficiently low and comparable to the corresponding junction parameters since $M_i \ll M_g$.

2.6 $\text{YBa}_2\text{Cu}_3\text{O}_{7-x}$ (YBCO-123) System

The most extensively studied high temperature superconductor cuprate is $\text{YBa}_2\text{Cu}_3\text{O}_{7-x}$, or shortly YBCO-123 with $T_c \approx 90$ K. This compound was discovered in 1986 by Wu *et al.* [78] and is the first compound of which T_c exceeds the boiling point of liquid nitrogen (i.e., 77 K at 1 atm). It exhibits one of the most interesting and complex relationships between chemistry, crystal structure and physical properties of any ceramic material studied.

It was found that the oxygenation procedure of YBCO-123 samples is very crucial in obtaining best superconducting properties. In a typical sample preparation procedure, YBCO-123 is formed with oxygen content close to six and then has to undergo a phase transition from tetragonal to orthorhombic structure, including the characteristic formation of twin boundaries. In principle, it is extremely difficult to reach the $x = 0$ state within reasonable time periods [104-107]. Figure 2.11 shows tetragonal and orthorhombic phases of $\text{YBa}_2\text{Cu}_3\text{O}_{7-x}$.

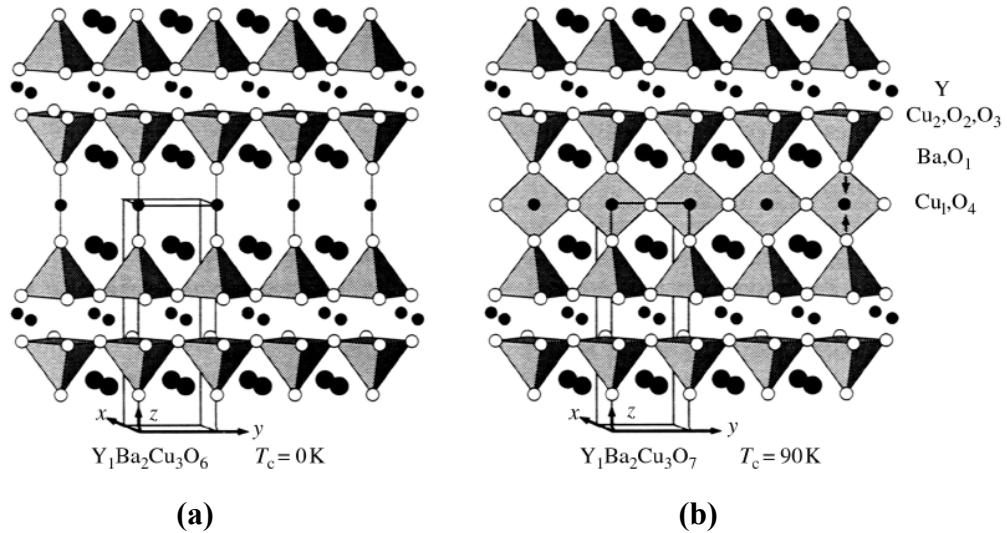


Figure 2.11 Structures of **(a)** tetragonal $\text{YBa}_2\text{Cu}_3\text{O}_6$, **(b)** orthorhombic $\text{YBa}_2\text{Cu}_3\text{O}_7$ (xy is ab -plane, z is c -axis of the unit cell) [108].

As the other high- T_c superconductors, YBCO-123 is a type-II superconductor. The flux of charge carriers along their CuO_2 layers causes a high anisotropy in these materials, whose physical properties in the ab -plane are different than those along the c -axis direction. The main superconducting characteristics of YBCO-123 are summarized in Table 2.1.

Table 2.1 Main superconducting parameters of $\text{YBa}_2\text{Cu}_3\text{O}_{7-x}$ (YBCO-123) in the ab-plane and along the c-axis direction at zero temperature. ξ is the coherence length, λ the penetration length, J_c is the critical current density, and H_{c1} and H_{c2} are the lower and upper critical magnetic fields, respectively (data extracted from references [108-110]).

	ab-plane	c-axis
$\xi(0)$ (nm)	1.5–4.3	0.3–0.7
$\lambda(0)$ (nm)	100–140	500–800
$J_c(0)$ (A/cm^2)	$3\text{--}12 \times 10^8$	$5\text{--}25 \times 10^7$
$H_{c1}(0)$ (mT)	2–23	8–9
$H_{c2}(0)$ (T)	230–624	70–122

2.7 Grain Boundaries in YBCO

It is believed that conductivity of grain boundaries of YBCO-123 arises from two different channels of intergrain conduction. Weak links (Josephson tunnel junctions or proximity junctions) between the superconducting grains are the major channel that occupies about 99.9 % of the grain boundary area available for the current but can not carry the supercurrent at high magnetic fields [90]. The second channel is produced by microbridges of intrinsic intragranular material (strong links) across the grain boundaries. Those microbridges occupy less than 0.1 % of the grain boundary area but they can carry supercurrent up to very high magnetic fields. The grain boundaries in YBCO-123 are structurally and compositionally heterogenous on a scale of 1-5 nm, which is comparable to the

coherence length ξ of YBCO-123 at 77 K. Low angle grain boundaries consist of grain boundary dislocation cores and conductive, grain like channels [111].

Any change in the orientation of grain boundaries on the atomic scale strongly affects the coupling between the grains, leading to a local decrease of J_c due to grain boundaries. Thus grain boundary misorientation controls the macroscopic J_c characteristics of YBCO-123 ceramic. The J_c of bulk polycrystalline YBCO-123 has a maximum value of 10^3 A/cm² at 77 K which is about 1000 times less than that ($J_c = 10^6$ A/cm²) obtained for thin films and single crystals of YBCO-123.

This large difference has various origins:

- (i) The strong dependence of J_c on crystallographic orientation, which is due to the intrinsic anisotropic properties of the YBCO-123 structure,
- (ii) The oxygen content due to oxygen self-diffusion,
- (iii) The oxygen content dependence on the grain boundary misorientation,
- (iv) The quality of grain boundaries, either clean or damaged.

All these parameters are present simultaneously inside the grains and for each grain boundary in the YBCO-123 structure. Therefore, J_c results from a combination of these physical properties.

The superconducting transition profile of YBCO-123 is also related to grains and it can be divided into two regimes [31, 112]. The first regime, called the main transition regime, corresponds to drop of resistance in the grains. It depends

mainly on the chemical composition and on the oxygen stoichiometry of the grains. The second regime is lying immediately below the main one and covers the temperature range down to zero resistance. The current transport in this regime is controlled by the grain boundaries (weak links) and corresponds to the temperature range where the Josephson coupling energy of the weak link is insufficient to overcome the thermal energy. This regime becomes broader in the presence of defects in the grain boundaries (intergranular phases, misorientations, oxygen deficiency, or cationic deficiency).

2.8 Effect of Doping Ag in YBCO-123

It is known that doping of silver in YBCO-123 ceramics improves significantly its plastic, mechanical and electrophysical properties [113-115]. This is one of the important methods of forming articles of arbitrary form of bulk, film or wire YBCO-123 samples. In the doping process, there is no chemical reaction between Ag and the YBCO-123 lattice and Ag atoms are not incorporated into the YBCO-123 lattice.

Ag can fill the intergranular spaces and improve both mechanical and electrical properties of YBCO-123 ceramic. Ag addition in YBCO-123 shows sizable enhancement in the critical current density J_c and reduction in the normal state resistivity. Moreover, improvement in the flexibility and chemical stability of YBCO-123 were reported without reduction in the superconducting transition temperature T_c [116-118]. The J_c enhancement implies better compactness, grain

alignment, grain growth and flux pinning due to stress field in the YBCO/Ag composites. The improvement in J_c can be attributed either to improved coupling between the superconducting grains or to stronger pinning of the intergranular vortices induced by the presence of silver. With silver doping, the grain size is increased and inter-grain current is decreased in YBCO-123 samples [119], because Ag provides conductive paths between superconducting grains. Ag doping reduces the thickness of effective grain boundaries and the critical current density of the sample increases. Thus, doping Ag into YBCO-123 reduces the “weak link” effects [120]. The presence of Ag between the YBCO-123 grains can also provide a plastic flow region and relax undesirable residual stresses in the ceramic sample resulting from the grain anisotropy of superconductors [121].

The normal state resistivity of the YBCO-123 samples decreases with Ag doping. Normal state resistivity and critical temperature of YBCO-123 samples contain important information associated with its granularity. The normal state resistivity of a granular superconductor depends on mainly the distribution of grains, the grain dimensions and inter-grain contacts [73].

Silver can be doped into YBCO-123 by different ways: By mixing with metallic Ag [113-115], by mixing with AgO_2 [122-124], by electrochemical methods [125-127], by diffusion of Ag [128, 129], and by mixing with AgNO_3 [121]. The first two methods result in a random non-uniform distribution of Ag in the composite, the third and fourth methods result in a non-random distribution of Ag on the grain surface.

In this work, the last method (by mixing YBCO-123 with AgNO_3) has been chosen, because AgNO_3 can distribute more uniformly in the YBCO-123 structure and it is more efficient than mixing YBCO with pure Ag. The decomposition temperature of AgNO_3 ($T_d = 440$ °C) is lower than the sintering temperature of YBCO-123 samples and it is higher than the melting point of AgNO_3 ($T_m = 212$ °C). According to these special conditions, the mixture is brought to the AgNO_3 melting point, at this stage the grains of YBCO-123 are wetted by the melt of AgNO_3 . This allows better homogenization of the composite. In the next stage the mixture is heated above T_d thus AgNO_3 decomposes and pure Ag is deposited on the grain boundaries.

CHAPTER 3

EXPERIMENTAL SET-UP

3.1 Sample Preparation

The polycrystalline YBCO-123 samples were prepared by the conventional solid state reaction method [50] using high purity powders of Y_2O_3 , $BaCO_3$, CuO and $AgNO_3$ (Aldrich Co). All the powders are of %99.99 purity. The powders were weighted in the stoichiometric proportions by using an electronic balance (Sartorius CP2245). The amount of Ag added was equal to 3% weight of nominal composition of Cu in YBCO-123. The powders were mixed and grinded in an agate mortar for approximately 2 hours in order to obtain a homogenous mixture. The mixed powder was put in a alimuna (Al_2O_3) crucible for calcination. The latter process was carried out at 930 °C for 12 hours in a microprocessor controlled tube furnace (Carbolite CTF 12/100/90).

After the calcination, the powder was reground and pestled in an agate mortar for approximately 1 hour. Then, the powder was pressed with a pressure of 10 Tons/cm² into a disc shaped pellet with a diameter of 10 mm and thickness of ~ 1.8 mm [Lightpath Optical (UK) LTD] in a stainless steel die for 5 minutes.

In order to obtain the desired orthorhombic phase (i.e., the YBCO-123 phase), the pellets were put again into the furnace and were sintered under oxygen (O_2) atmosphere with a pressure of ~ 1 atm at 950 °C for 12 hours. The pellets were cooled down to the room temperature with a low cooling rate of 1 °C/min (Fig. 3.1(a)). The latter process (including grinding and sintering) outlined above was repeated twice to raise the quality of the samples.

In the final step, to satisfy the sufficient O_2 absorption, the pellets were annealed at 550 °C for 12 hours at O_2 atmosphere and then cooled down to room temperature with a rate of 1 °C/min (Fig. 3.1(b)).

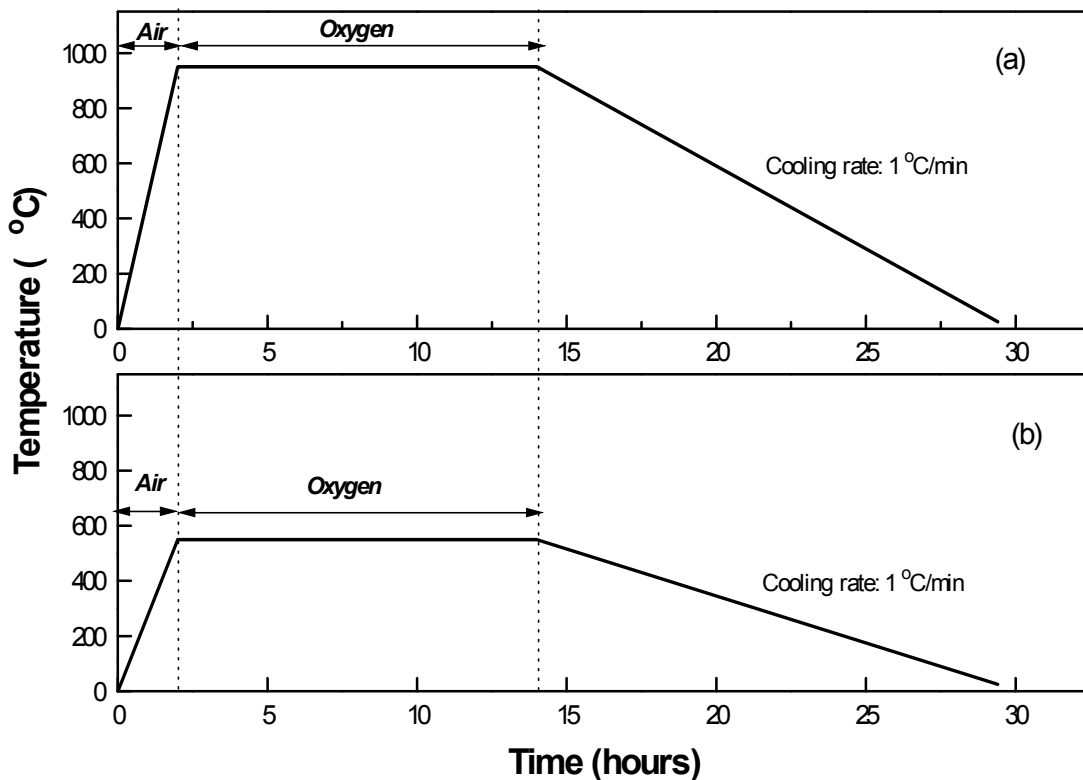


Figure 3.1 Schematic thermal profile of (a) sintering and (b) annealing of Ag doped YBCO-123 sample.

The prepared Ag-doped and undoped YBCO-123 polycrystalline bulk samples were cut by using diamond saw in the shape of rectangular prism with typical dimensions of length $\ell = 4.0$ mm, width $w = 0.8$ mm, thickness $t = 0.4$ mm. Such low sample dimensions are necessary to eliminate any Joule heating effects on the current leads.

3.2 Structure Analysis

There are several ways to characterize the crystalline and morphological structure of a material. In this work, three methods were employed to study material structure: Scanning Electron Microscopy (SEM), Energy Dispersive Spectroscopy (EDS) and X-Ray Diffraction (XRD). The topography and morphology of a polycrystalline superconducting YBCO/Ag sample was studied by SEM. Information on the structures and phases of the sample was obtained through X-ray diffraction patterns, and the composition of the YBCO/Ag sample was analyzed using EDS.

3.2.1 Scanning electron microscopy (SEM) and energy dispersive spectroscopy (EDS) of YBCO-123 samples

The microstructures of undoped and Ag-doped YBCO-123 samples were investigated by SEM (JEOL 6390 – LV). Images were obtained by detecting the secondary electrons emitted from the samples while an electron beam impinged on the surface of the bulk samples.

Figs. 3.2 (a) and 3.2 (b) show typical SEM micrographs for undoped YBCO-123 and Ag-doped YBCO-123 samples, respectively. It can be observed that Ag particles are preferentially distributed along intergranular region of superconducting structure forming amorphous metallic regions between grains. Porosity is observed over the samples in both samples.

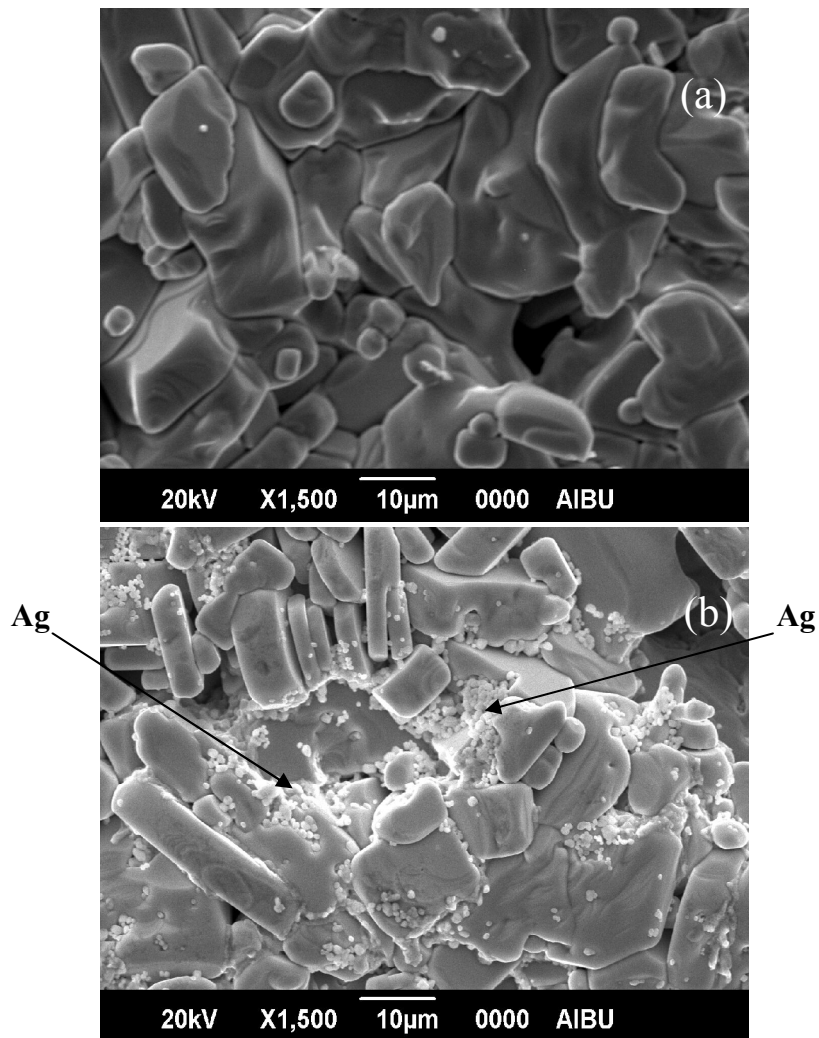


Figure 3.2 SEM photomicrographs of (a) undoped and (b) 3 wt % Ag-doped polycrystalline YBCO-123 bulk samples. White shiny regions observed in SEM are the images of Ag. The magnification of SEM images is 1500.

The grain size of undoped and Ag-doped YBCO-123 samples was estimated by using SEM photomicrographs. We found that the grain size of the undoped sample varies between 3.75 – 33.75 μm , whereas, for the Ag-doped sample, it varies between 2.5 – 25 μm . The grain size of the undoped sample is generally greater than the doped sample.

Energy Dispersive Spectroscopy (EDS) is a chemical microanalysis technique used in conjunction with SEM. In this study, EDS analysis was carried out to investigate stoichiometry and chemical composition of the Ag-doped YBCO-123 sample. EDS analysis showed that amount of silver in YBCO/Ag is ~ 3.48 wt %. Note that this value is comparable to the amount of doping of Ag into the superconducting structure.

3.2.2 X-ray diffraction (XRD)

In this thesis, the XRD data were collected at room temperature using a Rigaku D/Max-IIIC diffractometer with Cu K_{α} radiation ($\lambda = 1.542 \text{ \AA}$) over the range $2\theta = 3^{\circ} - 60^{\circ}$ with a scan speed of $0.2^{\circ} \text{ min}^{-1}$. The XRD patterns of the undoped and Ag-doped polycrystalline YBCO/Ag samples are presented in Figure 3.3. The reflections indexed in the patterns (Joint Committee on Powder Diffraction Standards (JCPDS) file) match almost the orthorhombic structure of YBCO-123 material and belong to the YBCO orthorhombic unit cell.

For the Ag-doped YBCO sample, we could clearly identify two silver peaks of Ag(111), Ag(200) reflections which indicate the presence of silver as a separate metallic phase [129]. The lattice parameters a , b and c were obtained from 2 θ values by least square refinement of Bragg equation, which are given in table 3.1. The obtained lattice parameters are in agreement with published results [130-132] (see Table 3.2).

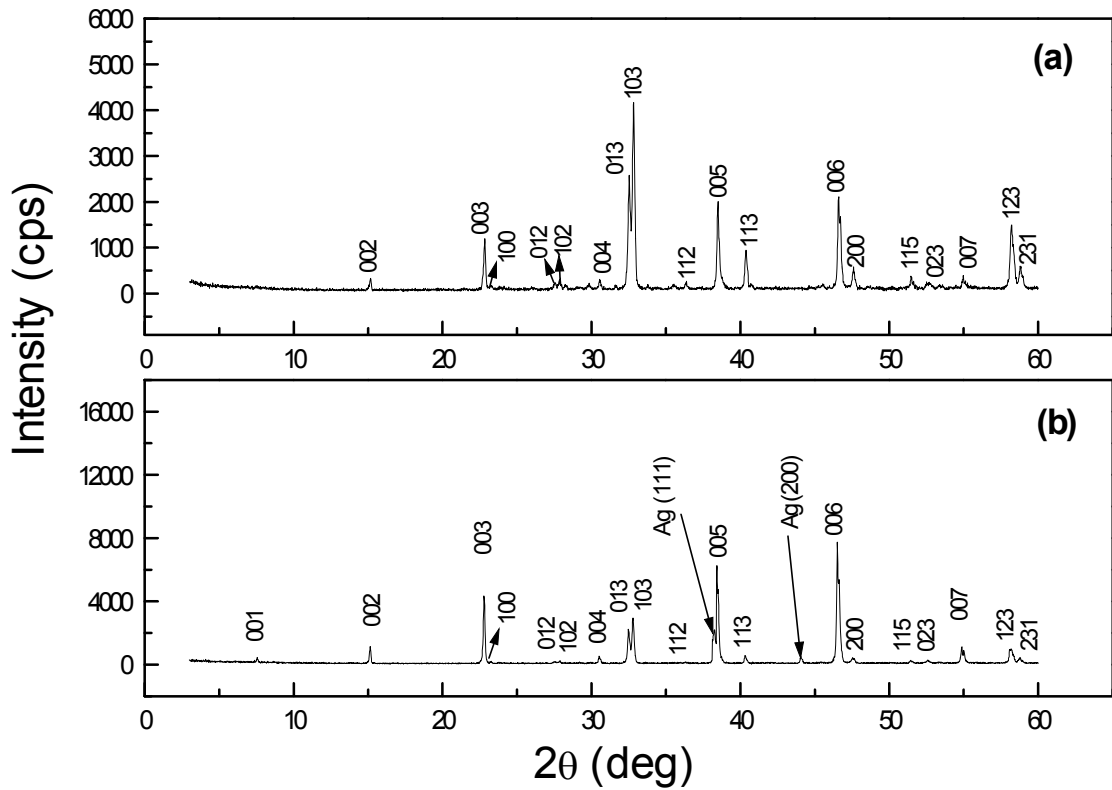


Figure 3.3 X – ray diffraction (XRD) patterns of (a) undoped, (b) Ag-doped YBCO-123 samples.

Table 3.1 The lattice parameters a , b and c for undoped and Ag-doped samples.

	YBCO	YBCO/ Ag (3%)
a (Å)	3.8176	3.8236
b (Å)	3.8882	3.8923
c (Å)	11.6789	11.6942

Table 3.2 The lattice parameters a , b and c for Ag-doped samples (data extracted from ref. [130])

Ag (%)	0.5	2.5	5.0
a (Å)	3.8225	3.8227	3.8240
b (Å)	3.8892	3.8904	3.8900
c (Å)	11.6760	11.6790	11.681

3.3 Measurement Set-up

The transport measurements were carried out using the four point probe technique. This method consists of attaching four contacts to the sample. The four contact configuration is fundamental because it enables us to minimize the contribution of spurious voltage signals due to current contacts. Copper wires with diameter of 0.5 mm for current and voltage pads were attached to the sample by using good quality silver paint (Electroday, 1415). The contact resistance measured by using the three point method was of the order of $10^{-2} \Omega$ below T_c and $10^{-1} \Omega$ at room temperature.

After making contacts, the sample was placed carefully into a closed cycle refrigerator [Oxford instruments, (OI) CCC1104]. Thus, the samples are ready to be measured.

A block diagram of the measurement set-up is given in Fig. 3.4. All measurements were carried out under PC control via an IEEE - 488 interface card. A temperature stability better than 0.01 K was maintained during the measurements (OI, ITC-503 temperature controller). The temperature was measured by using a calibrated 27 Ohm-Rhodium-Iron thermocouple (OI, Calibration number 31202). In the experiments Keithley-2182A (nanovoltmeter) with a resolution of 1 nV and Keithley 6221 (current source) were used in measuring the sample voltage and applying the current, respectively. The nanovoltmeter was triggered for a maximum of 61/2 digits, and its buffer was read directly within the integration time of 100 ms in order not to cause any artificial effect. The measured sample voltage is the average value of 5 readings for each data point. In all measurements under external magnetic field, the magnetic field was generated by an electromagnet (OI, N100 electromagnet).

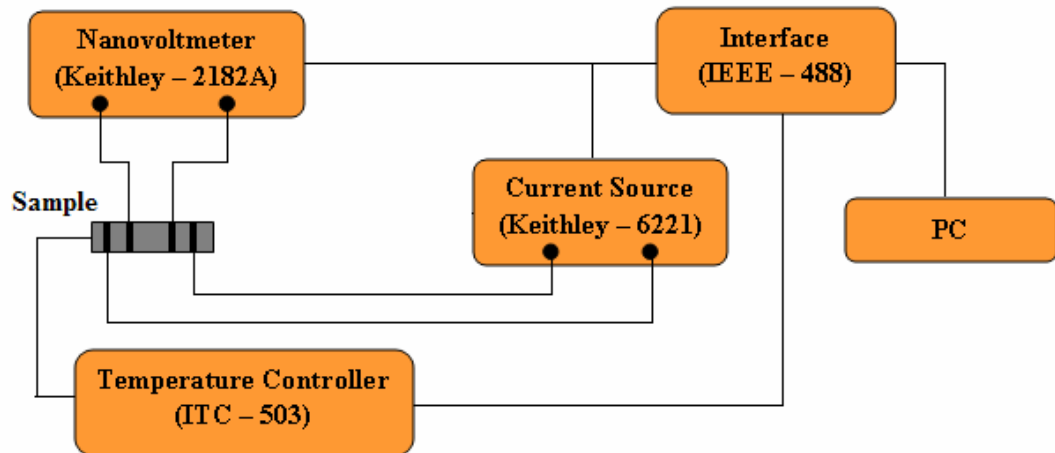


Figure 3.4 Block diagram of the experimental set-up used in the measurements.

3.4 Current-Voltage Characteristics ($I - V$ Curves) Measurements

In order to determine the current carrying capacity of the samples, current-voltage ($I - V$) characteristics were measured at temperatures near T_c of the samples by using the experimental set-up in Fig. 3.4. The critical current density (J_c) of an Ag-doped YBCO-123 polycrystalline bulk sample, whose results are presented in this study, is $\sim 40 \text{ A/cm}^2$ at $T = 88 \text{ K}$ by using the $1 \mu\text{V/cm}$ criterion.

In the $I - V$ measurements, the standard and reverse procedures were applied in measuring the $I - V$ curves in Ag-doped YBCO-123 samples. In the standard procedure, the transport current (I) is increased from zero to a maximum value (I_{max}) and then decreased from I_{max} to zero. Thus, current-increase (CI) and current-decrease (CD) branches are obtained, respectively. In the reverse procedure, first I_{max} is applied and then it is decreased to zero; in final stage, the applied current is increased from zero to I_{max} . Thus, the reverse current-decrease (RCD) branches and reverse current-increase (RCI) branches were obtained. During the evolution of the $I - V$ curves, the sweep rate of transport current (dI/dt) is taken constant.

3.5 Electrical Transport Relaxation ($V - t$ Curves) Measurements

The slow transport relaxation measurements ($V - t$ curves) were carried out by applying dc currents to the samples. An initial current (I_1) is applied to the sample and the evolution of the sample voltage was measured as a function of time. In

order to create a quenched state, after reaching the steady state, the initial current I_1 was reduced to a finite value I_2 (or interrupted) for the rest of the relaxation process.

The time evolution of the sample voltage ($V - t$ curves) was also measured by applying bi-directional square wave (BSW) current [with long period (P) and different amplitudes] at zero magnetic field ($H = 0$) and by applying magnetic field (H). For our purpose, the commercial current source (Keithley-6221) and the nanovoltmeter (Keithley-2182A) are adequate to produce such BSW currents, and to read low voltage levels with high precision. Just after the driving current is applied, we started to measure the sample voltage developing along the sample as a function of time. Thus, monitoring of all details of the time evolution of the sample-voltage including the transient effects becomes possible.

3.6 Magnetovoltage ($V - H$ curves) Measurements

The magnetovoltage ($V - H$ curves) measurements were carried out as functions of the temperature (T), magnitude of the transport current (I), and the sweep rate (dH/dt) of the applied magnetic field (\vec{H}) for $\vec{H} \perp \vec{I}$. To be able to see the time effects in the $V - H$ curves, the value of dH/dt is of crucial importance. The magnetic field was swept in the forward and reverse regions in which the polarity of \vec{H} was changed with different dH/dt values. The speed of measurement was always greater than that of the field-sweep rate dH/dt ; otherwise it was impossible to measure the sample voltage properly as dH/dt is varied.

CHAPTER 4

EXPERIMENTAL RESULTS

In this chapter, experimental results of the transport, transport relaxation and magneto-voltage measurements are presented.

4.1 Resistivity versus Temperature Measurements on the Ag-Doped YBCO Sample

A typical example for the resistivity versus temperature ($\rho - T$ curve) of Ag-doped YBCO (YBCO/Ag) sample is given in Fig. 4.1. The critical temperature T_c of the sample at zero magnetic field is found as ~ 92 K from the derivative of the resistivity with respect to temperature (i.e. the $d\rho / dT - T$ curve) which is given in the inset of Fig. 4.1. The width of transition region ΔT_c is about 0.3 K at zero applied field, which is consistent with those of given in the literature [31]. The $\rho - T$ curve in the normal state shows nearly a metallic behavior and the resistivity decreases with decreasing temperature until the superconducting transition occurs. Note that the normal state resistivity (ρ_n) of the YBCO/Ag sample at room temperature is less than 0.1 m Ω -cm. This value is much smaller than that of undoped polycrystalline YBCO sample with $\rho_n \sim 1.5$ m Ω -cm and reflects directly the effect of Ag doping on transport properties of YBCO ceramics.

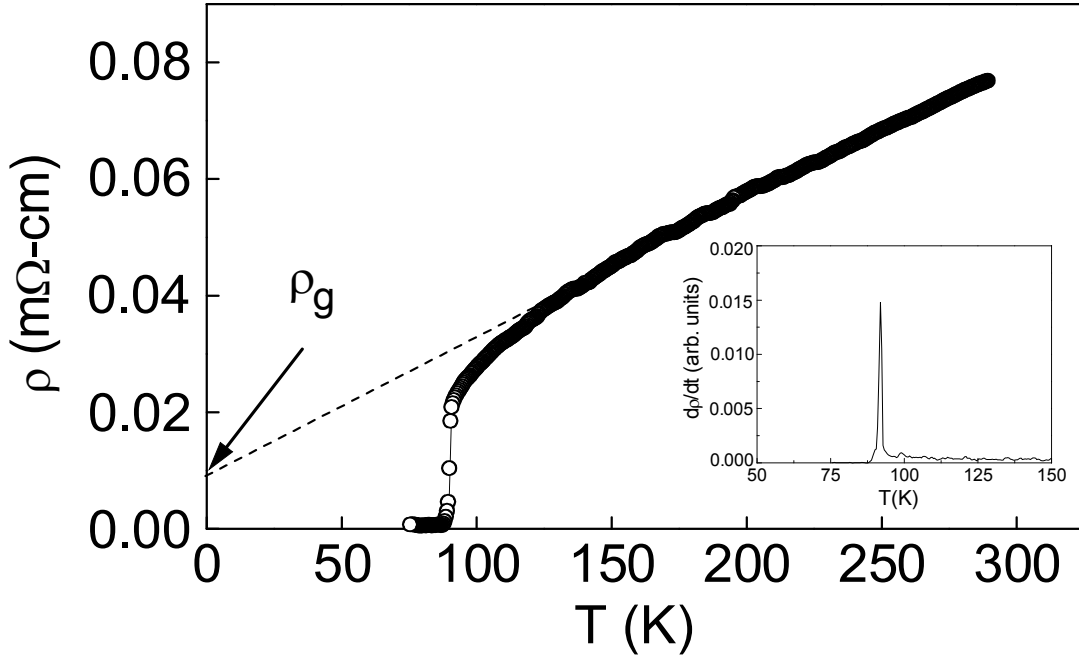


Figure 4.1 The resistivity of the bulk polycrystalline YBCO/Ag sample as a function of temperature. The inset shows the derivative of resistivity with respect to temperature ($d\rho / dT$). ρ_g is defined as the grain boundary resistivity.

The zero temperature intercept of the normal state resistivity ($\sim 10 \mu\Omega\text{-cm}$) can be attributed to the grain boundary resistivity ρ_g . The magnitude of ρ_g reveals that the coupling between grains is enhanced significantly by adding of Ag to YBCO.

4.2 Current – Voltage Characteristic ($I - V$ Curve) Measurements

Figure 4.2 shows example for the hysteretic and non-linear $I - V$ curves of the YBCO/Ag sample measured using the standard procedure at temperatures $T = 85 \text{ K}$, 84 K and 82 K with current sweep rate $dI/dt = 0.312 \text{ mA/s}$ and applied magnetic field values of $H = 10 \text{ mT}$ and $H = 20 \text{ mT}$. The magnetic field was

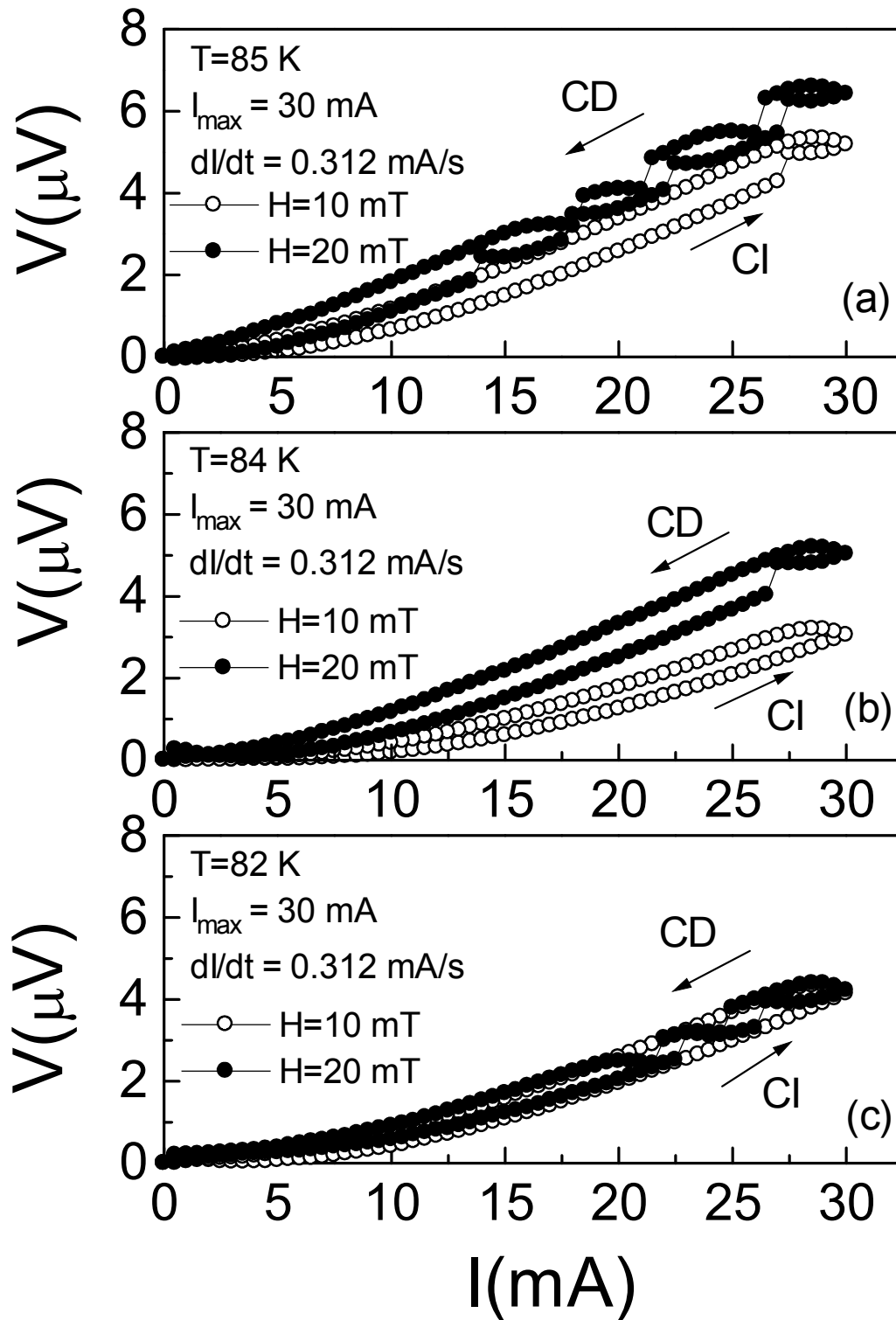


Figure 4.2 The $I - V$ curves of the YBCO/Ag sample measured using the standard procedure with $dI/dt = 0.312 \text{ mA/s}$ and applied magnetic field $H = 10 \text{ mT}$ and 20 mT , at **(a)** $T = 85 \text{ K}$, **(b)** $T = 84 \text{ K}$, **(c)** $T = 82 \text{ K}$. The arrows show the direction of sweeping of the applied current. CI and CD with the arrows indicate the current-increase and current-decrease branches of the $I-V$ curves upon cycling of the transport current, respectively.

oriented perpendicular to the transport current ($\vec{H} \perp \vec{I}$). Each $I - V$ curve consists of two branches: The current-increase (CI) branch measured as the current is increased from zero to a maximum current value I_{\max} ($= 30$ mA) and the current-decrease (CD) branch measured as the current is decreased from I_{\max} to zero. Upon cycling the transport current, all $I - V$ curves exhibit a hysteretic and non-linear behavior. We also observed several drops and jumps in the $I - V$ curves, especially for those obtained at $H = 20$ mT. The voltage drops and jumps are quite prominent in the $I - V$ curves measured at $H = 20$ mT and temperatures $T = 82$ K, 84 K and 85 K. However, the $I - V$ curves measured at $H = 10$ mT exhibit more stable behavior when compared to those measured at $H = 20$ mT. The results indicate that such instabilities (jumps and drops in the sample voltage) depend mainly on the magnitude of the applied magnetic field. On the other hand, upon cycling the transport current, upward and downward curvatures were observed in the CI and CD branches of the $I - V$ curves, respectively.

The voltage dissipation observed in the $I - V$ curves in Fig. 4.2(a) and Fig. 4.2(b) increases with increasing the magnitude of external magnetic field, which can be attributed to the magnetoresistance effect. However, at $T = 82$ K the $I - V$ curves measured at $H = 20$ mT nearly collapse on the ones at $H = 10$ mT, (Fig. 4.2(c)), although a voltage increase is expected when H is increased from 10 to 20 mT. As a first approximation, this observation can be correlated with the constant flow of flux lines along the sample, and we suggest that the measured voltage falls in the regions where the magnetoresistance does not change, i.e. steady state region.

Figure 4.3 shows the hysteretic $I - V$ curves of the YBCO/Ag sample measured at $T = 84$ K with different sweep rates (dI/dt) varied from 1.25 to 0.312 mA/s for $H = 10$ mT and 20 mT. We note that the line shape of $I - V$ curves dramatically

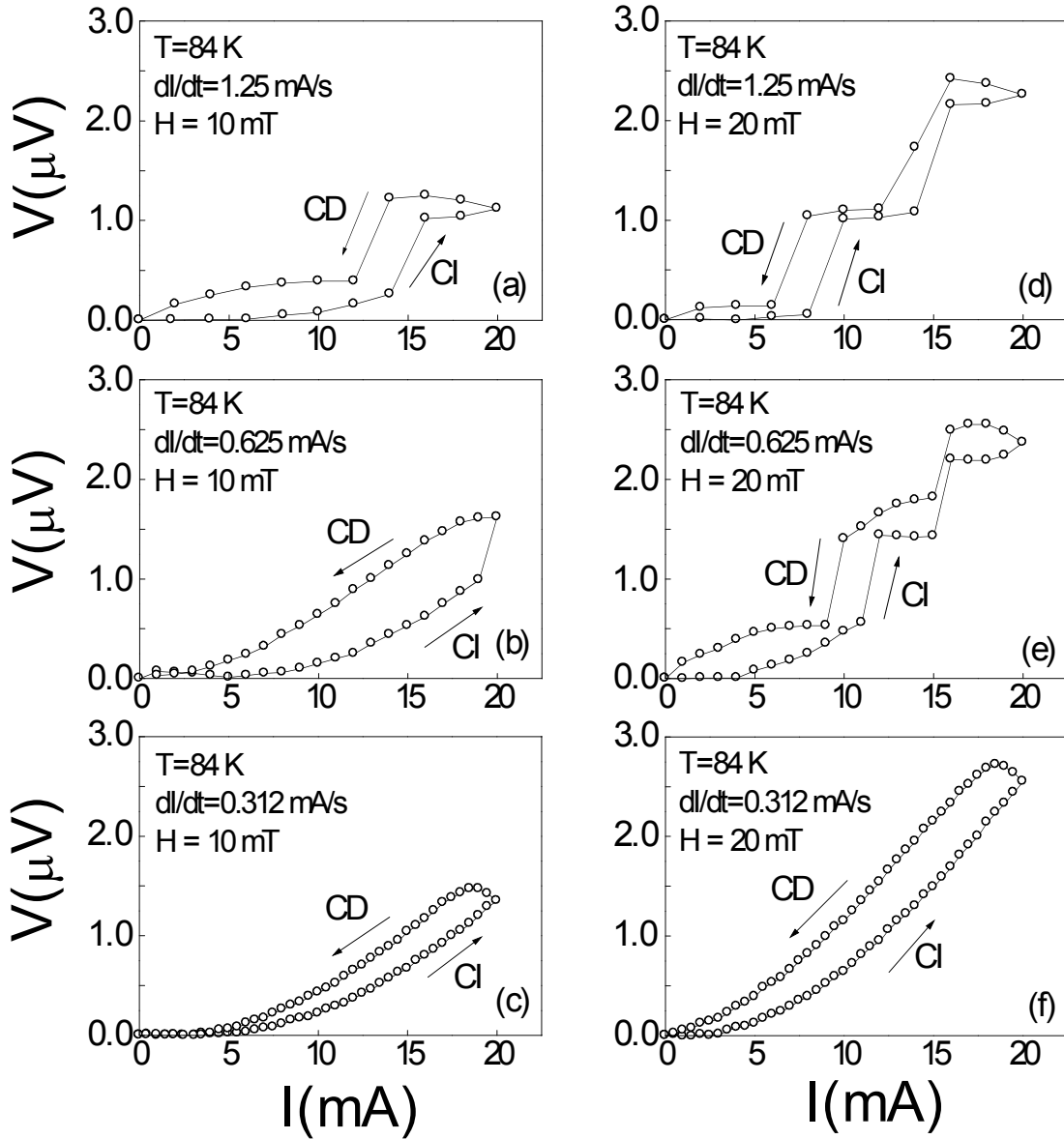


Figure 4.3 The $I - V$ curves of the YBCO/Ag sample measured by the standard procedure at $T = 84$ K and $H = 10$ mT with (a) $dI/dt = 1.25$ mA/s, (b) $dI/dt = 0.625$ mA/s, and (c) $dI/dt = 0.312$ mA/s; at $T = 84$ K and $H = 20$ mT with (d) $dI/dt = 1.25$ mA/s, (e) $dI/dt = 0.625$ mA/s and (f) $dI/dt = 0.312$ mA/s. The arrows show the direction of sweeping of the applied current.

changes by varying dI/dt . Figure 4.3 (a) reveals that the voltage corresponding to the CI branch of the $I - V$ curve measured at $H = 10$ mT increases non-linearly with the current and then a voltage jump occurs at $I \sim 14$ mA. The non-linear behavior is also observed for the CD branch together with a voltage drop at around 12 mA, which can be considered to have the same origin with the voltage jump on the CI branch. On the other hand, as dI/dt is decreased from 1.25 mA/s to 0.312 mA/s, the voltage jumps or drops and plateau regions developing on the $I - V$ curves disappear [Fig. 4.3(c)]. As the external magnetic field is increased from 10 mT to 20 mT, in addition to the enhancement in the measured dissipation, the voltage jumps and drops become more pronounced for both the CI and CD branches of the $I - V$ curves [Figs. 4.3(d)-4.3(f)]. Furthermore, the number of the voltage jumps and drops also increased as compared to those observed at $H = 10$ mT. It seems that, in one hand, the magnitude of external magnetic field provokes the instabilities together with the variation of current sweep rate, in the other hand, it affects directly the line shape of the $I - V$ curves. Finally, the instabilities on the $I - V$ curves measured for $dI/dt = 0.312$ mA/s at $H = 20$ mT in Fig. 4.3(f) are not observed as in the case in Fig. 4.3(c).

In order to study the effect of the maximum current (I_{\max}) on the evolution of the $I - V$ curves, I_{\max} was increased from 20 mA to 40 mA. The measurements were repeated under the same experimental conditions as in Figs. 4.3(d)-4.3(f). It is seen from Figs. 4.4(a)-4.4(c) that the stepwise behavior of the $I - V$ curves remains in the current range 20 – 40 mA. For $dI/dt = 0.312$ mA/s, the number of voltage drops and jumps decreases and the instabilities disappear

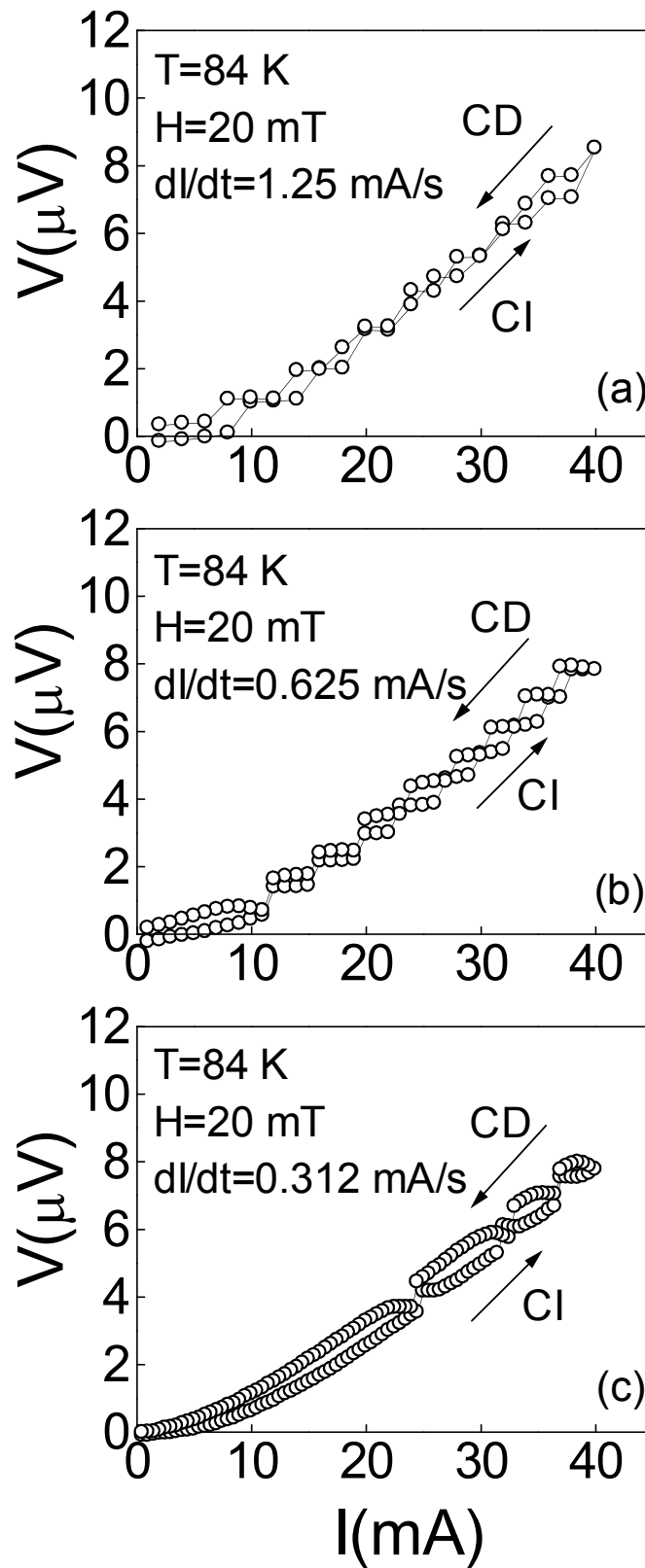


Figure 4.4 The $I-V$ curves of the YBCO/Ag sample measured at $T = 84$ K and $H = 20$ mT by the standard procedure for (a) $dI/dt = 1.25$ mA/s, (b) $dI/dt = 0.625$ mA/s, and (c) $dI/dt = 0.312$ mA/s. The maximum current I_{max} was 40 mA. The arrows show the direction of sweeping of the applied current.

below 20 mA for both the CI and CD branches of the $I - V$ curves. We also observe that the maximum voltage dissipation (V_{\max}) measured at $I_{\max} = 40$ mA is practically independent of the current sweep rate.

Figure 4.5 shows the results of $I - V$ measurements made under the same experimental condition as in Fig. 4.4, but I_{\max} was taken as 50 mA. The $I - V$ curve measured with $dI/dt = 1.25$ mA/s, exhibits a stepwise structure in the whole current range considered. For current sweep rates of 0.625 and 0.312 mA/s, the stepwise behavior becomes more rounded and the $I - V$ curve demonstrates a negative differential resistance.

Figure 4.6 shows a set of $I - V$ curves for the YBCO/Ag sample measured under the same experimental condition as in Fig 4.3, but at a lower temperature ($T = 82$ K) and $I_{\max} = 40$ mA. At this temperature, voltage drops and jumps, and plateau regions develop for both the CI and CD branches of the $I - V$ curves (Figs. 4.6(a)-4.6(c)). As in the case of $I - V$ measurements represented above, the instabilities decrease with decreasing dI/dt . The maximum dissipation measured at $I_{\max} = 40$ mA is essentially independent of dI/dt , for instance, the sample voltage measured at $I_{\max} = 40$ mA is ~ 7 μ V for all current sweep rates employed in the measurements. As the external magnetic field is increased from 10 mT to 20 mT, the voltage instabilities shift to relatively lower values of the applied current (Figs. 4.6(d)-4.6(f)). For instance, for $dI/dt = 0.625$ mA/s, the first voltage jump appears at about 15 mA for the CI branch of the $I - V$ curve measured at $H = 10$ mT (Fig. 4.6(b)) whereas, for $H = 20$ mT, it occurs at about 13 mA (Fig. 4.6(e)).

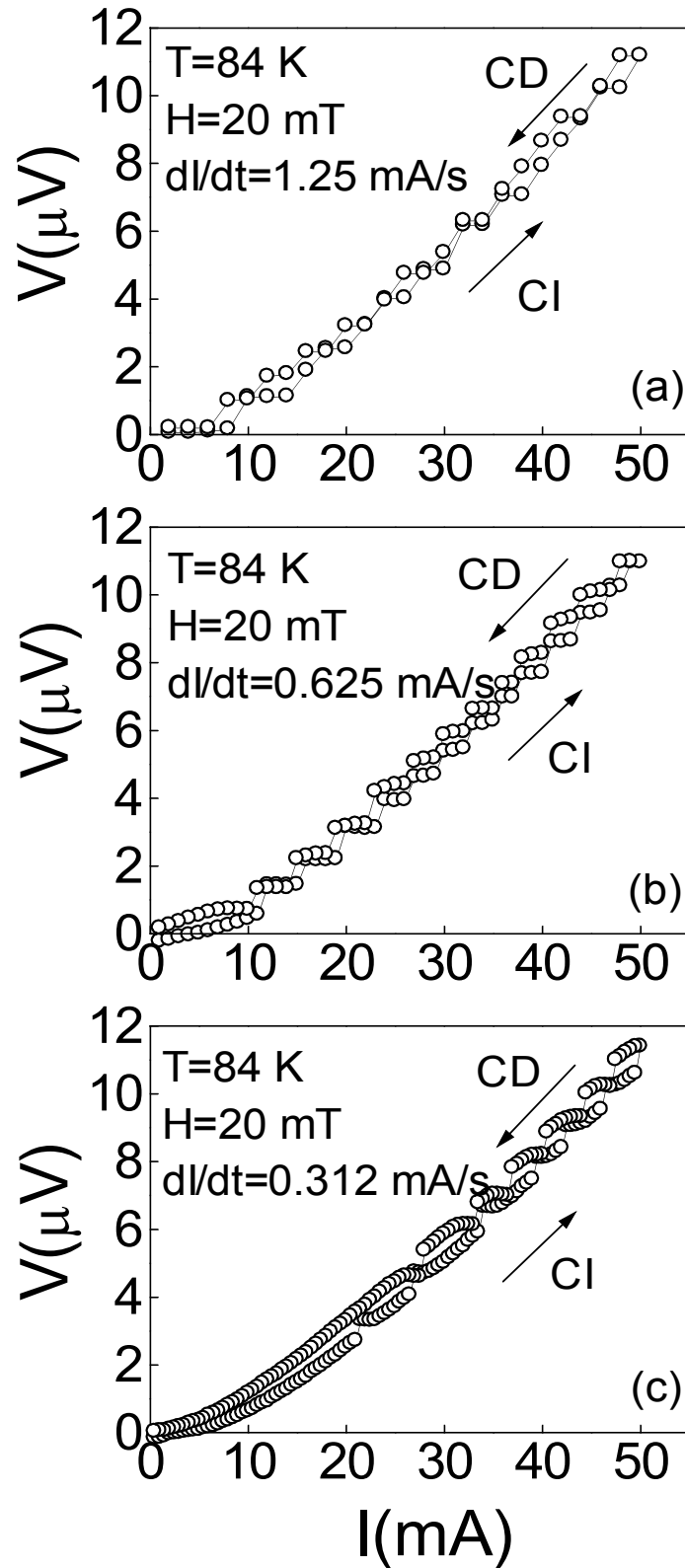


Figure 4.5 The $I - V$ curves of the YBCO/Ag sample measured at $T = 84 \text{ K}$ and $H = 20 \text{ mT}$ by the standard procedure for (a) $dI/dt = 1.25 \text{ mA/s}$, (b) $dI/dt = 0.625 \text{ mA/s}$, and (c) $dI/dt = 0.312 \text{ mA/s}$. The maximum current I_{max} was 50 mA . The arrows show the direction of sweeping of the applied current.

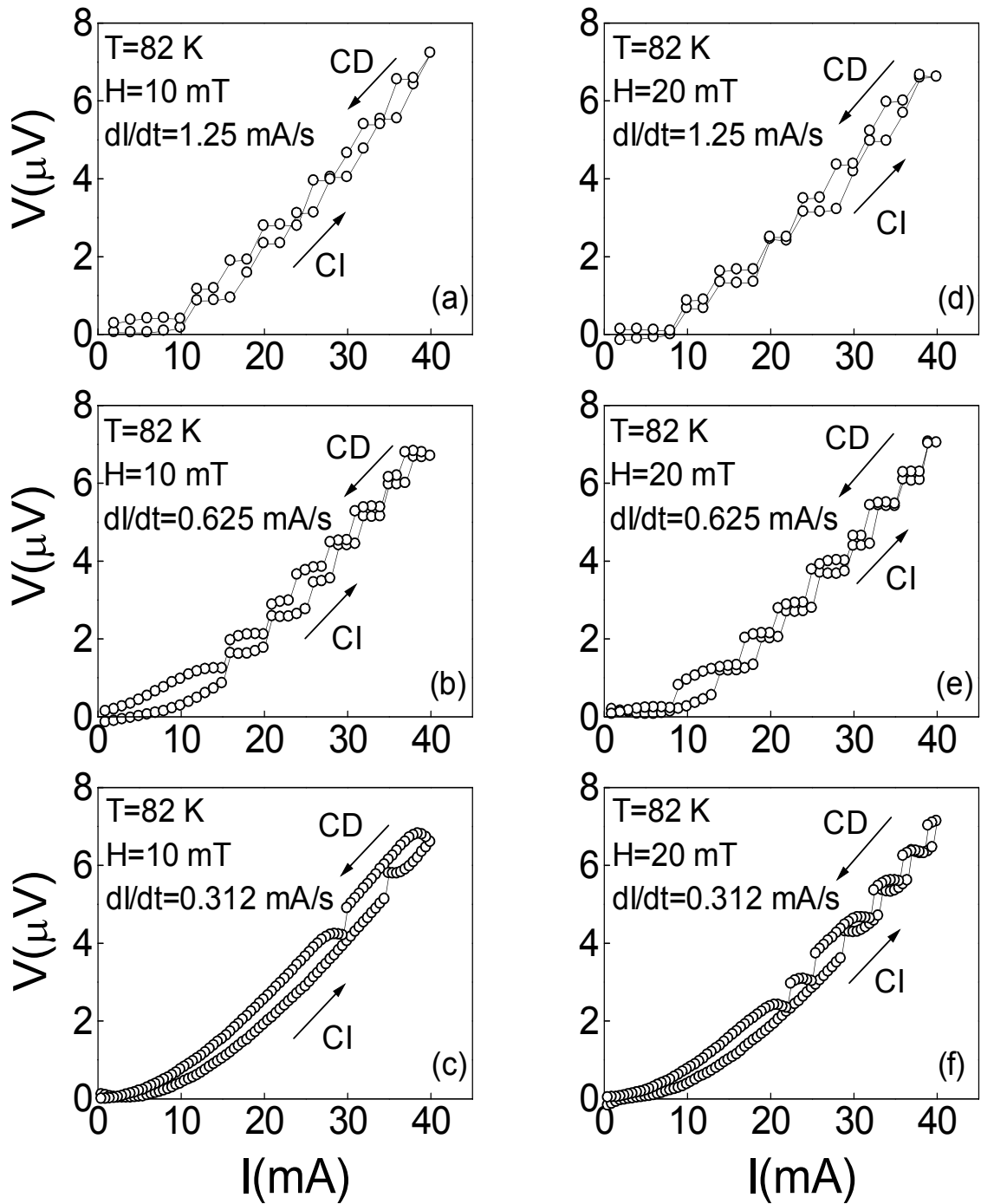


Figure 4.6 The $I - V$ curves of the YBCO/Ag sample measured at $T = 82$ K by the standard procedure for $dI/dt = 1.25, 0.625$ and 0.312 mA/s at $H = 10$ mT **(a)-(c)** and at $H = 20$ mT **(d)-(f)**. The maximum current I_{\max} is taken as 40 mA. The arrows show the direction of sweeping of the applied current.

On the other hand, despite the increase in instabilities, the increase in magnetic field does not cause any difference in the measured dissipation as the current is swept from 0 to $I_{\max} = 40$ mA (Fig. 4.6). This finding supports our suggestion that the measured dissipation associated with flux motion stays within the region where the magnetoresistance does not change, as mentioned earlier (see Fig. 4.2(c)).

Figure 4.7 shows the $I - V$ curves of YBCO/Ag sample measured under the same experimental conditions given in Fig. 4.3. However, the $I - V$ curves in Fig. 4.7 are measured by using the reverse procedure. In the reverse procedure, the applied current is first decreased from I_{\max} to 0 (the reverse current decrease branch, RCD), and then, increased from 0 to I_{\max} (the reverse current increase branch, RCI). Measurements of the $I - V$ curves by the reverse procedure provide a useful tool to study the surface effects and the penetration of the transport current (or associated vortices) from the outer surface of the YBCO/Ag sample.

Figure 4.7, presents the results of such measurements on the YBCO/Ag sample at $T = 84$ K, $H = 10$ and 20 mT, and at the current sweep rate dI/dt varied from 1.25 to 0.312 mA/s. Upon cycling the transport current, the $I - V$ curves exhibit hysteretic behavior as those obtained by using the standard procedure. However, there are some difference between the $I - V$ curves obtained by the standard procedure (Fig. 4.3) and reverse procedure (Fig.4.7). First, the voltage jumps, drops and plateau regions for the RCI and RCD branches are more pronounced than those for the CI and CD braches.

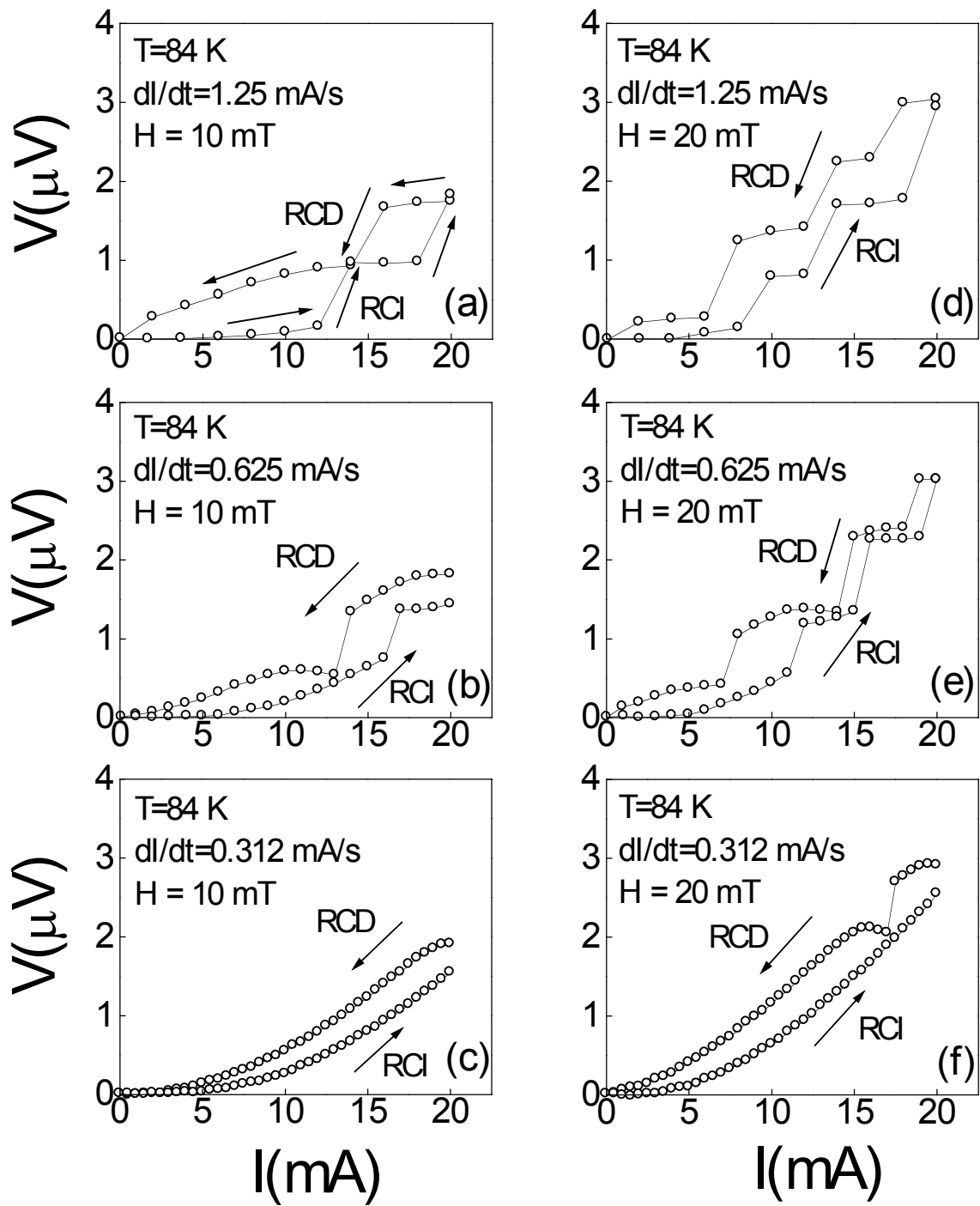


Figure 4.7 The $I-V$ curves of the YBCO/Ag sample measured at $T = 84$ K by the reverse procedure for $dl/dt = 1.25$, 0.625 and 0.312 mA/s at $H = 10$ mT (a)-(c) and at $H = 20$ mT (d)-(f). I_{\max} is taken as 20 mA. The arrows show the direction of sweeping of the applied current.

Second, the measured dissipation in the $I - V$ curves depicted in Figs. 4.7(a) – 4.7(f) is higher than those in Fig. 4.3, especially for $H = 10$ mT. It is also seen from Figs. 4.7(a)-(c) that a measurable voltage ($\sim 2 \mu\text{V}$) develops immediately for all dI/dt values considered as $I_{\text{max}} = 20$ mA is applied to the sample. At the beginning of the RCD branch, the sample voltage achieves values of $\sim 2 \mu\text{V}$ and $\sim 3 \mu\text{V}$ for $H = 10$ and 20 mT, respectively. In addition, the instabilities in the RCD branch measured at $H = 20$ mT for $dI/dt = 0.312$ mA/s begin to appear at about 17 mA.

Figure 4.8 shows the $I - V$ curves measured by using the reverse procedure at $T = 82$ K and $H = 10$ mT, for $dI/dt = 1.25, 0.625$ and $0,312$ mA/s. In order to asses the effect of temperature on the $I - V$ curves, the maximum current I_{max} was taken the same (20 mA) as in Fig. 4.7. It is seen from the RCD branch of the $I - V$ curve in Fig. 4.8(a) that a voltage drop evolves at about $I = 12$ mA. However, for the RCI branch of the same $I - V$ curve, an abrupt voltage jump appears at $I \sim 16$ mA, which is greater than the voltage drop observed for the RCD branch. Differently from the $I - V$ curves measured at $T = 82$ K (Fig. 4.7(a)), both the RCD and RCI branches almost collapse on the same curve for $I < 10$ mA (Fig. 4.8 (a)). For the other current sweep rates, the $I - V$ curves are rather smooth and do not show any voltage drops or jumps upon cycling the applied current. Another observation is that the voltage dissipation measured at $I_{\text{max}} = 20$ mA for the RCI is somewhat smaller than that of measured for RCD one.

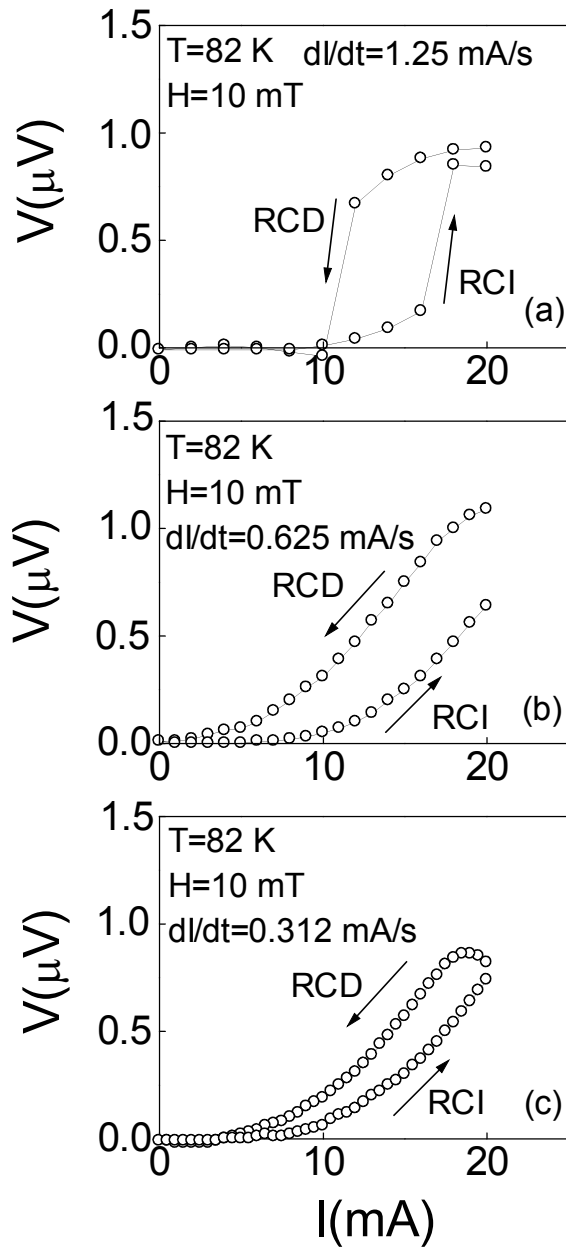


Figure 4.8 The $I - V$ curves of the YBCO/Ag sample measured at $T = 82$ K and $H = 10$ mT by reverse procedure for (a) $dI/dt = 1.25$ mA/s, (b) $dI/dt = 0.625$ mA/s, (c) $dI/dt = 0.312$ mA/s. I_{\max} was 20 mA. The arrows show the direction of sweeping of the applied current.

In order to observe the effect of maximum current I_{\max} on the evolution $I - V$ curves, the applied maximum current was increased from 20 mA to 30 mA. Figure 4.9 shows the $I - V$ curves measured at the same experimental conditions as those in Fig. 4.8. It is observed that there is an increase in the number of

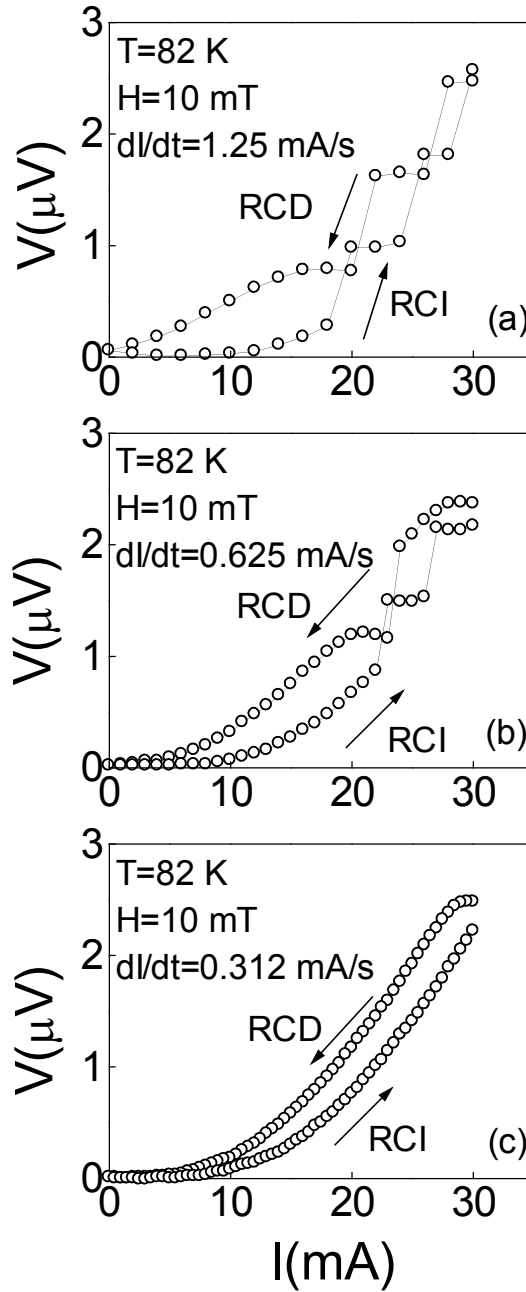


Figure 4.9 The $I - V$ curves of the YBCO/Ag sample measured at $T = 82$ K and $H = 10$ mT by reverse procedure for (a) $dI/dt = 1.25$ mA/s, (b) $dI/dt = 0.625$ mA/s, (c) $dI/dt = 0.312$ mA/s. I_{\max} was 30 mA. The arrows show the direction of sweeping of the applied current.

instabilities on the $I - V$ curves obtained for $dI/dt = 1.25$ and 0.625 mA/s. However, for $dI/dt = 0.312$ mA/s, the $I - V$ curves do not show any instability. The results show that low current sweep rates results in smooth curves of both

RCD and RCI branches. But we expect that the instabilities observed in the $I - V$ curves will begin to appear with increasing the value of I_{\max} .

In line with this expectation, the maximum current I_{\max} was increased from 30 to 50 mA and $I - V$ measurements were carried out at the same experimental conditions considered in Fig. 4.9 by applying $H = 10$ and 20 mT. Figure 4.10 shows the experimental results. The number of instabilities on the RCD and RCI branches of the $I - V$ curves increases as the magnetic field is increased from 10 to 20 mT, and the current values where the instabilities occur shift to lower values. For instance, the first voltage jump on the RCI branch of $I - V$ curve measured for $dI/dt = 0.312$ mA/s at $H = 10$ mT appears at about 43 mA whereas, at $H = 20$ mT, the first voltage jump appears at $I \sim 21$ mA. Thus, the $I - V$ curves exhibit instabilities even at low values of dI/dt . To prevent such instabilities in the $I - V$ curves, it seems that dI/dt should be decreased below 0.312 mA/s for $I_{\max} = 50$ mA. Note also that the $I - V$ curves in Figs. 4.10(d)-4.10(f) are more reversible when compared to those in Figs. 4.10(a)-4.10(c), as the applied magnetic field is increased from 10 mT to 20 mT. More reversibility implies that the flux lines can follow nearly the same flow paths for the RCD and RCI branches and the flux motion associated with those branches does not differ much from each other.

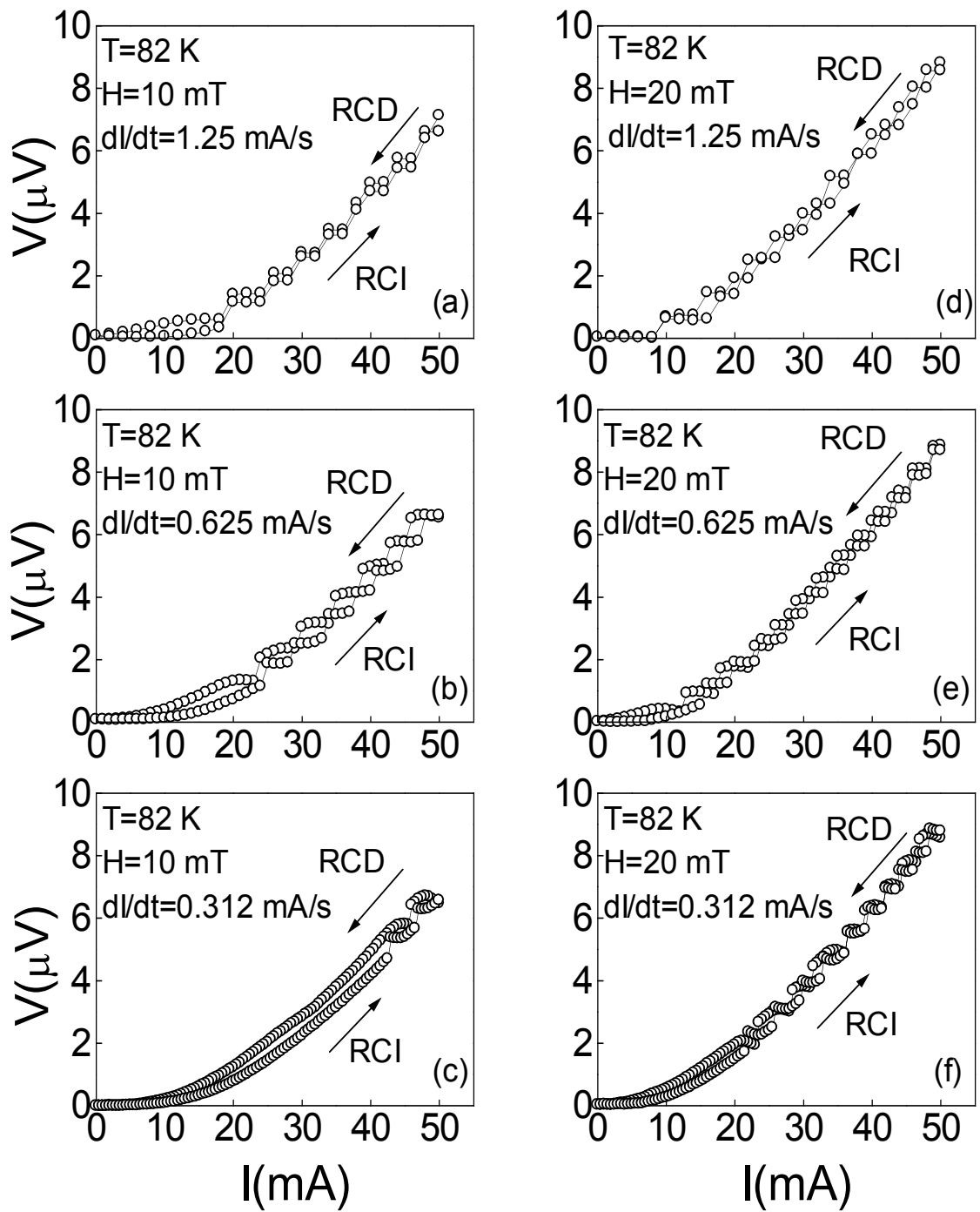


Figure 4.10 The $I - V$ curves of the YBCO/Ag sample measured at $T = 82$ K by reverse procedure for $dI/dt = 1.25, 0.625$ and 0.312 mA/s at $H = 10$ mT **(a)-(c)** and at $H = 20$ mT **(d)-(f)**. I_{\max} was 50 mA. The arrows show the direction of sweeping of the applied current.

4.3 Time Effects and Transport Relaxation Measurements

The steady state response of the polycrystalline YBCO/Ag sample to a driving current can be changed dramatically by increasing the magnitude of the driving current or reducing it to a finite value or interrupting it completely, which leads to several implications on the evolution of the $V - t$ curves. In measuring the $V - t$ curves, a dc driving current I_1 (the initial current) was applied to the sample for a while (i.e., 60 s) to achieve a steady state, and, then, suddenly changed from I_1 to a lower finite value (I_2) which was kept in the rest of the relaxation process, up to 120 s. In the mean time, the sample voltage is recorded continuously as a function of time.

4.3.1 Time evolution of sample voltage ($V - t$ curves)

Figure 4.11 shows the $V - t$ curves measured at $T = 89$ K and $H = 0$ for $I_1 = 50$ mA and $I_2 = 0, 8, 22, 26, 30, 34,$ and 42 mA. As I_1 is applied to the sample, at the beginning of the relaxation process, there is a rapid increase in the sample voltage up to ~ 3 s, and, then, following a small shoulder at ~ 12 s, which can be considered as an onset of a steady state of moving entity, the sample voltage levels off. When the driving current is abruptly reduced from I_1 to I_2 , the sample voltage first drops sharply, then, after a small hump, the sample voltage decreases smoothly, and, for $t > 80$ s, it becomes practically independent of time. However, as the initial current is switched to zero, the sample voltage drops abruptly to zero,

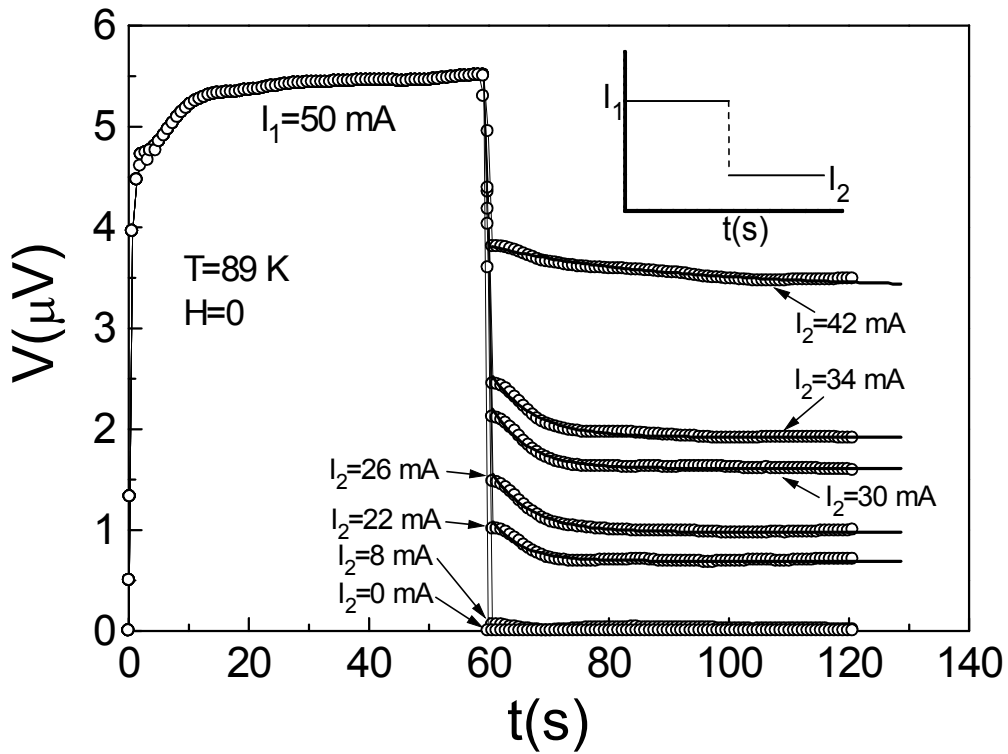


Figure 4.11 The $V - t$ curves of the YBCO/Ag sample measured at $T = 89$ K and $H = 0$ for selected currents of I_2 with $I_1 = 50$ mA. The bold solid lines, for $t > 60$ s, are the curves calculated from Eq. 2.13. The inset shows a schematic representation of the driving current applied to the sample.

without exhibiting any relaxation. This indicates that, within the time response of the experimental set-up used in the study, there is no residual (or trapped) voltage inside the sample to be relaxed. The bold solid lines in Fig. 4.11 (for $t > 60$ s) are the curves calculated from Eq. 2.13 by taking t_0 as fitting parameter.

Figure 4.12 shows the $V - t$ curves of the YBCO/Ag sample measured at $T = 89$ K and $H = 0$, for $I_1 = 40$ mA and $I_2 = 0, 14, 18, 22, 26, 30, 32, 34,$ and 36 mA. At the beginning of the relaxation process, the sample voltage response to the initial current I_1 is similar that in Fig. 4.11. Within about ~ 8 s, the initial rapid increase slows down and levels off at about $t = 12$ s, which implies the presence of a

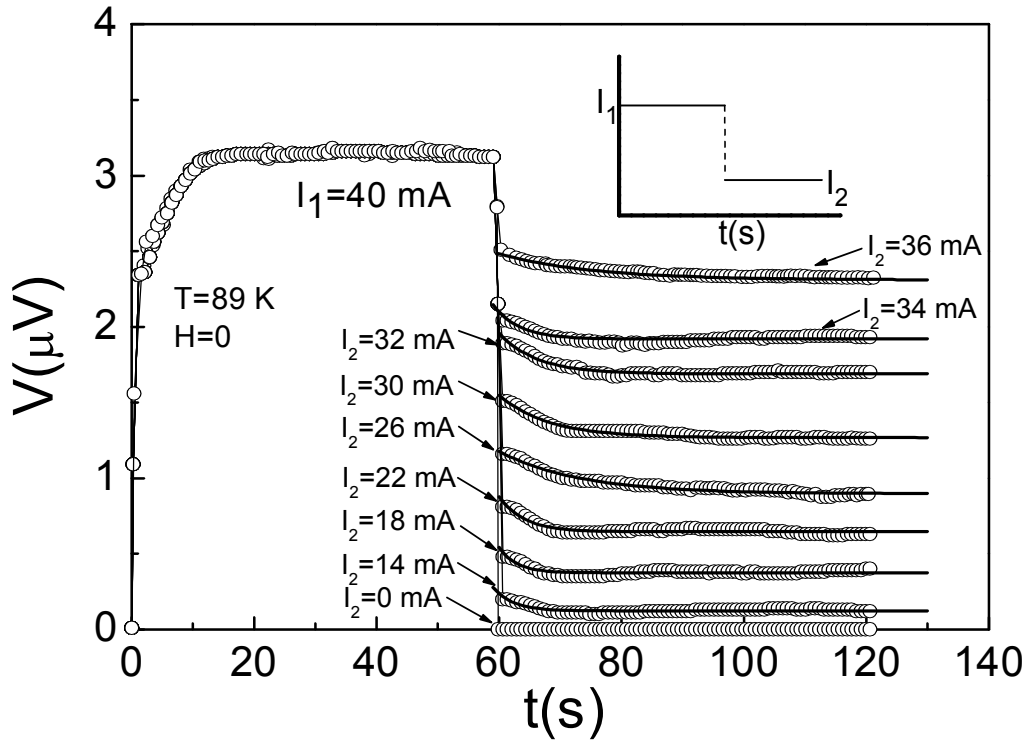


Figure 4.12 The $V - t$ curves of the YBCO/Ag sample measured at $T = 89$ K and $H = 0$ for selected currents of I_2 with $I_1 = 40$ mA. Bold solid lines, for $t > 60$ s, are the curves calculated from Eq. 2.13. The inset shows a schematic representation of applied current.

current-induced correlated motion. When the initial current I_1 is suddenly reduced to I_2 , a sharp drop in the sample voltage is observed and the sample voltage decreases smoothly to a finite value as the time progresses. In addition, there is a hump in the $V - t$ curves at the beginning of relaxation process, for all current values, except $I_2 = 0$ and 36 mA. The bold solid lines in Fig. 4.12 are the curves calculated from Eq. 2.13 by taking t_0 as fitting parameter and $\alpha = 1$.

To further assess the effect of the initial current I_1 , $V - t$ measurements were carried out at a lower value of I_1 . Figure 4.13 presents the $V - t$ curves of the YBCO/Ag sample measured at the same experimental conditions as those in Fig. 4.12, but for $I_1 = 30$ mA and $I_2 = 10, 18, 22$, and 26 mA. Although the general

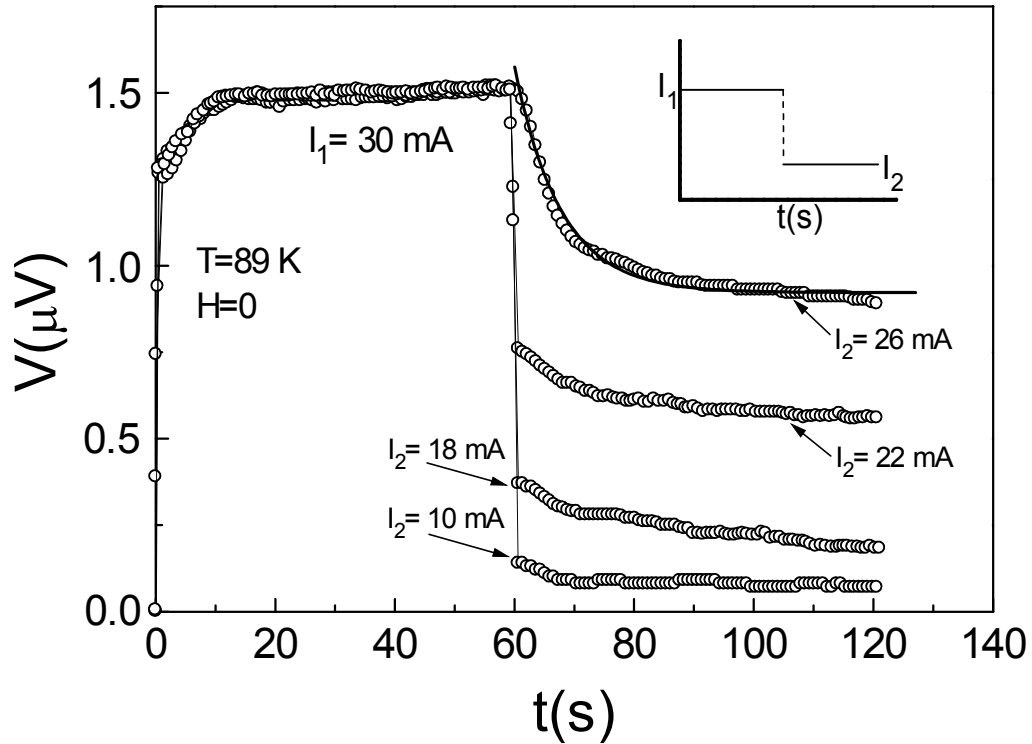


Figure 4.13 The $V - t$ curves of the YBCO/Ag sample measured at $T = 89$ K and $H = 0$ for selected currents $I_1 = 30$ mA and $I_2 = 10, 18, 22$ and 26. Bold solid line, for $t > 60$ s, is the curve calculated from Eq. 2.13. The inset shows a schematic representation of applied current.

behavior of the $V - t$ curves are similar to that in Figs. 4.11 and 4.12, there are some differences to be noted. First, as I_1 is suddenly decreased to $I_2 = 26$ mA, no sharp drop is observed in the sample voltage, which decays smoothly with time. Second, when $I_1 (= 30$ mA) is reduced to I_2 , the humps observed in the $V - t$ curves for high values of I_1 (Figs. 4.11 and 4.12) now disappeared for all values of

I_2 (see Fig. 4.13). In addition, the measured sample voltage tends to decay towards lower dissipation values as the time evolves. This implies that the dynamic process associated with pinning and depinning still continues inside the sample and the process develops in favor of pinning. The bold solid line given in Fig. 4.13 is the curve calculated from Eq. 2.13 by taking t_0 as fitting parameter.

In order to assess the effect of temperature on the evolution of the $V - t$ curves, measurements were performed at $T = 88$ K and $H = 0$, but the other experimental conditions were the same as in Fig. 4.11. Figure 4.14(a) presents the $V - t$ curves of the YBCO/Ag sample measured at 88 K and $H = 0$, for $I_1 = 50$ mA and $I_2 = 46, 42, 38, 34, 30, 18,$ and 0 mA. The initial current I_1 was taken as 50 mA, because for $I_1 < 50$ mA the sample voltage was too small to be measured by the measurement system used in the study. It is seen from Fig. 4.14(a) that there is a gradual non-linear increase in the sample voltage at early times of the relaxation process. As the time progresses, the sample voltage levels off at $t \sim 16$ s. When I_1 is suddenly reduced to I_2 , the sample voltage decreases smoothly with time for all values of I_2 . This is in contrast to the $V - t$ measurements made at $T = 89$ K (see Fig. 4.11), in which the sample voltage showed a sharp drop before decaying. The smooth decay in sample voltage in Fig. 4.14(a), takes a certain time t_s , which depends on the value of I_2 and, then, the voltage becomes independent of time. Here, t_s is the time elapsed from the beginning of the voltage decay to the time where the voltage levels off. The variation of t_s with I_2 is given in Fig. 4.14(b): There is a non-linear relation between t_s and I_2 . The bold solid lines in Fig. 4.14(a) are the curves calculated from Eq.2.13 by taking t_0 as fitting parameter.

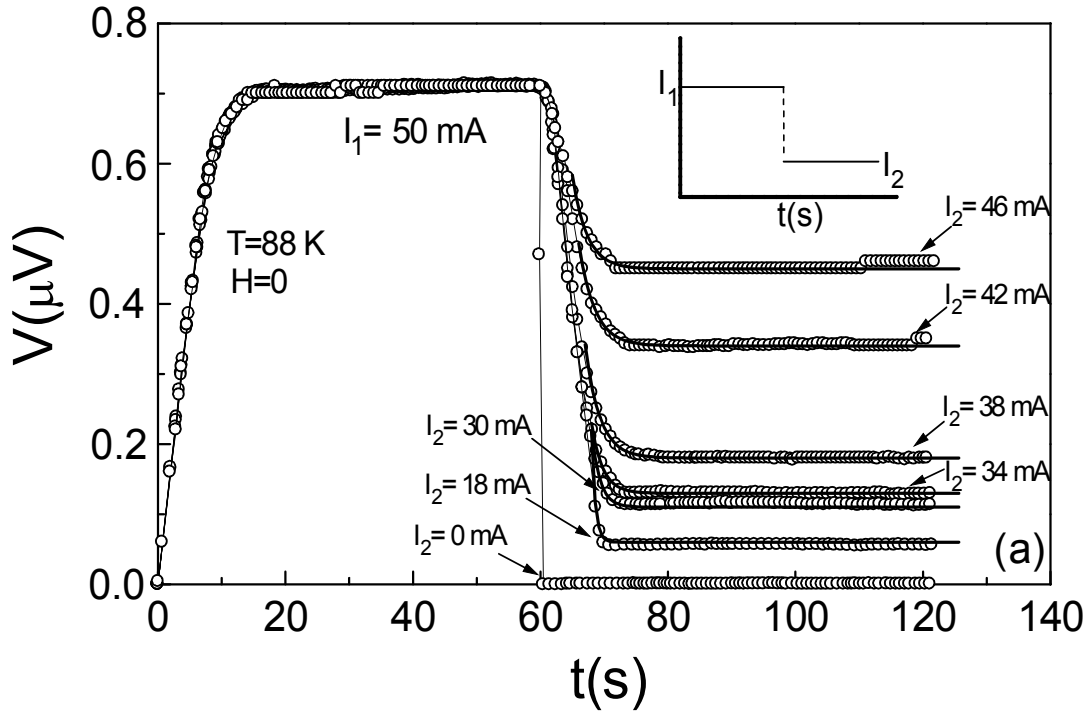


Figure 4.14(a) The $V - t$ curves of the YBCO/Ag sample measured at $T = 88$ K and $H = 0$ for $I_2 = 46, 42, 38, 34, 30, 18,$ and 0 mA. The inset shows a schematic presentation of applied current. Bold solid lines are the curves calculated from Eq. 2.13.

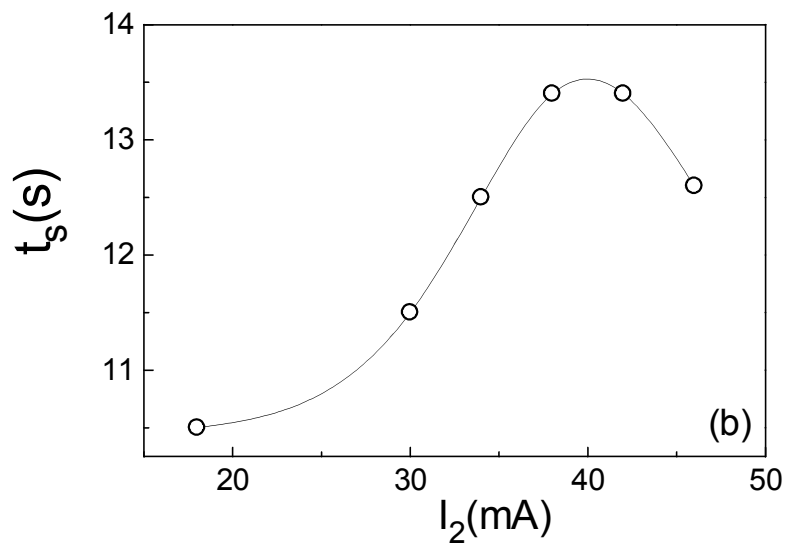


Figure 4.14(b) The variation of time t_s with I_2 . The data are extracted from the $V - t$ curves given in Fig. 4.14(a). The full line through the experimental data is a guide for the eyes.

4.3.2 The effect of external magnetic field on the evolution of $V - t$ curves

The influence of the external magnetic field on the $V - t$ curves can be seen from the Figs. 4.15 – 4.17. Here, low temperature and low initial current values were selected in obtaining the $V - t$ curves, because the voltage dissipation measured under external magnetic field increased markedly when compared to that measured at zero magnetic field.

Figure 4.15(a) presents the $V - t$ curves measured at $T = 85$ K and $H = 10$ mT for $I_1 = 20$ mA and $I_2 = 16$ mA, and 12 mA. At the initial stage of the relaxation process, the voltage rise is quite sharp and the sample voltage levels off within a very short time (less than ~ 1 s) as compared to that extracted from $V - t$ curves measured at $H = 0$ (see Fig. 4.11). When the current is abruptly reduced from I_1 to I_2 , the voltage drops sharply and a steady state is reached rapidly. These observations could be related to destruction of the coherent state of weak link structure due to the application of magnetic field.

Figure 4.15(b) shows the $V - t$ curve measured at the same experimental conditions as in Fig. 4.15(a), but for $I_1 = 6$ mA and $I_2 = 4$ mA. A very rapid voltage rise is observed at the beginning of the relaxation process as in the Fig. 4.15(a). The smooth voltage decay resembles that observed for $V - t$ curves in Fig. 4.13 for $I_2 = 26$ mA and Fig. 4.14(a).

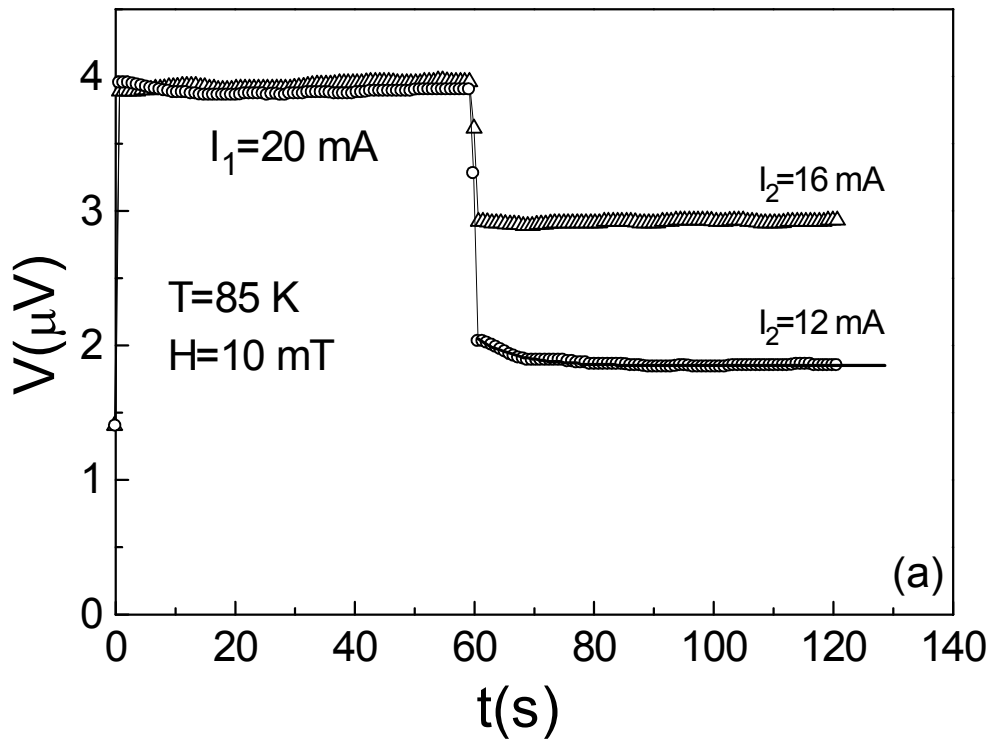


Figure 4.15(a) The $V - t$ curves of the YBCO/Ag sample measured at $T = 85$ K and $H = 10$ mT, for $I_1 = 20$ mA and $I_2 = 12$ and 16 mA. The bold solid line is calculated from Eq. 2.13.

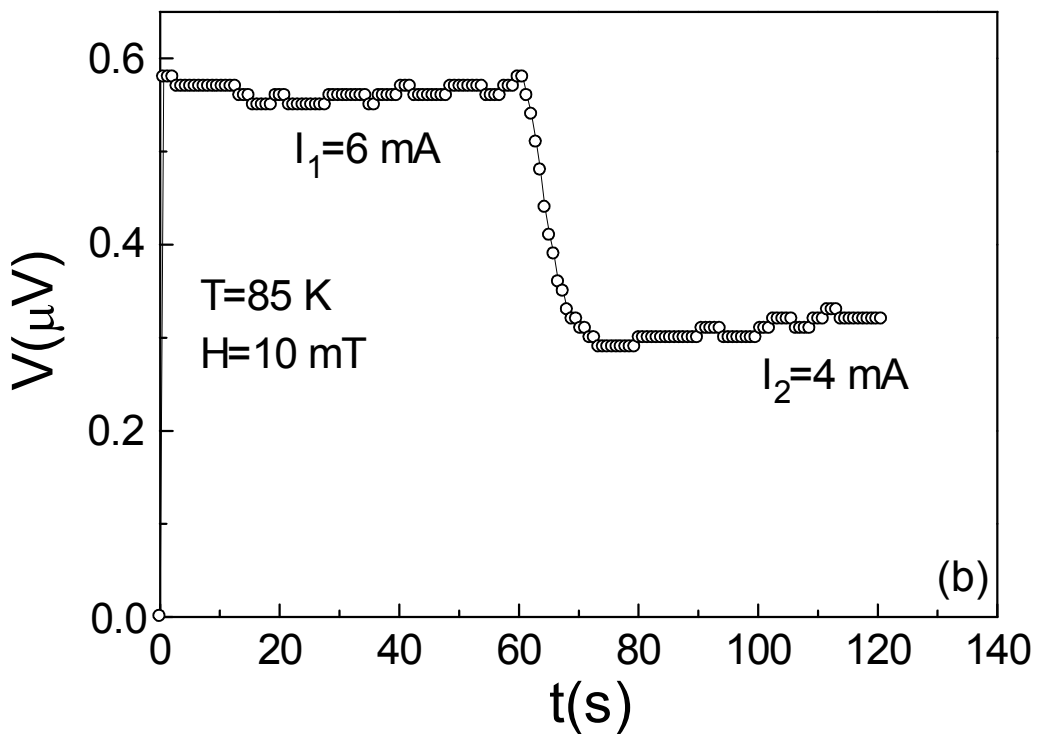


Figure 4.15(b) The $V - t$ curve of the YBCO/Ag sample measured at $T = 85$ K and $H = 10$ mT, for $I_1 = 6$ mA and $I_2 = 4$ mA.

The measurements were performed at the same experimental conditions given in Fig. 4.15(a) but at $T = 84$ K. Figure 4.16 shows the $V - t$ curves of YBCO/Ag measured at $T = 84$ K and $H = 10$ mT for $I_1 = 20$ mA and $I_2 = 12$ mA and 16 mA. The initial increase of the voltage response is very sharp, then the sample

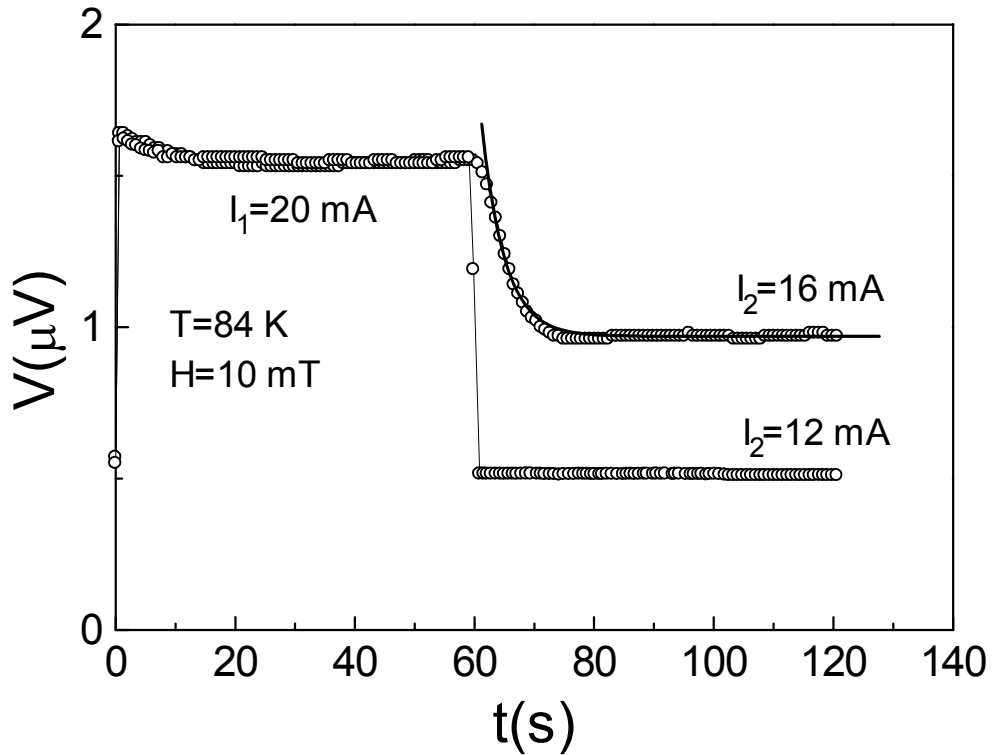


Figure 4.16 The $V - t$ curves of the YBCO/Ag sample measured at $T = 84$ K and $H = 10$ mT for $I_1 = 20$ mA and $I_2 = 12$ and 16 mA. The bold solid line is calculated from Eq. 2.13.

voltage decreases slightly with time and becomes nearly constant up to about 60 s. When I_1 is reduced to $I_2 = 16$ mA, the sample voltage decrease smoothly with a line shape similar to that in $V - t$ curves in Figs. 4.14(a) and 4.15(b). However, for $I_2 = 12$ mA, an abrupt voltage drop, which resembles a switching case, is observed, and the measured dissipation is nearly constant in the time interval of 60 - 120 s, indicating that the relaxation effects disappear.

The external magnetic field is increased to $H = 14$ mT to further observe its effect on the $V - t$ curves. Figure 4.17 shows the $V - t$ curves of YBCO/Ag measured at $T = 84$ K and $H = 14$ mT, for $I_1 = 20$ mA and $I_2 = 4, 8, 12,$ and 16 mA.

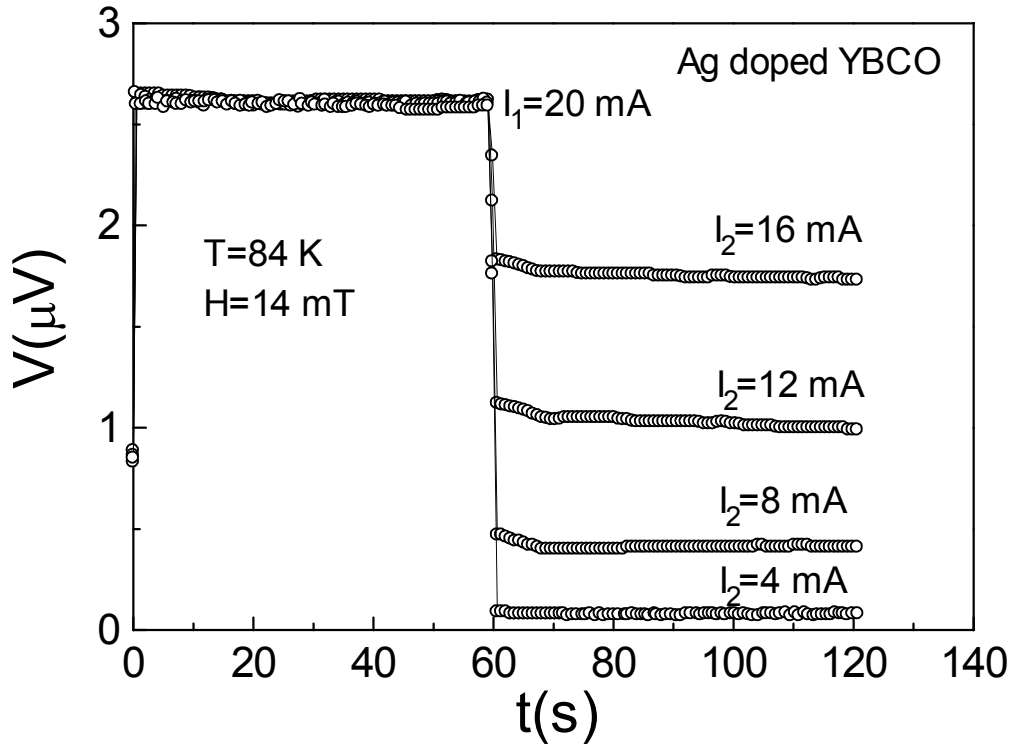


Figure 4.17 The $V - t$ curves of the YBCO/Ag sample measured at $T = 84$ K and $H = 14$ mT for $I_1 = 20$ mA and $I_2 = 4, 8, 12,$ and 16 mA.

The relaxation process at early times is similar to that of observed in Fig. 4.16. However, the initial decrease in the sample voltage in the time interval of 0 - 60 s is not so prominent as in Fig. 4.16. When the initial current I_1 is reduced to I_2 , the sample voltage drops abruptly and the quenched state levels off within a very short time.

4.4 Voltage Oscillations in YBCO/Ag Sample and Influence of Bidirectional Square Wave (BSW) Current on the Evolution of $V-t$ Curves

In this section, we investigate the influence of bi-directional square wave (BSW) current with various periods (P), and amplitude on the voltage-time ($V-t$) curves in polycrystalline YBCO/Ag sample at different temperatures (T) and external magnetic fields (H). It was observed that a non-linear response seen in $V-t$ curves to BSW current with sufficiently short periods or sufficiently low amplitude reflects itself as regular sinusoidal – type voltage oscillations.

4.4.1 Influence of the period of BSW current on $V-t$ curves

Figures 4.18(a) - 4.18(d) illustrate the time evolution of the sample voltage measured at $T = 89$ K for a BSW current of amplitude 15 mA at periods $P_1 = 10, 14, 20$ and 40 s at zero magnetic field. The upper panel in Fig. 4.18 depicts the time dependence of the driving current. The sample voltage response to the BSW current evolves in the shape of regular sinusoidal voltage oscillations for all periods, except the one for $P_1 = 40$ s. The $V-t$ curve measured for BSW current with $P_1 = 40$ s (Fig. 4.18(d)) exhibits oscillations resembling the variation of BSW current with time (Fig. 4.18(a)). It is also observed that the amplitude of voltage oscillations increases gradually with increasing the period P_1 , which can be attributed to the relaxation effects intervening during the process. In addition, the difference between the periods of the BSW current drive and sample voltage response is negligibly small, which can cause a phase difference between them.

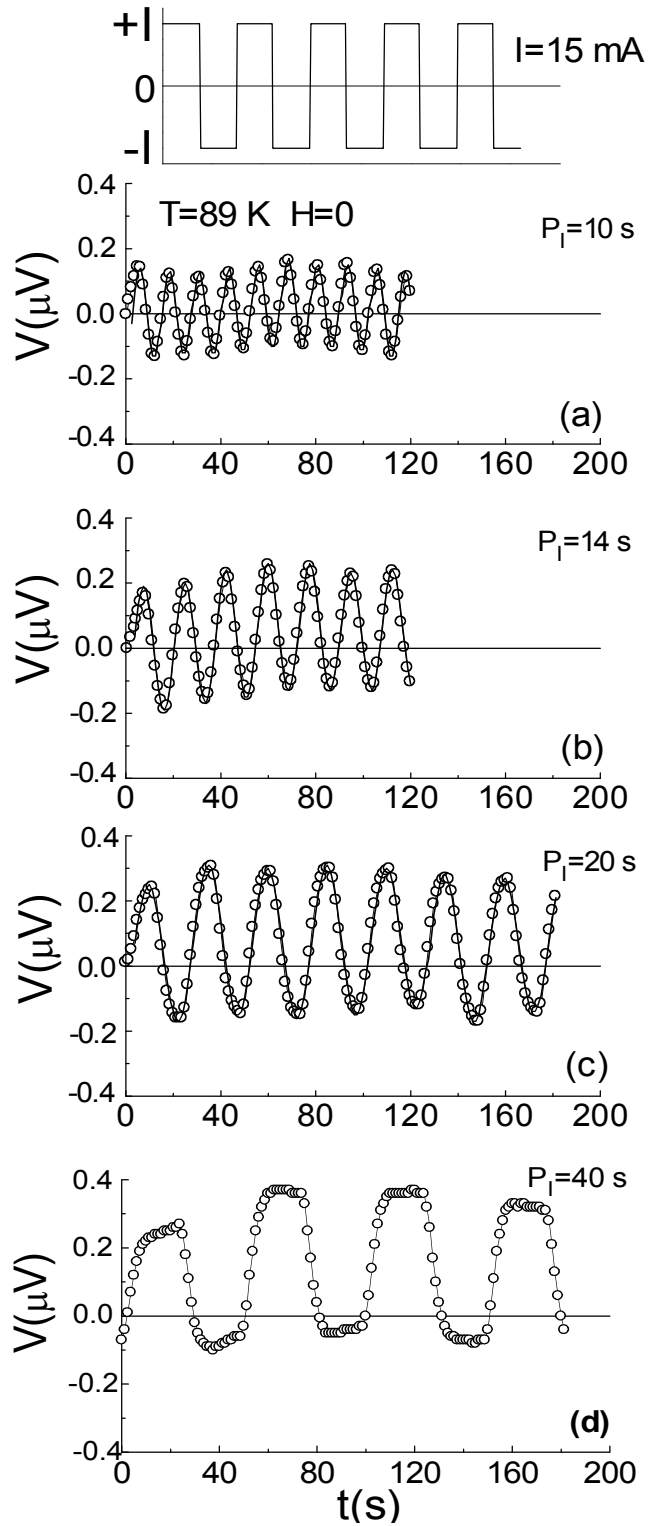


Figure 4.18 Time evolution of the sample voltage measured for a BSW current with amplitude $I = 15 \text{ mA}$ and period P_i : **a)** 10 s, **b)** 14s, **c)** 20 s, and **d)** 40 s. The measurements were made at $T = 89 \text{ K}$ and $H = 0$. The top panel shows schematically the BSW current applied to the sample.

To assess the influence of the amplitude of BSW current on the evolution of voltage oscillations, $V-t$ measurements were carried out at $T = 89$ K and $H = 0$ for BSW current with a period $P_1 = 20$ s and amplitudes of $I = 16$ mA and 18 mA (Fig. 4.19). Figure 4.19(a) shows the regular sinusoidal-type voltage oscillations evolving for $I = 16$ mA, which are similar to those in Figs. 4.18(a)-4.18(c). The current-induced oscillations are essentially symmetric with respect to zero axis, and the measured voltage amplitude is about $0.3 \mu\text{V}$. The $V-t$ curve measured for

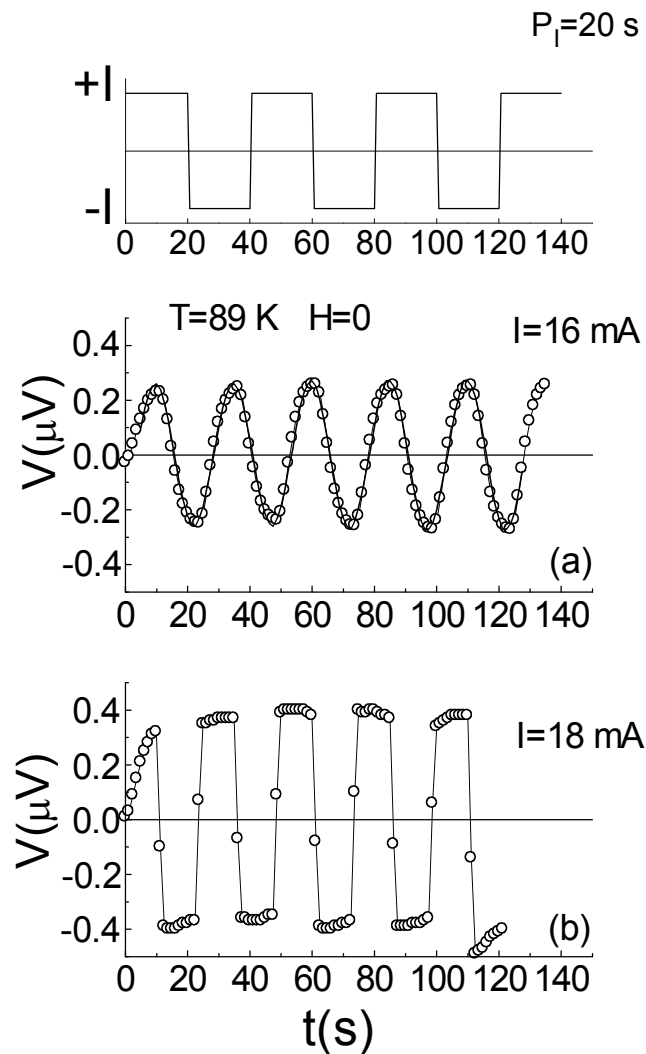


Figure 4.19 Time evolution of the sample voltage measured at $T = 89$ K and $H = 0$ for BSW current with a period $P_1 = 20$ s and amplitudes **a)** $I = 16$ mA, **b)** $I = 18$ mA. The top panel represents schematically the BSW current applied to the sample.

$I = 18$ mA (Figure 4.19(b)) reveals that the amplitude of voltage oscillations increased slightly and the line shape of voltage oscillations resembles that of the BSW current in time.

The effect of the external magnetic field (H) on the evolution of the voltage oscillations is demonstrated in Fig. 4.20. The measurements were performed at $T = 89$ K for external magnetic fields of $H = 10, 16$ and 20 mT. The amplitude and period of the BSW current were $I = 4$ mA and $P_1 = 10$ s, respectively. The $V - t$ curve measured at $H = 10$ mT exhibits sinusoidal-type regular voltage oscillations (Fig 4.20(a)). However, the line shape of the oscillations in the $V - t$ curves measured for $H = 14$ and 16 mT differs from that measured for $H = 10$ mT. Figures 4.20 (b) and 4.20(c) demonstrate that the voltage response of the sample evolves in two stages. In the early stage of the voltage response, the oscillations have the regular sinusoidal-type line shape with a low amplitude of ~ 0.2 μ V, and, as the time progresses, the oscillations change their character. The first voltage jump (or drop) occurs at ~ 38 s and ~ 43 s on the $V - t$ curves measured at $H = 16$ mT and $H = 20$ mT, respectively. After the time values where the voltage jump (or drop) occurred, the time variation of the voltage response of the sample (with a relatively larger amplitude of ~ 0.5 μ V) resembles the line shape of the BSW current.

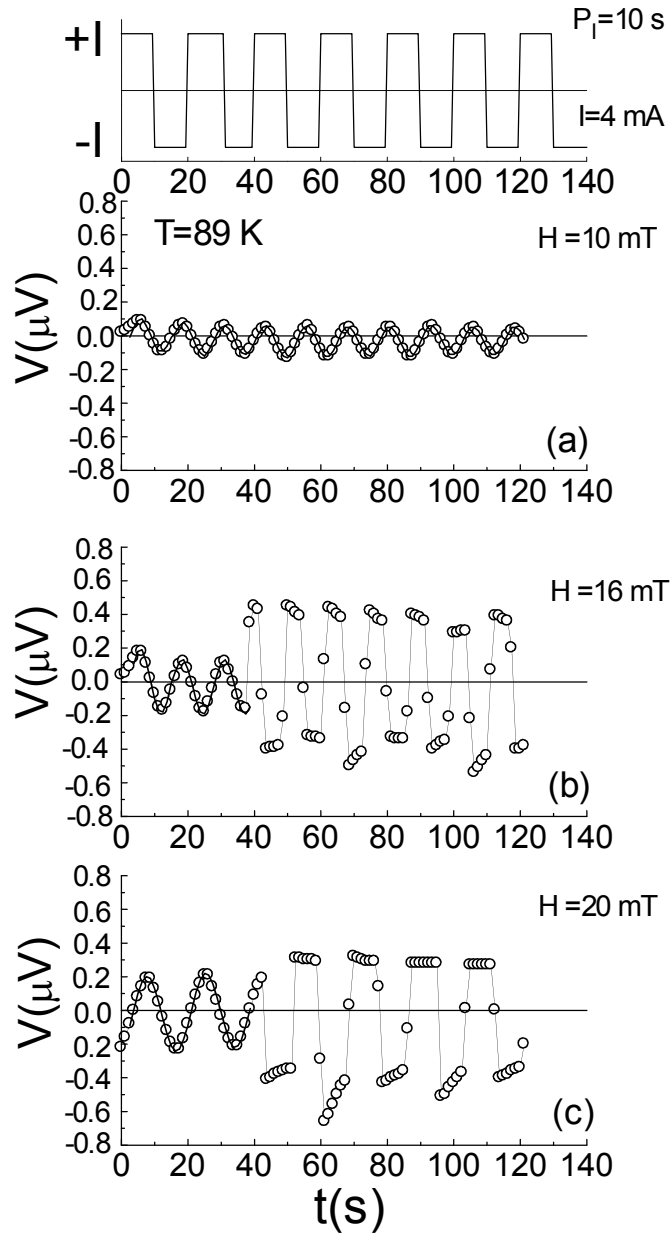


Figure 4.20 Time evolution of the sample voltage measured for BSW current (with amplitude $I = 4$ mA and period $P_1 = 10$ s) at $T = 89$ K and external magnetic fields: **a)** $H = 10$ mT, **b)** $H = 16$ mT, and **c)** $H = 20$ mT. The top panel shows schematically BSW current.

4.5 Magnetovoltage ($V - H$ Curves) Measurements

The magnetovoltage ($V - H$ curves) measurements on the YBCO/Ag were carried out for a constant dc transport current (I) by sweeping the external magnetic field

up [field increased branch (FIB) of the forward region (FR)] and down [field decreased branch (FDB) of the forward region (FR)] in the range 0 – 60 mT. The $V - H$ curve measurements were also made, after the polarity of the magnetic field is reversed [reverse region (RR)]. In all $V - H$ measurements, the applied magnetic field was perpendicular to the transport current ($\vec{H} \perp \vec{I}$). The $V - H$ curves were measured at selected values of temperature, transport current, and magnetic field sweep rate (dH/dt).

4.5.1 Hysteresis effects in the $V - H$ curves measured at different sweep rates of the external magnetic field (dH/dt)

Figure 4.21(a) shows the hysteretic $V - H$ curves measured at $T = 88$ K for selected values of the dc transport current $I = 10, 15, 20, 30,$ and 40 mA with a fixed magnetic field sweep rate $dH/dt = 0.50$ mT/s. The measurements were carried out in five stages for each value of I . The corresponding stages are observed better in the replotted of $V - H$ curve taken for $I = 20$ mA in Fig. 4.21(b). The external magnetic field is cycled up (FIB) and down (FDB) in the FR and, then, the external magnetic field is cycled up and down in the RR. In the final stage, the magnetic field was increased from 0 to 60 mT (FIB in the FR) and the measurement was finished at $H_{\max} = 60$ mT. In the FR, at the beginning of the measurements for FIB, the $V - H$ curve starts from zero for all current values and reaches a nearly steady state as the magnetic field is increased towards 60 mT. As the magnetic field is decreased from $H_{\max} = 60$ mT to 0, for the FDB in the FR,

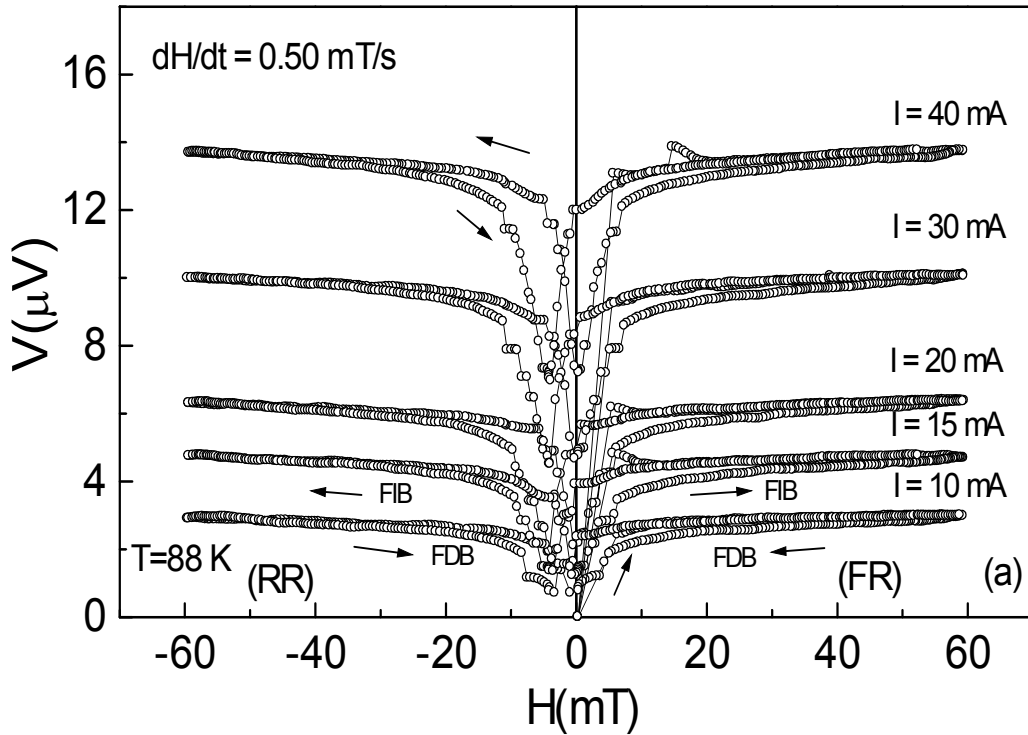


Figure 4.21(a) Magnetovoltage ($V - H$) curves of the YBCO/Ag sample measured at $T = 88$ K for selected values of the transport current $I = 10, 15, 20, 30$ and 40 mA, with a fixed magnetic field sweep rate $dH/dt = 0.50$ mT/s. The arrows show the direction of sweeping of the external magnetic field.

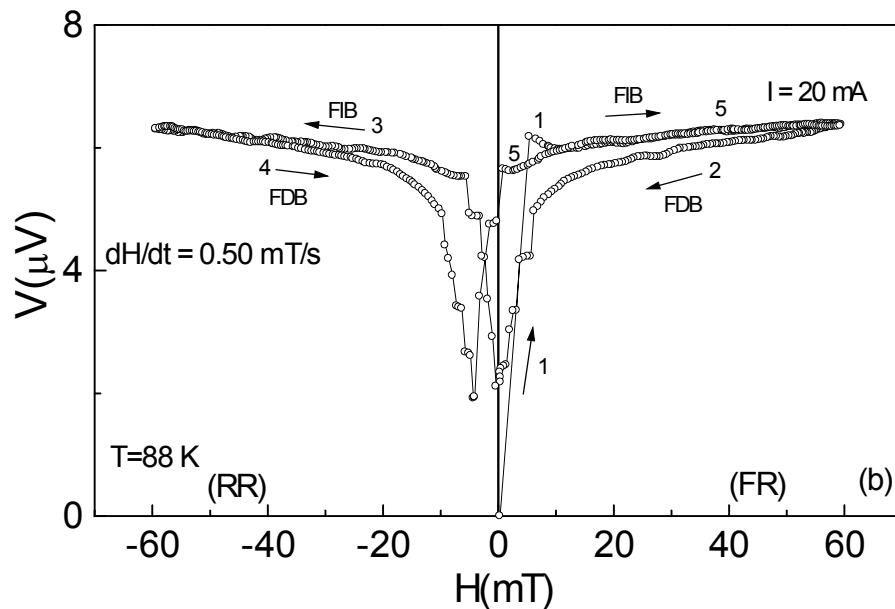


Figure 4.21(b) Replotted of magnetovoltage ($V - H$) curve given in Fig. 4.21(a) for better observation of the stages of hysteresis cycle. The current is taken as $I = 20$ mA.

a clockwise (cw) hysteresis effect appears over the whole magnetic field range considered and the sample stays in a resistive state down to $H = 0$. We note that, for $H > 30$ mT, the $V - H$ curves are essentially reversible. As the magnetic field is decreased down to zero (FDB in the FR), the measured sample voltage dissipation does not become zero. This finding indicates that there is a residual voltage at $H = 0$ which increases with increasing the transport current from 10 to 40 mA.

A similar case is observed in the reverse region (RR) where the polarity of magnetic field is reversed. In the third stage of $V - H$ curves, a non-linear increase in the measured voltage dissipation is observed and voltage dissipation becomes approximately constant as in the FR. In the fourth stage of $V - H$ loops, the measured dissipation decreases with decreasing the magnitude of \vec{H} in the counterclockwise (ccw) direction and passes through a minimum before \vec{H} becomes zero. After the minimum value, although $|\vec{H}|$ is decreased, the sample voltage increases non-linearly and reaches a maximum value at $H = 0$. In fifth stage of the evolution of hysteresis loops where the magnetic field is again reversed (FR), the sample voltage increases non-linearly with increasing H and collapses on the FIB of the first stage. After the fifth stage, whole plot of hysteresis loop is completed (see Fig. 4.21(b)). Note that the voltage drops and jumps evolve at low magnetic field values.

In order to assess the effect of dH/dt on the $V - H$ curves, dH/dt was increased and the measurements described in Fig. 4.21 were repeated. The $V - H$ curves

measured at $T = 88$ K for $I = 15, 20, 30$ and 40 mA with $dH/dt = 1.30$ and 2.60 mT/s are presented in Figs. 4.22 and 4.23, respectively. The $V - H$ curves in Fig. 4.22 exhibit a similar behavior to those in Fig. 4.21(a). In other words, increasing dH/dt from 0.50 mT/s to 1.30 mT/s does not cause any pronounced change in the line-shape of the $V - H$ curves. However, we note that an increase in dH/dt results

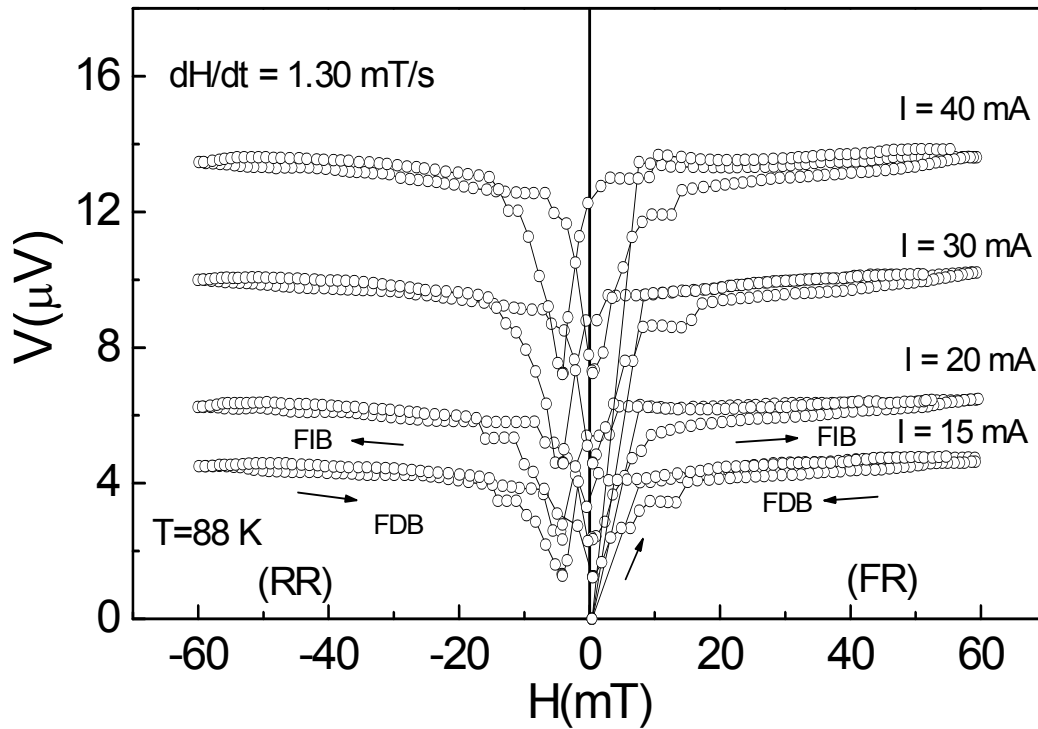


Figure 4.22 Magnetovoltage ($V - H$) curves of the YBCO/Ag sample measured at $T = 88$ K for selected values of the transport current $I = 10, 15, 20, 30$ and 40 mA, with a fixed magnetic field sweep rate $dH/dt = 1.30$ mT/s. The arrows show the direction of sweeping of the external magnetic field.

in increase in the number of the instabilities in the $V - H$ curves. It is seen from the $V - H$ curves given in Fig. 4.23 that the voltage drops and jumps and also the plateau regions are quite prominent. In addition, a comparison of $V - H$ curves in Figs. 4.21-4.23 with each other reveals that the voltage dissipations measured at

given values of I and H are practically independent of dH/dt in the range 0.50-2.60 mT/s.

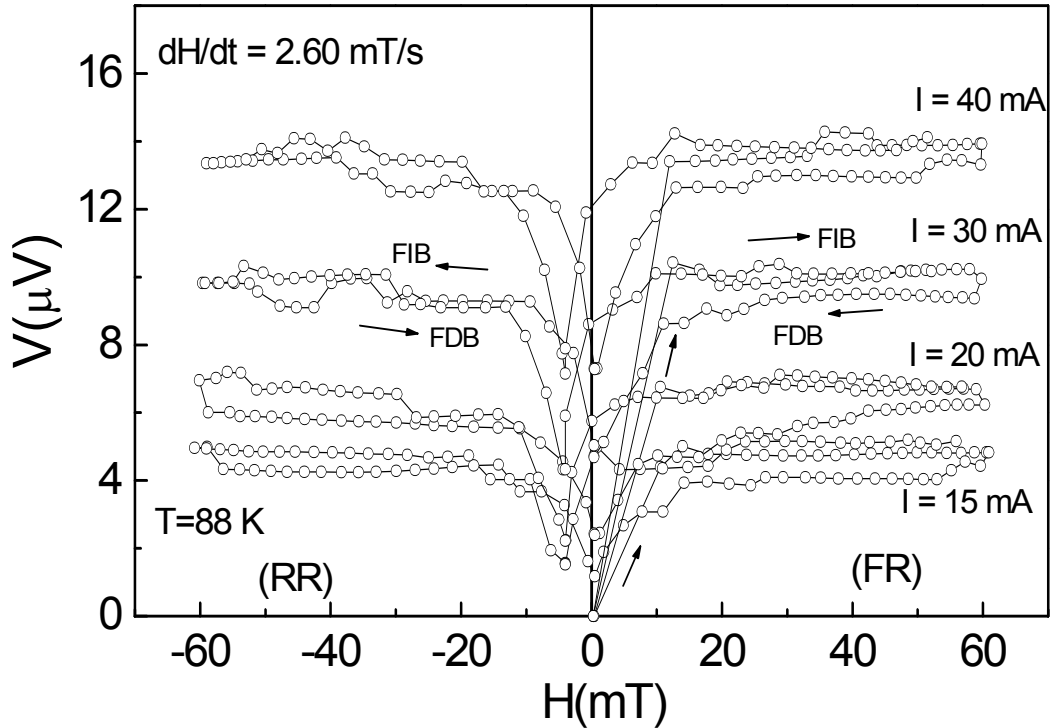


Figure 4.23 Magnetovoltage ($V - H$) curves of the YBCO/Ag sample measured at $T = 88$ K for selected values of the transport current $I = 10, 15, 20, 30$ and 40 mA, with a fixed magnetic field sweep rate $dH/dt = 2.60$ mT/s. The arrows show the direction of sweeping of the external magnetic field.

In order to assess the effect of temperature on the $V - H$ curves, the temperature was decreased from 88 to 84 K. Figures 4.24-4.26 show the $V - H$ curves measured at 84 K for $I = 30, 40, 50,$ and 60 mA and $dH/dt = 0.50, 1.30$ and 2.60 mT/s, respectively. As the temperature is decreased from 88 to 84 K, the measured voltage dissipation decreases. The $V - H$ curves are not reversible in contrast to those in Figs. 4.21 and 4.22. We observe significant increase in

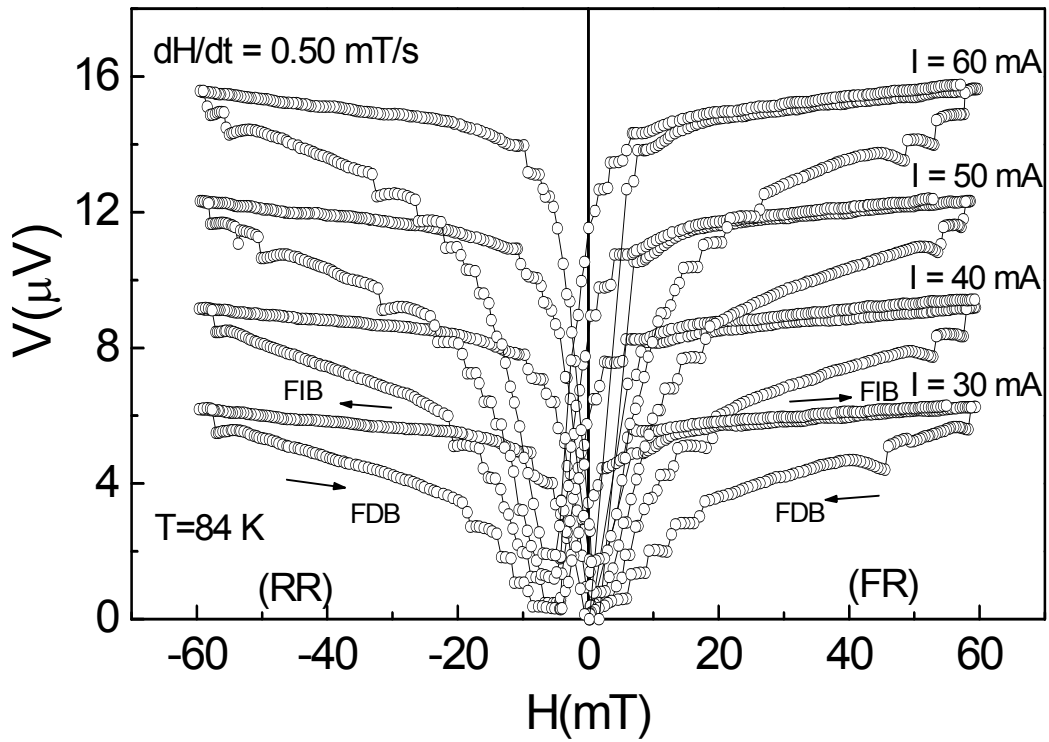


Figure 4.24 Magnetovoltage ($V-H$) curves of the YBCO/Ag sample measured at $T = 84$ K for $I = 30, 40, 50$ and 60 mA, and $dH/dt = 0.50$ mT/s. The arrows show the direction of sweeping of the external magnetic field.

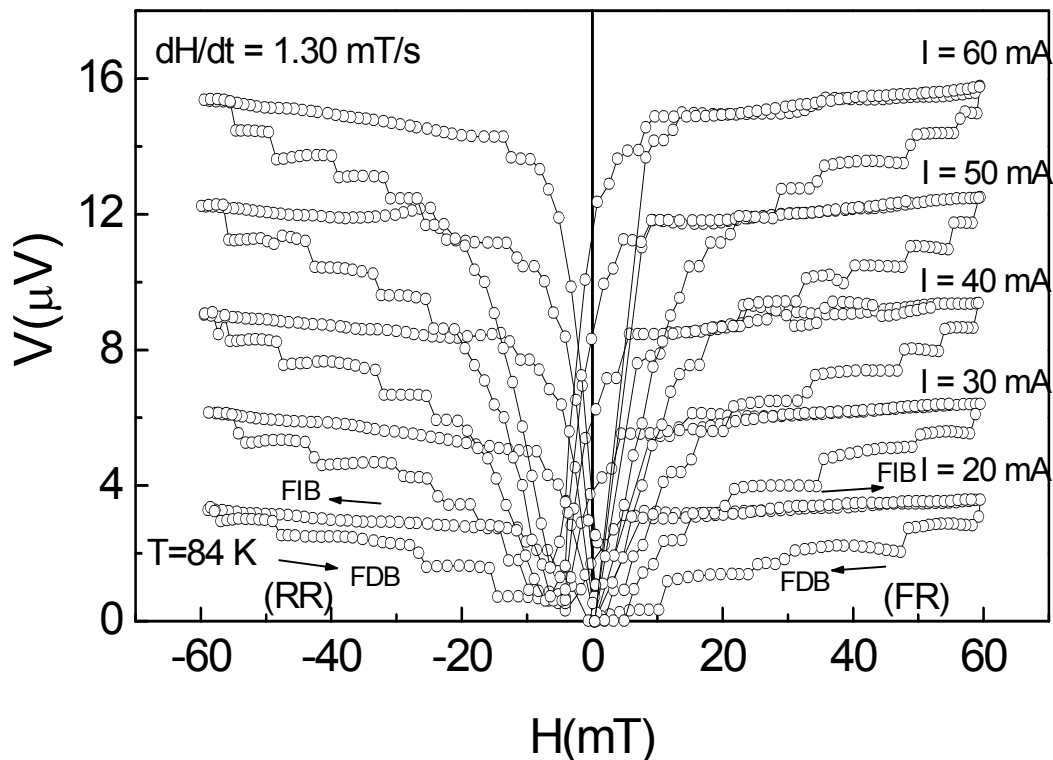


Figure 4.25 Magnetovoltage ($V-H$) curves of the YBCO/Ag sample measured at $T = 84$ K for $I = 20, 30, 40, 50$ and 60 mA, and $dH/dt = 1.30$ mT/s. The arrows show the direction of sweeping of the external magnetic field.

irreversibilities and an enhancement in the height of hysteresis loop. In Fig. 4.24, it is seen that the instabilities observed in the $V - H$ curves become more frequent at low magnetic field in the range $-20 \text{ mT} < H < 20 \text{ mT}$. As the magnetic field approaches to 60 mT, the only instabilities that remain are the voltage drops in the FDBs. However, the voltage dissipation measured for the FIBs varies smoothly with increasing H . At higher values of dH/dt , in addition to the voltage drops and jumps, we see that wide voltage plateau regions develop in the $V - H$ curves. Figure 4.25 shows that the voltage drops and plateaus are more prominent than those observed in Fig. 4.24. The voltage instabilities and voltage plateau regions are observed in all branches of the $V - H$ curves measured with $dH/dt = 2.60 \text{ mT/s}$ (Fig. 4.26).

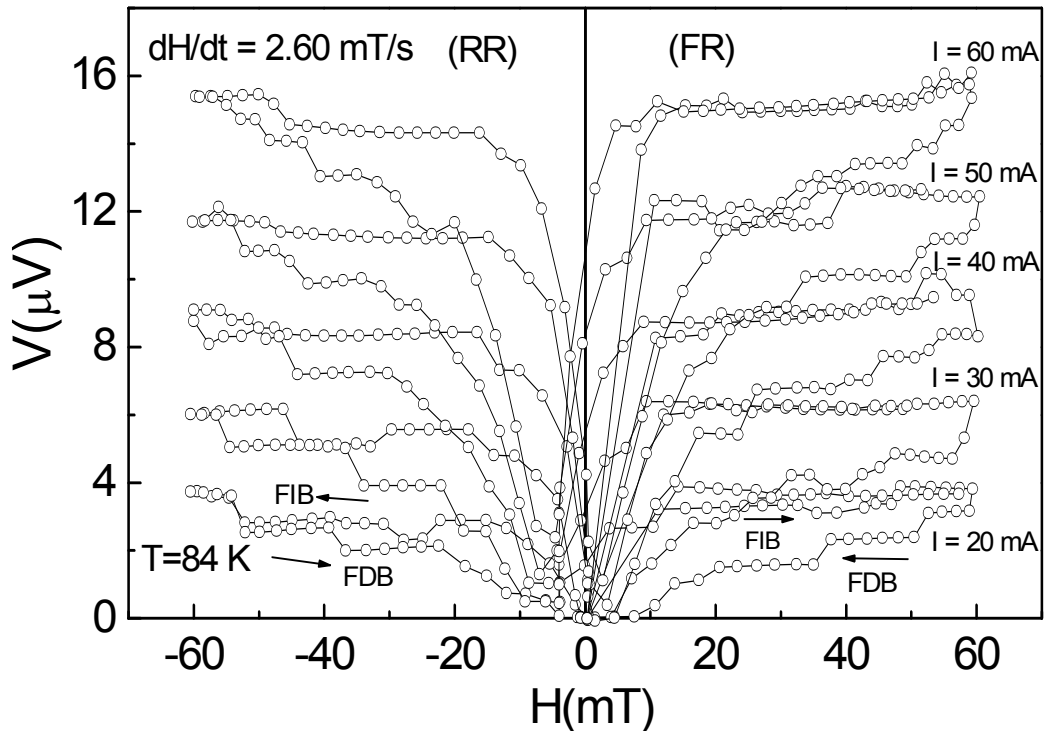


Figure 4.26 Magnetovoltage ($V - H$) curves of the YBCO/Ag sample measured at $T = 84 \text{ K}$ for $I = 20, 30, 40, 50$ and 60 mA , and $dH/dt = 2.60 \text{ mT/s}$. The arrows show the direction of sweeping of the external magnetic field.

Figures 4.27-4.29 show the $V-H$ curves measured at 82 K for $I = 20, 30, 40, 50,$ and 60 mA, and $dH/dt = 0.50, 1.30$ and 2.60 mT/s, respectively. The $V-H$ curves exhibit several different features as functions of dH/dt and transport current. For the $V-H$ curves measured with $dH/dt = 0.50$ mT/s and $I = 20$ and 30 mA (see Fig. 4.27) the variation of measured dissipation with H is smooth with a few voltage drops and jumps just below 60 mT. The number of the voltage drops in the FDBs in the forward region (FR) and reverse region (RR) tends to increase with increasing the transport current (see for instance the FDB of $V-H$ curve for $I = 60$ mA). In addition, as the magnetic field is decreased, the voltage measured for the FIB in FR becomes zero at $H \sim 8$ mT, and 3 mT for $I = 20$ mA and $I = 30$

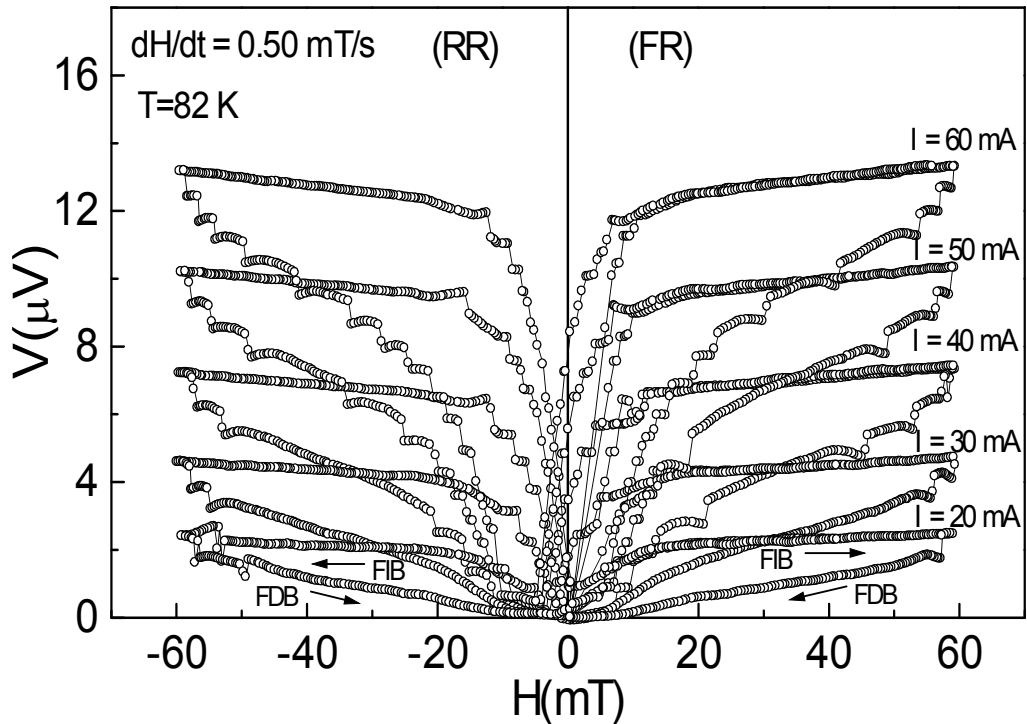


Figure 4.27 Magnetovoltage ($V-H$) curves of the YBCO/Ag sample measured at $T = 82$ K for $I = 20, 30, 40, 50$ and 60 mA, and $dH/dt = 0.50$ mT/s. The arrows show the direction of sweeping of the external magnetic field.

mA, respectively, so that below these H values the superconducting state is maintained. The $V - H$ curves measured with $dH/dt = 1.30$ mT/s show that the voltage drops and plateaus regions in the FDBs of the FR and RR develop for all current values considered (Fig. 4.28). A further increase in dH/dt (i.e, 2.60 mT/s) results in significant instabilities as in Fig. 4.29. Furthermore, the symmetry in the curves obtained for the FR and the RR is destroyed. However, there is no considerable change in the dissipation measured for all current values when dH/dt is increased from 0.50 to 2.60 mT/s.

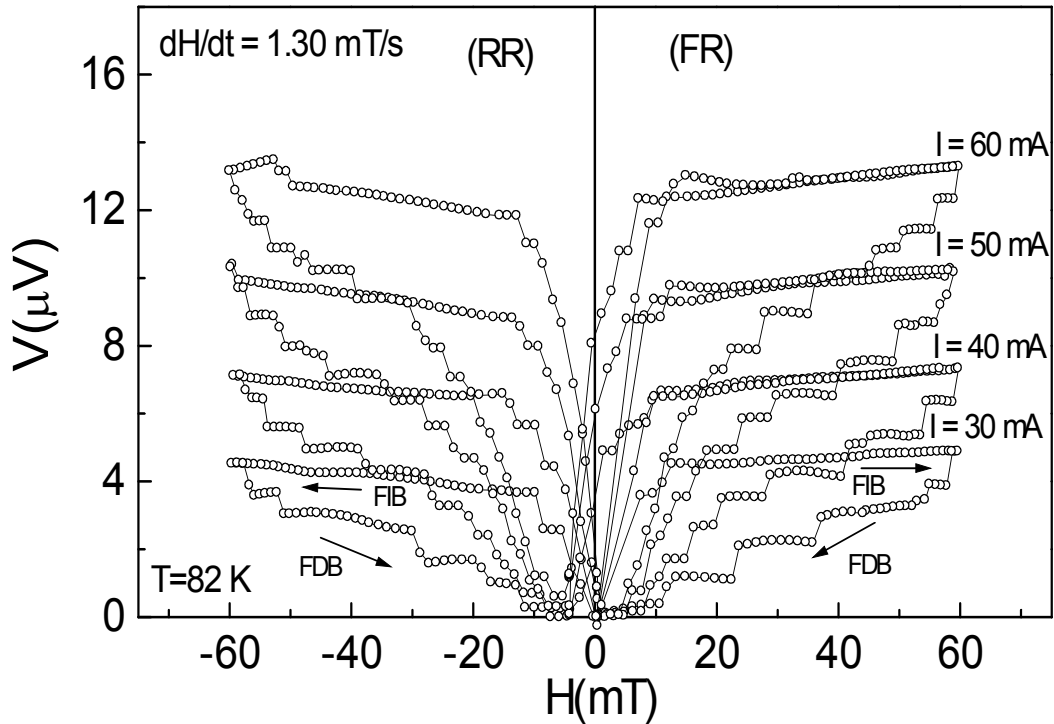


Figure 4.28 Magnetovoltage ($V - H$) curves of the YBCO/Ag sample measured at $T = 82$ K for $I = 30, 40, 50$ and 60 mA and $dH/dt = 1.30$ mT/s. The arrows show the direction of sweeping of the external magnetic field.

In detailed measurement of the $I - V$ curves, it was observed that there is a negligible difference between the measured voltage dissipation of the $I - V$

curves given in Fig. 4.2(c) and Fig. 4.6, so that they do not demonstrate any magnetoresistance effect as the external magnetic field is varied from 10 to 20 mT. The reason can be easily understood from the $V - H$ curves given in Figs. 4.27-4.29.

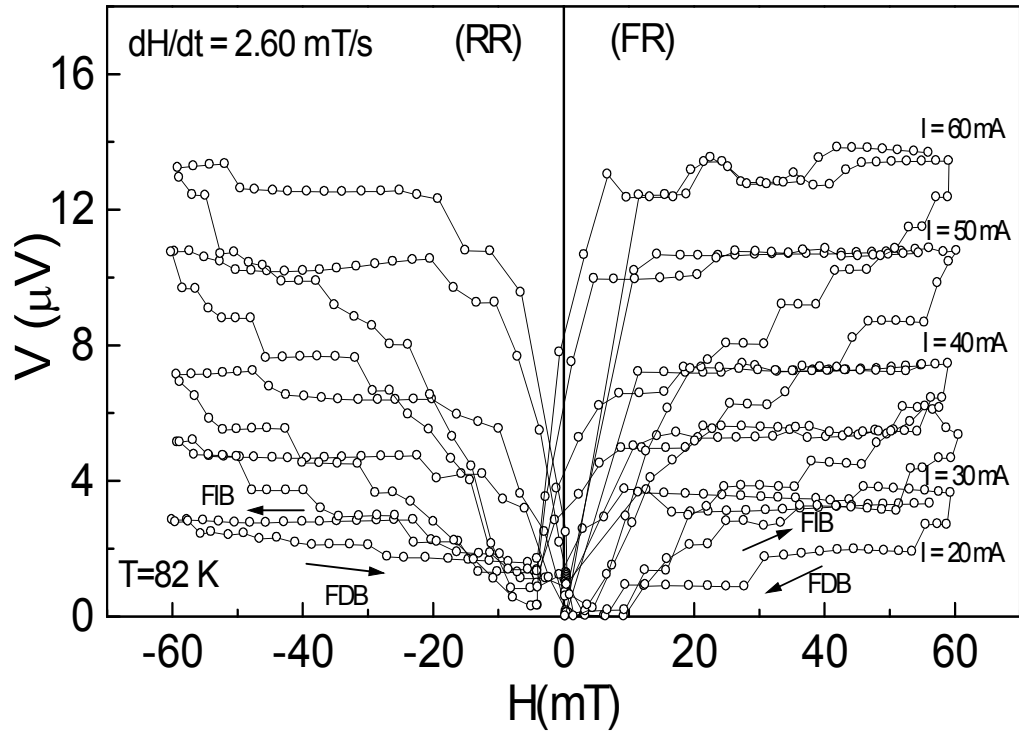


Figure 4.29 Magnetovoltage ($V - H$) curves of the YBCO/Ag sample measured at $T = 82$ K for $I = 20, 30, 40, 50$ and 60 mA and $dH/dt = 2.60$ mT/s. The arrows show the direction of sweeping of the external magnetic field.

Figure 4.30 shows a set of $V - H$ curves of undoped YBCO sample measured at $T = 82$ and $dH/dt = 1.00$ mT/s with $I = 30, 40, 50, 60, 70,$ and 75 mA [51]. The curves exhibit several different features as a function of the transport current. One of them is the strong irreversibilities appearing upon cycling the external magnetic field. The irreversible behavior of the $V - H$ curves for the undoped YBCO sample is more pronounced when compared to those observed in the Ag-doped

YBCO sample. In the case of increasing the magnetic field for both forward and reverse directions, the resistive state becomes observable after a certain critical value of the external magnetic field, H_c^{up} , and the dissipation sharply increases and tends to saturate; whereas, in the case of decreasing the magnetic field in both forward and reverse directions, the sample becomes less resistive, and it recovers the zero resistance state at another critical value of the external magnetic field (H_c^{down}) which is much greater than H_c^{up} .

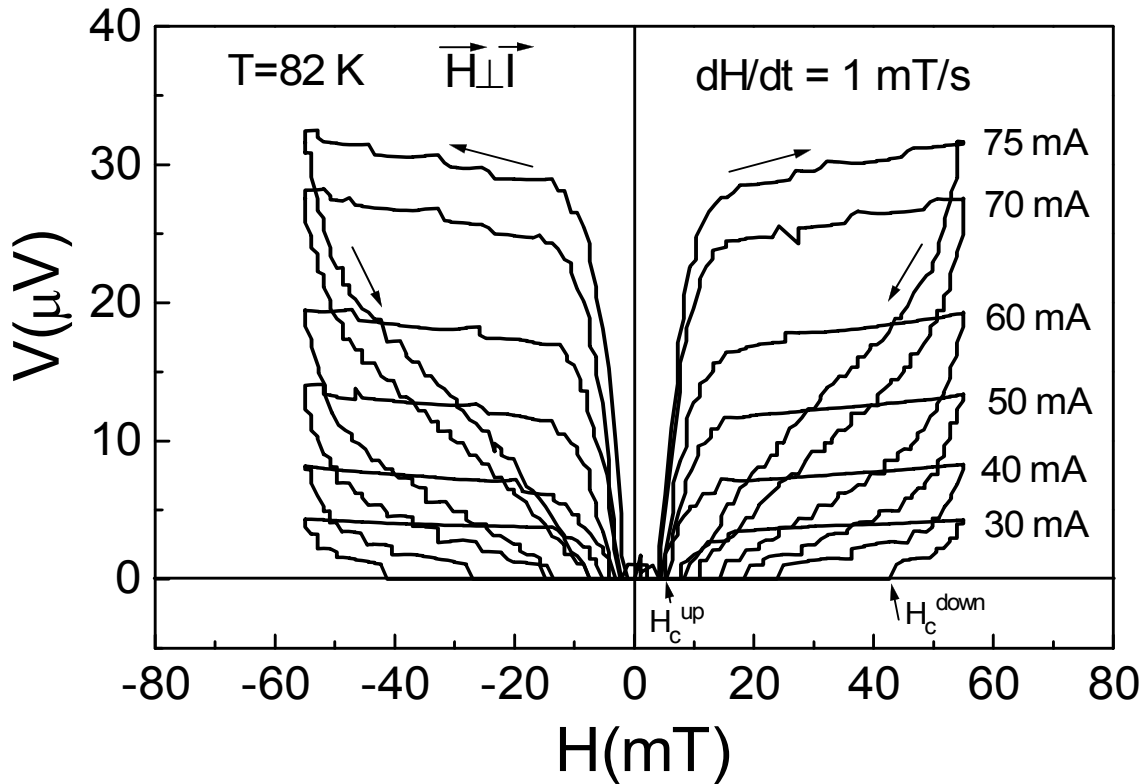


Figure 4.30 Magnetovoltage ($V - H$) curves of the undoped YBCO sample measured at $T = 82 \text{ K}$ for $I = 30, 40, 50, 60, 70$ and 75 mA and $dH/dt = 1.00 \text{ mT/s}$. The arrows show the direction of sweeping of the external magnetic field [51].

CHAPTER 5

DISCUSSION

In this chapter, the experimental results of $I - V$ curves, $V - t$ curves, voltage oscillations, and $V - H$ curves measured for the Ag-doped $Y_1Ba_2Cu_3O_{7-x}$ (YBCO/Ag) polycrystalline sample are discussed in terms of flux dynamics evolving mainly in the intergranular region and partly in the intragranular region of the sample. The interplay between the pinning and depinning process and the effect of doping Ag on the electrical transport properties and transport relaxation in YBCO/Ag ceramics are investigated in detail.

5.1 Current – Voltage ($I - V$) Characteristics Measurements

5.1.1 Flux dynamics and hysteresis effects

Electrical transport properties, particularly the current–voltage characteristics ($I - V$ curves), provide important information on the critical current density (J_c), practical applicability of the material, and the dissipation mechanisms of type-II superconducting materials. Therefore, measuring the $I - V$ curves has a great importance in characterizing the superconducting materials. To determine J_c , the $I - V$ measurements must be independent of how fast the data is collected [9, 11, 34-38]. In another words, the $I - V$ curves must be independent of the sweeping

rate of applied current dI/dt [11]. However, it is well known that the presence of giant flux creep in some high temperature (HTSCs) cuprates makes the $I - V$ curves and hence the corresponding J_c value time dependent [34]. One of the main reasons of the presence of giant flux creep is the high operating temperatures of HTSCs. In this case, the measured dissipation depends on the time scale and also the time constant of experimental set-up, and the time elapsed to plot the whole $I - V$ data [11, 34]. Therefore, in addition to the speed of measurement system, dI/dt must be considered as an important parameter in the $I - V$ measurements.

Zhang *et al.* [35] showed that numerical solutions of the non-linear diffusion equation in one dimension, which considers flux creep phenomena, gives apparent dI/dt dependent $I - V$ curves. Ding *et al.* [34] showed experimentally that the dI/dt controls the evolution of $I - V$ curves of Ag-Bi-2223 tapes and found that the critical current I_c decreases linearly with increasing dI/dt . Similar studies related to the numerical solution of non-linear diffusion equation were conducted by several authors [38-41]. It was reported that slow or fast ramping rates of the transport current affects the line shape of the $I - V$ curves, I_c , and flux profiles evolving along the sample [38-41]. Xiao *et al.* [9] investigated the flux dynamics of a strongly pinned vortex lattice in 2H-NbSe₂ and observed that both the $I - V$ curves and I_c become strongly dI/dt dependent for the magnetic field cooled sample of 2H-NbSe₂.

Due to the presence of different flux pinning mechanisms, hysteresis effects in the $I - V$ curves for both LTSCs [29, 133,134] and HTSCs [31, 135-138] were

observed upon cycling the transport current, as in the case of magnetization measurements ($M - H$ curves). We note that the physical mechanisms responsible for the hysteresis effects in the $I - V$ curves are different from those in the $M - H$ curves [11, 52].

Many experimental observations on both LTSCs and HTSCs reveal that the hysteresis loops in the $I - V$ curves can be clockwise (cw) [26, 29, 30] or counter-clockwise (ccw) [3, 7, 21, 23-25, 28, 31, 33, 43] in character, owing to the different pinning regimes inside the sample and the experimental conditions considered in the measurements. Several explanations have been proposed to explain the hysteresis effects in the $I - V$ curves. Self-Joule heating originating from the contacts where the transport current is applied [31], inelastic quasi particle scattering [139], dynamical metastability of the vortex matter in single crystalline samples [3,6,48], different pinning regimes associated with inhomogeneity of the sample (i.e., in polycrystalline samples) [24, 51] can cause ccw hysteresis effects in the $I - V$ curves of superconductors. The hysteresis effects were also explained in terms of position-dependent shielding currents in the frame of the critical state model [133] and also the change in the number of the mobile flux line dislocations [140]. In addition, the hysteresis effects in the $I - V$ curves have been explained by the presence of several dynamical phases of the vortices, which are related to the plastic flow, immobile or pinned vortex configuration etc. [134, 141, 142].

In order to identify the hysteresis effects in the $I - V$ curves obtained by using both the standard and reverse procedures, we first focus on the data presented in Figs. 4.2 – 4.10. As a first approximation, it can be suggested that the heating effects at current contacts can cause similar hysteresis effects seen in $I - V$ curves [24, 143]. Indeed, at high currents, the power dissipated at current contacts can be high enough to cause such effects. However, a careful examination of the data in Fig. 4.3, Fig. 4.7 and Fig. 4.8 reveals that the height of the hysteresis loops depends on dI/dt and decreases with decreasing dI/dt . Further, at low current sweep rates, much more time is spent to measure and plot the whole $I - V$ data. Therefore, the heat produced by the contacts should increase and cause an enhancement in the height of the hysteresis loop. On the contrary, we observed that the height of the loops decreases somewhat with reducing dI/dt . In addition, the power dissipated at the current leads (with the contact resistance $\sim 10^{-3} \Omega$) below the transition temperature is $\sim 9 \times 10^{-7} \text{ W}$ for currents in range up to 30 mA (see the $I - V$ curve in Fig. 4.2), and, this would cause no marked effect on the line-shape of the $I - V$ curves and would not be a source of instability seen in the $I - V$ curves.

Another possible mechanism which can cause hysteresis effects in the $I - V$ curves is the hot spot and local heating effects [24, 143, 144]. It can be suggested that, at the temperatures below T_c , the presence of Ag atoms along the grain boundaries can behave as resistive regions as compared to superconducting grains. At high driving current values, such resistive regions can be a source of local heating centers leading to an enhancement in the measured dissipation. It is

expected that the more heat is produced on the sample at the smaller values of dI/dt . As is mentioned above, the measured dissipation can increase at low current sweep rates since more time is spent to obtain the whole $I - V$ curve. In this case, both the hysteresis effects and voltage instabilities should increase. However, we generally observed that such effects, in particular, the voltage instabilities decrease with decreasing dI/dt and smooth $I - V$ curves are obtained. This implies that the doping with Ag has a positive contribution to the superconducting properties of YBCO ceramic by improving the grain connectivity. We, therefore, suggest that the hot spot and local heating effects can be easily ruled out and can not be a source of hysteresis effects observed in the $I - V$ curves in this study.

It is well-known that the low-field magnetization measurements ($M - H$ curves) are related to the intergrain currents which correspond to the flux trapping within the junction network. [51, 145, 146]. The pinning of the vortices in a junction network will depend on the amount of the disorder in the coupling strength between the grains. In addition to this, the applied magnetic field or the magnetic field induced by the transport current should be less than the first critical field of the grains $H_{c1,g}$. In fact, in a granular structure, it is extremely difficult to satisfy ideal and reversible junctions which are not consistent with low field $M - H$ data which show irreversibility effects [24, 51]. We suggest that doping of Ag destroys partly the intergranular pinning properties of the YBCO ceramic by increasing the grain coupling.

In both magnetic and transport measurements, at low dissipation levels, the flux lines enter into the intergranular region after overcoming the surface weak-links and demagnetizing factor of the sample. It is expected that the presence of metallic regions (or paths) formed by Ag atoms along grain boundaries act as easy motion channels for flux lines. Thus, the flux lines can move easily in those regions without encountering any obstruction until they meet the pinning centers or superconducting grains.

At this point, as a relevant parameter, the grain boundary resistivity (ρ_g) can help us to make a quantitative discussion of addition of Ag into the YBCO sample. First of all, we note that ρ_g is very sensitive to all kinds of defects and to the anisotropic effects associated the misoriented grains inside the sample [51]. As mentioned in the previous chapter, in most practical cases, it is reasonable to assume that ρ_g is proportional to the residual resistivity of the granular sample, which is obtained by extrapolating the $\rho - T$ curve from above T_c to $T = 0$ K. For further quantitative analysis, it is required to assume that the residual resistivity is largely dominated by the grain boundaries. The value of grain boundary resistivity ρ_g of our YBCO/Ag sample found from $\rho - T$ measurement is $\sim 10 \mu\Omega\text{-cm}$ (see Fig. 4.1). This implies that the grain connectivity between the grains increases by addition of Ag into the superconducting matrix of YBCO. It should be noted that the resistivity of Ag at $T = 300$ K is $\sim 1.6 \mu\Omega\text{-cm}$ which is much lower than that of ρ_g of YBCO/Ag. This difference can be attributed to the formation of S-N-S junctions in addition to the ones of S-I-S type which are expected naturally to be developed in a polycrystalline structure during the sample preparation. We also

note that the junctions of S-N-S and S-I-S type (or S-N-I-S) and also other kinds of defects should coexist in the granular structure of YBCO [51]. Therefore, under these conditions, ρ_g should be always greater than the resistivity of Ag. The addition of Ag into the YBCO matrix leads to a decrease the normal state resistivity ($\rho_n \sim 90 \mu\Omega\text{-cm}$) as compared to that of undoped YBCO ($\rho_n \sim 1500 \mu\Omega\text{-cm}$) [147].

The presence of S-N-S type junctions between the superconducting grains [99, 100] can bring the possibility of proximity effect on the evolution of hysteresis effects in the $I - V$ curves. Indeed, as is outlined in Chapter 2, the induced superconductivity can exist only in a thin surface layer (in order of the coherence length) of the normal metal near the S-N interface. However, the influence of the proximity effect on the measured transport properties of the YBCO/Ag sample must be negligible due to following reasons. First, the measurement temperatures considered in this study are very high and close to T_c of the sample. Second, the magnetic field values applied to the sample are much larger than the first (H_{c1}^w) and second (H_{c2}^w) critical fields of the weak-link structure, i.e., $H \gg (H_{c1}^w, H_{c2}^w)$. Therefore, it is possible that the grains are decoupled at these temperature and magnetic field values. Thus, the influence of proximity effect on transport measurements can be ruled out. In conclusion, it can be suggested that the hysteresis effects observed in the $I - V$ curves of the YBCO/Ag sample do not solely arise from the Josephson junction phenomena.

Now, we are in a position to discuss the hysteresis effects in the $I - V$ curves in more detail. We suggest that the hysteresis effects evolving in the $I - V$ curves of undoped HTSCs granular samples are related to the presence of weak-link structure. To verify this, we consider the $I - V$ curves of undoped polycrystalline YBCO sample [148] and also those of the newly found superconducting polycrystalline material MgB_2 [149]. It is well known that the presence of weak-links is a great problem in HTSCs cuprates and can cause a significant decrease in the current carrying capacity of the superconducting material. Therefore, many attempts have been made to improve the weak-links connecting the grains and also to produce weak-link free superconducting materials.

Figure 5.1 shows typical $I - V$ curves of polycrystalline YBCO and MgB_2 samples measured with $dI/dt = 1.25 \text{ mA/s}$ at zero magnetic field. Figure 5.1(a) reveals that the $I - V$ curve of undoped YBCO is quite smooth without any instability over the current range considered. It is also evident from Fig. 5.1(a) that a pronounced hysteresis develops in the $I - V$ curves of undoped YBCO sample upon cycling the transport current. It should be noted that the hysteresis effects in the $I - V$ curves of undoped YBCO are more pronounced than that of Ag-doped YBCO sample. It can be suggested that one of the main reasons responsible for this difference is the presence of weak-link structure in undoped YBCO sample, which has negative effects on both its transport and magnetic properties.

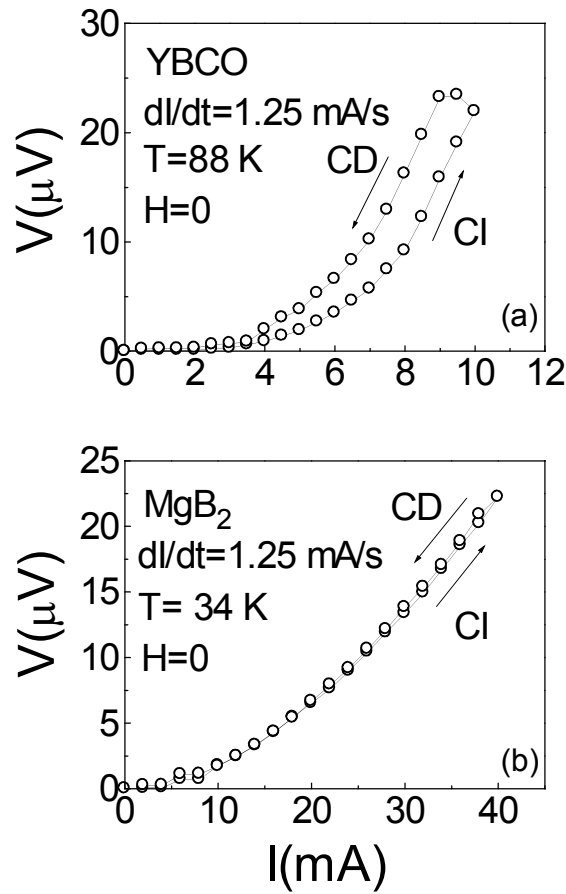


Figure 5.1 (a) Hysteresis effect observed in $I - V$ curve of polycrystalline sample of YBCO measured at $T = 88$ K and zero magnetic field for $dI/dt = 1.25$ mA/s (b) Hysteresis effect observed in $I - V$ curve of polycrystalline sample of MgB_2 measured at $T = 34$ K and zero magnetic field for $dI/dt = 1.25$ mA/s [148, 149].

Figure 5.1(b) demonstrates that there are no measurable hysteresis effects in the $I - V$ curves of polycrystalline sample of MgB_2 , so that the current increase and decrease branches of the $I - V$ curve collapse on the same curve and represent a reversible behavior upon cycling the transport current [149]. This implies that the current induced flux lines follow the same flow paths along the sample and see nearly same pinning potential. We also attribute this reversible behavior in the

$I - V$ curves of MgB_2 sample to the absence of weak-link structure. Indeed, many experimental observations reveal that the transport current (or associated vortices) in the MgB_2 sample are not limited by the weak-links between the grains [149, 150]. Therefore, the reversible $I - V$ curves of MgB_2 can be an indication of the absence of any weak-link problem, which can be ruled out in many magnetic and transport measurements. In view of discussion, we suggest that the physical origin of the negligible hysteresis effects observed in the $I - V$ curves of the YBCO/Ag sample can be related to the destruction of weak-link structure, and improvement of the grain connectivity achieved by doping of YBCO with Ag.

In some cases, the voltage difference between the CI and CD branches (or RCD and RCI branches in reverse procedure) becomes negligible. This implies that dI/dt should be reduced below the lowest value of 0.312 mA/s used this study, and slow current sweep rates should be preferred for practical applications of Ag-doped YBCO. Finally, upon cycling the transport current up and down, it can be suggested that the hysteresis effects in the $I - V$ curves of the YBCO/Ag sample arise from the different degrees of inhomogeneous flux motion between the CI and CD branches [24, 51].

5.1.2 Instabilities in the $I - V$ curves: Voltage jumps and drops

One of the main observations in the CI or RCI branches of the $I - V$ curves of the YBCO/Ag sample is the prominent voltage jumps and drops (see Figs 4.3 and 4.7). These instabilities tend to appear in all $I - V$ curves of YBCO/Ag and it

seems probable that they originate from doping of Ag into YBCO. We performed hundreds of $I - V$ measurements by using both the standard and reverse procedures at different temperatures, external magnetic fields, and dI/dt . We observed that most of the $I - V$ curves exhibit these instabilities, which strongly depend on external parameters such as dI/dt , I_{\max} , T and H considered in measurements. In particular, the magnitude of dI/dt controls mainly the evolution of these instabilities. When the ramping rate of transport current is high enough, the flux lines have less time to depin from one state to a more ordered one. Thus, the measured sample voltage does not change in a given range of transport current, although the Lorentz force acting on flux lines changes. Such a physical case would lead to the observation of several plateau regions in the $I - V$ curves, where the dissipation does not vary with increasing the transport current [11, 24]. At these plateau regions, the number of flux lines does not increase or decrease, and the flux line system is locked partly to a state for a while. After the evolution of plateau regions, the observation of small voltage jumps can be due to the continuous increase in the Lorentz force acting on flux lines. The voltage jumps can be correlated with sudden depinning of some of the flux lines and correspond to their ordered state (or correlated motion). On the other hand, at low current sweep rates, the flux lines can find enough time to make such transitions without showing instabilities. Hence, the instabilities in the measured voltage disappear and the both branches of the $I - V$ curves become smoother.

Furthermore, a negative differential resistance in the $I - V$ curves of the YBCO/Ag sample appears as the current is varied (see Figs 4.6 and 4.10). The

negative differential resistance can be explained as follows: First, the flux lines under the Lorentz force depin and flow defectively leading to an enhancement in measured dissipation. Second, a slight drop in measured dissipation is an indication of pinning of flux lines although the Lorentz force increases. That is, the competition between pinning and depinning results in favor of pinning. In a general description, such voltage jumps and drops in $I - V$ curves can be correlated to the increase or decrease in the number of the mobile flux lines, respectively, or attributed to the change in the average velocity of the flux lines.

It is also seen from the $I - V$ curves of the YBCO/Ag sample that increase in the applied magnetic field provokes the instabilities in the measured voltage. The increase in magnetic field can cause an increase in the nucleation centers for flux lines inside the sample. Since the penetration of the flux lines into the superconducting grains becomes difficult due to high shielding circulating currents around the periphery of the grain, they will try to distribute themselves spatially along the intergranular region where the Ag atoms exist. A partial penetration of flux lines into the grains via the weakest points of the grains can develop and some of them can be pinned there. Due to the increasing transport current with a given dI/dt , the Lorentz force stimulates the flux motion, and, therefore, can make the flux lines accumulated along intergranular region unstable. In such a physical case, the increase in the number of mobile flux lines per unit area can trigger easily the instabilities observed in the $I - V$ curves of YBCO/Ag.

It can be suggested that the instabilities in the $I - V$ curves of the YBCO/Ag originate from the phase slip centers due to the presence of Ag, or other impurities in the intergranular region. Elmuradov *et al.* [151] observed similar stepwise structure and ccw hysteresis effects in the $I - V$ curves of NbN wire with multi-contact configurations. The stepwise structure in those $I - V$ curves was attributed to the phase slip lines and was confirmed by numerical simulations using time-dependent Ginzburg-Landau theory [151]. The magnitude of the order parameter at the regions of phase slip centers can be reduced locally by imperfections and, even, can drop to zero. In this case, the current can be carried by normal electrons. The phase difference of the order parameter can vary at these regions from one place to another and manifest itself as a stepwise structure in the $I - V$ curves. However, at high current sweep rates, the Lorentz force acting on vortices becomes relatively greater than the one at low values of dI/dt , and, the distance traveled by the vortices becomes relatively greater than the correlation length, which is generally comparable to the size of the phase slip centers [151]. It is expected that the vortices moving at high current sweep rates will pass rapidly those centers without causing any stepwise structure in the $I - V$ curves. Therefore, we conclude that the stepwise structure can not originate from the phase slip center effects.

5.1.3 Reverse procedure in the $I - V$ curves

Measurements of the $I - V$ curves using the reverse procedure enable us to study the surface effects and the penetration of the transport current (or associated

vortices) from the outer surface of the YBCO/Ag sample [27, 28]. As soon as the current I_{\max} is applied to the sample, a measurable dissipation develops immediately, which is comparable to the one observed for the standard procedure with $I = I_{\max}$. Such a fast developing dissipation can be correlated with the presence of Ag atoms, which weakens the localized surface weak links. Thus, the flux lines find conductive silver paths (or channels) and penetrate easily into the superconducting material from its outer surface, and their final motion terminates in the superconducting grains. It can be suggested that the flux lines inside the sample are ready to move without encountering any obstruction along their travel.

To better understand the physical case described above, it is necessary to give a typical example for the $I - V$ curves of undoped polycrystalline YBCO sample measured by the reverse procedure. Figure 5.2 shows such an $I - V$ curve of undoped YBCO sample measured at $T = 85$ K and $H = 0$ for $dI/dt = 1.25$ mA/s. It is evident from Fig. 5.2 that no measurable voltage develops immediately as the transport current I_{\max} is applied to the sample. The dissipation starts from zero at $I = I_{\max}$ and increases almost linearly with decreasing the transport current. After the voltage passes through a broad maximum at about 45 mA, it decreases non-linearly with decreasing I and becomes zero at ~ 20 mA. For the RCI branch, after a certain threshold current value (~ 42 mA), a non-linear increase in the sample voltage is observed with increasing I , as in the case of the standard procedure. It should be noted that a significant hysteresis loop evolves in the $I - V$ curves of undoped YBCO sample measured by using reverse procedure.

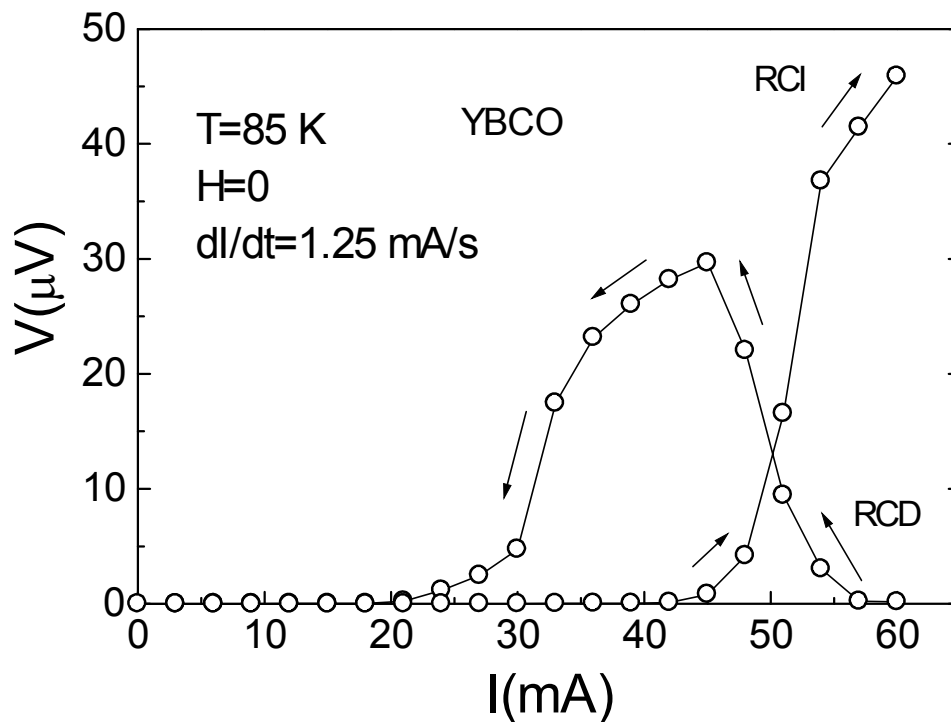


Figure 5.2 Hysteresis effect observed in the $I - V$ curve of polycrystalline sample of undoped YBCO measured at $T = 85$ K and $H = 0$ for $dI/dt = 1.25$ mA/s [148].

A physical description associated with the $I - V$ curve of undoped YBCO obtained by the reverse procedure is given in the following: As the transport current I_{\max} is applied to the sample, a large shielding current around the its periphery develops immediately and prevents the penetration of flux lines into the sample. That is why we do not observe any voltage dissipation at the beginning of the measurement. The increase in voltage dissipation is an indication of that the flux lines first overcome the demagnetizing factor of the sample and then the localized surface weak-link structure, which acts as surface pinning centers. Of course, in the Ag-doped YBCO sample, the physical case would be different: It appears that the presence of randomly distributed Ag atoms does not permit the formation of large shielding currents around the sample, but, reduces them to much smaller sizes. Thus, it makes the flux motion relatively easier from the sample surface to

the interior, and it results in an enhancement in the measured dissipation.

We now consider the $I - V$ curves of undoped YBCO sample measured by the reverse procedure in the presence of external magnetic field. Figure 5.3 shows typical hysteretic $I - V$ curves of undoped YBCO. It is evident from the $I - V$ curves of the undoped YBCO sample measured at $H = 10$ and 20 mT (Fig. 5.3(a)) that the dissipation on the RCD branch appears at $\sim 1 \mu\text{V}$ and $\sim 4 \mu\text{V}$,

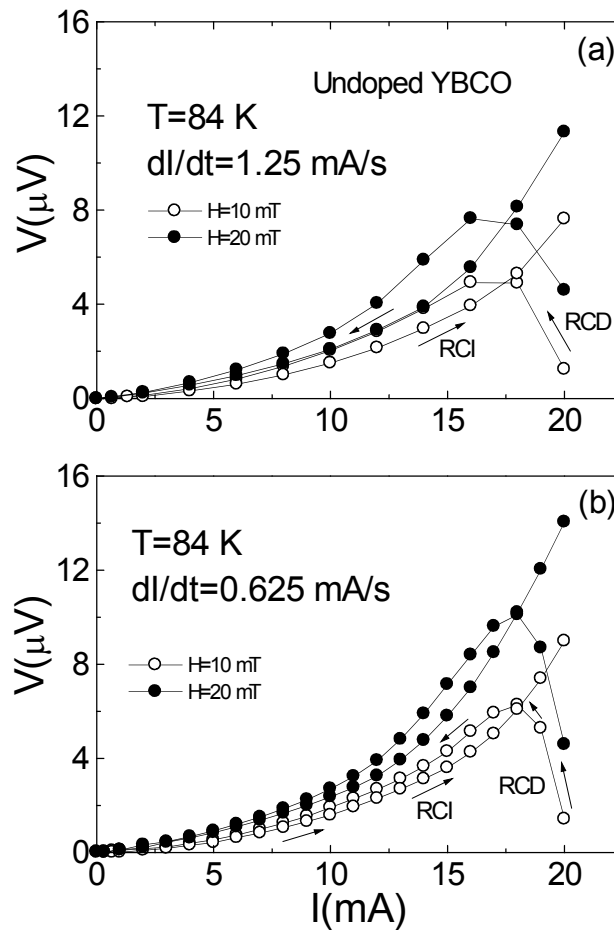


Figure 5.3 The $I - V$ curves of the undoped YBCO sample measured by the reverse procedure at $T = 84 \text{ K}$, and $H = 10$ and 20 mT for (a) $dI/dt = 1.25 \text{ mA/s}$ (b) $dI/dt = 0.625 \text{ mA/s}$. The arrows show the direction of sweeping of the applied current [28].

respectively, as soon as I_{\max} is applied. We observe that the sample voltage passes through a maximum value at ~ 17 mA for both magnetic field values as I_{\max} is decreased with $dI/dt = 1.25$ mA/s. The $I - V$ curves measured at $H = 20$ mT exhibit nearly the same behavior as in case of $H = 10$ mT, except an increase in measured dissipation. A similar physical case is also observed in the $I - V$ curves measured for $dI/dt = 0.625$ mA/s (Fig. 5.3(b)). The behavior of both the RCD and RCI branches in all $I - V$ curves are highly non-linear upon cycling driving current.

When the current I_{\max} is applied to the sample, the observation of a measurable dissipation in the $I - V$ curves implies that the surface and intergranular weak-links are disrupted by the external magnetic field, and hence the flux lines are ready to move. Therefore, due to the spatial distribution of the flux lines inside the sample, the Lorentz force can cause the motion of flux lines along the intergranular region, so that it results in an measurable dissipation at the beginning of measurement of $I - V$ curves. Note that the current values where the voltage reaches a maximum do not change with increasing the external magnetic field from 10 to 20 mT. This implies the presence of channel-like flow patterns in the undoped YBCO sample which widens as H is increased from 10 mT to 20 mT. In the $I - V$ curves for the YBCO/Ag sample given in Fig. 4.7, we observe that the sample voltage decreases non-linearly as I_{\max} is applied and does not exhibit any broad variation seen in RCD branches of the $I - V$ curve of undoped YBCO given in Fig. 5.3. This can be taken as an indication of the presence of foreign atoms inside the YBCO material. Indeed, the presence of Ag in the superconducting

structure of YBCO is responsible for this behavior observed in the $I - V$ curves of YBCO/Ag.

5.2 Transport Relaxation ($V - t$ curves) Measurements

It is well known that there are two different mechanisms which govern the transport phenomena in type-II superconductors: The interaction between flux lines, and the interplay between the flux lines and pinning centers [3, 5, 6, 12]. Short- and long-range correlations between the flux lines can cause several interesting phenomena, which can be investigated by slow and fast transport relaxation measurements [10, 43, 45, 152]. Thus, the flux dynamics and its details can be monitored by the time evolution of the voltage response to an applied current (i.e., the $V - t$ curves). During the relaxation measurements, the applied transport current can be interrupted or reduced to a finite value to create a quenched state along the sample [47, 153]. Thus, the details of re-organization process associated with transition from steady state response to disordered state can be investigated. Further, the type of driving current modulation also plays a crucial role in $V - t$ curve measurements, which help to explore new accessible states of the flux line configuration [2, 49, 50].

5.2.1 Evolution of the $V-t$ curves of the YBCO/Ag sample

5.2.1.1 Time effects for $I_1 > I_2$

Now, we discuss the $V-t$ curves presented in Figs. 4.11-4.17, which show that one of the main features of the $V-t$ curves is the rapid increase in voltage dissipation measured at beginning of the relaxation process. As a first approximation, as in the case of the discussion for the $I-V$ curves, we suggest that the Ag atoms destroy partly the natural structure of the junction network by reducing the intergranular flux pinning. Introduction of Ag into the structure could be responsible for the rapid initial increase in $V-t$ curves. Thus, the doping Ag into YBCO with can lead to metallic flow paths which form easy motion channels for flux lines and, therefore, the flux lines re-organize themselves very rapidly; so this process results in an increase in measured dissipation [28, 42]. Before the sample voltage levels off, the rapid increase in the voltage dissipation slows down in time and exhibits a shoulder in some $V-t$ measurements. We correlate this physical case to both the competition between pinning and depinning process and to the saturation in the number of new flow channels. In addition, the size of the resistive channels including the silver paths does not change during the time evolution of the sample voltage and this leads to developing of a constant flow rate for the flux lines along the sample. At high and moderate dissipation levels, it can be suggested that the presence randomly distributed Ag atoms inside the superconducting structure is one of the major important factors, which affects the line shape and the general behavior of the $V-t$ curves.

The strong competition between pinning and depinning manifests itself, in particular, at low dissipation levels. We suggest that the smooth $V - t$ curves measured at zero magnetic field (Fig. 4.14(a)) can be taken as a typical example for this strong competition. On the other hand, Fig. 4.15(b) shows that there is no smooth gradual increase in the sample voltage with time, although the measured dissipation is less than $1 \mu\text{V}$. The rapid increase in the voltage dissipation can be correlated to the presence of external magnetic field. As soon as the magnetic field is applied, the flux lines distribute themselves very rapidly along sample, since the surface and intergranular weak-links are already weakened by addition of Ag to YBCO ceramic. Therefore, initially, the flux lines are in a stationary state, and the flux lines are ready to move before the transport current is applied. Thus, in the presence of external magnetic field, at early times of the relaxation process, a rapid increase in the voltage can be expected even at low dissipation levels. A similar discussion for with the rapid increase in measured dissipation is also valid for the evolution of $V - t$ curves in Fig. 4.16 and Fig. 4.17.

The $V - t$ curves presented in Fig. 4.15(b) and Fig. 4.16 show that, following the rapid increase in the voltage, the voltage decreases slightly with time before leveling off. We suggest that the moving flux lines try to penetrate into the grains and some of them succeed to penetrate. We note that the penetrated flux lines can be found spatially within the London penetration depth of the grains in a pinned position. Since the mentioned decrease in the measured dissipation is very small, it is possible that the flux lines are mostly expelled from the grains. Furthermore, due to the strong competition between pinning and depinning, the size of the

ordered state decreases gradually with time, depending on the magnitude of I_1 . This results in a decrease in the number of the flux lines participating in the motion.

5.2.1.2 Time evolution of the quenched state created for $I_1 > I_2$

In the $V - t$ curves (Figs. 4.11-4.17), the initial current I_1 is suddenly reduced to a value I_2 less than I_1 . In some cases, we observed sharp drops in the time evolution of the sample voltage correlated to the glassy state relaxation, and in other cases the sample voltage varied smoothly with time. As can be seen from Figs. 4.11, 4.12, and 4.14(a), as I_1 is switched to zero, the sample voltage becomes abruptly zero, within the time response of the experimental set-up. This observation suggests that the local heating in the sample has negligible effect on the measured voltage [28, 42, 153]. Otherwise, a significant thermal relaxation which decays with time would be observed in the $V - t$ curves. In addition, the $V - t$ curve in Fig. 4.11 shows that, for $I_1 = 8$ mA, the measured voltage becomes approximately equal to zero. In this quenching process, the sample expels almost all the current-induced flux lines and behaves like a single macroscopic slab, since the magnetic screening is almost completed.

The bold solid lines in Figs. 4.11-4.14, 4.15(a) and 4.16 are the curves calculated from Eq. 2.13, which is an empirical relation of $V(t) = V(0) \exp(-t/t_0)^\alpha$ where t_0 is a characteristic time and the exponent α is a constant which depends on the external magnetic field (plus the self-field of the transport current) and

temperature. There is a reasonable agreement between the experimental $V - t$ curves and the empirical relation in Eq. 2.13. The characteristic time t_0 obtained by fitting Eq. 2.13 to the experimental data of Figs. 4.11, 4.12 and 4.13 is plotted as a function of I_2 in Figs. 5.4(a)-5.4(c), respectively. A value of ~ 1 is found for the exponent α which depends weakly on the current I_2 . Figure 5.4 demonstrates that t_0 tends to increase with increasing I_2 . We suggest that the magnitude of I_2 determines the general behavior of the created quenched state with time and t_0 controls the relaxation process. High values of I_2 require relatively higher values of t_0 , that is, in the relaxation of the quenched state, the redistribution of the transport current (or the associated vortices) along the sample evolves within very short time in different order of the penetrated states. Therefore, in the glassy state relaxation, we expect that the increase in I_2 can result in an increase in the value of t_0 .

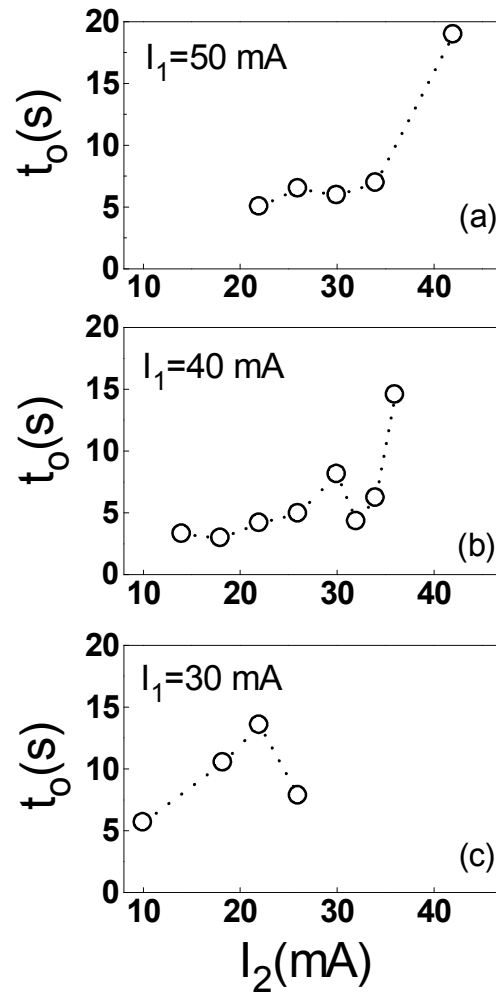


Figure 5.4 Variation of the characteristic time t_0 with current I_2 . The values of t_0 were extracted from the $V - t$ curves given in (a) Fig. 4.11, (b) Fig. 4.12 (c) Fig. 4.13. The dashed lines are a guide for the eyes.

In some $V - t$ curves (see Fig. 4.17) after a sharp drop in the sample voltage, the measured dissipation levels off in a very short time by reaching a steady state. We suggest that the flux lines redistribute themselves very rapidly in a distribution of energy landscape and find accessible stable states easily. Due to the number of the flux lines participating the motion, the presence of Ag atoms inside the superconducting structure can help the flux lines to explore the stable states. We

note that the quenched state can lead to the observation of switching effect in the $V - t$ curves under certain experimental conditions (see the $V - t$ curve measured with $I_2 = 12$ mA in Fig. 4.16).

Another interesting observation in the $V - t$ curves is the voltage hump observed at the onset of relaxation in the quenched state (see for instance the $V - t$ curves given in Figs. 4.11-4.13, 4.15(a) and 4.17). We correlate the voltage hump with a transient effect in the measured dissipation, which appears due to simultaneous operation of both pinning and depinning processes. It can be suggested that these two effects balance each other for a short while by causing a gradual change in measured voltage. Then, the transient effects disappear and a decay in the sample voltage appears with time. This is an indication of the fact that pinning dominates mostly the flux dynamics and is more effective with respect to depinning.

In the $V - t$ curves in Figs. 4.13, 4.14(a), 4.15(b) and 4.16, a smooth voltage decay is observed, instead of a sharp drop, as the initial current I_1 is dropped to I_2 . We note that the smooth voltage decays are generally observed when I_2 is comparable to I_1 , and at low dissipation levels below 1 μ V. In this case, the amount of flow channels decreases gradually in time, and the measured dissipation reflects slow dynamic competition between the pinning and depinning processes together with a gradual increase in the diamagnetic response of the sample. On the other hand, $V - t$ curves measured at the zero magnetic field (Fig. 4.14(a)) demonstrate that the smooth voltage decays result in a constant voltage level, which is practically independent of time for all values of I_2 considered. This implies that the amount

of flow channels does not change with time and thus the number of the current-induced flux lines remains constant.

In the following, to understand better the transport relaxation measurements of the YBCO/Ag sample, we present a typical example for the $V - t$ curves of undoped YBCO sample in Fig. 5.5 [28]. The initial stage of the relaxation process in the $V - t$ curve of undoped YBCO given in Fig. 5.5 is similar to that of Ag-doped YBCO (see Fig. 4.11). However, when the current I_1 (= 50 mA) is reduced to I_2 (= 34 mA), two-stage voltage decays appears in the relaxation process. First, the voltage decreases gradually for a while, and, then, at $t \sim 65$ s, it exhibits a smooth transition evolving to lower dissipation values as the time progresses. The solid line in Fig. 5.5 is the best fit Eq. 2.13 to the experimental data in the range $t > 65$ s. The parameters t_0 and α as found from the fitting procedure are ~ 11 s and ~ 1 , respectively. Our earlier $V - t$ measurements carried out on superconducting polycrystalline samples of YBCO [28] demonstrated that the evolution of $V - t$ curves is always highly non-linear as in Ag-doped YBCO investigated here. This suggests that the difference between the $V - t$ curves of Ag-doped and undoped YBCO samples depends on the structural composition, chemical, and anisotropic states. Of course, the main parameter which affects the time evolution of sample voltage is the doping level of Ag into YBCO.

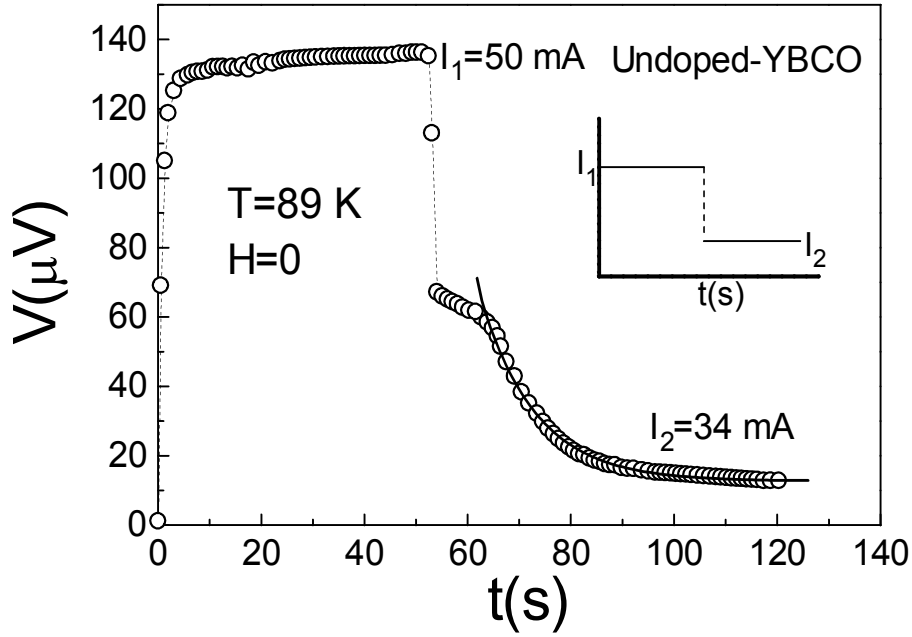


Figure 5.5 The $V - t$ curve for the undoped YBCO sample measured at $T = 89$ K and $H = 0$ for $I_1 = 50$ mA and $I_2 = 34$ mA. The inset shows schematic presentation of the applied current. The bold solid line is the curve calculated from Eq. 2.13. [28].

5.2.2 Current and magnetic field induced voltage oscillations

Experimental studies reveal that setting the flux lines in motion by different kinds of current modulations causes different motional re-organizations in type-II superconductors [1-4, 42, 48-50, 154]. Fast transport measurements using bi-directional square wave (BSW) currents showed clearly the current driven re-ordering of vortices [1]. D'anna *et al.* [1] suggested that the instabilities observed in detwinned single crystalline sample of YBCO arises from the entry surface barrier which influences the coherent motion of the vortices entering or leaving the large faces of the crystal. Kwok *et al.* [154] reported peculiar voltage oscillations in time to ac sinusoidal type driving current just below the melting (or

freezing) line of single crystalline sample of YBCO. They attributed the oscillatory instability in the YBCO sample to the strong competition between the driving and pinning forces together with relaxation effects and the long range spatial correlations in the vortex solid. Gordeev *et al.* [2, 49] and Rassau *et al.* [155] showed that the observation of regular voltage oscillations having low frequency depends strongly on temporal asymmetry of the drive and also its magnitude. The unusual instabilities were explained in terms of transitions between ordered and disordered states of vortex matter. In order to observe the periodic oscillations in response, the asymmetric current pulses are essential feature in producing such instabilities. In our case, one of the main conditions to observe the periodic voltage oscillations in the $V - t$ curves is to apply symmetric BSW current to the sample [28, 42, 50].

Due to the BSW current, the oscillatory driving force can cause a coherent motion of flux lines along weak pinning centers, and, after the forth and back repetitive oscillations, the flux line system becomes spatially more ordered in time. The regular voltage oscillations, without observation of any instability (i.e., voltage jumps or drops) or noise, evince for the formation of this ordered state. The voltage response associated with voltage oscillations lies typically in the range of 10^{-6} - 10^{-7} V [2, 50, 155]. This suggests that total number of the flux lines contributing to the oscillations is nearly constant and the change in the measured voltage can be related to the periodic variations in the average velocity of flux lines. The repetitive voltage oscillations seen in the $V - t$ curves of the YBCO/Ag sample (Fig. 4.18 and Fig. 4.19) are quite smooth and no voltage drop or jump are

observed for the positive or negative cycles of BSW drive. We suggest that the current-induced flux lines fluctuate between the ordered and disordered states by subjecting the same pinning forces in average.

The $V - t$ curves in Fig. 4.19 demonstrate that the amplitude of BSW current is one of the main parameters which affect the voltage oscillations. Regular sinusoidal oscillations disappear by increasing the amplitude of BSW current from 16 to 18 mA (i.e., 0.125 % increase). This implies that the Lorentz force dominates the pinning force, and depinning wins mostly this competition. As can be seen from Fig. 4.19(b), the sample voltage tends to increase or decrease in time for positive or negative cycles of BSW drive. We suggest that this observation can be related to the relaxation effects, short and long range correlations between the current-induced flux lines during the time interval corresponding to the half periods of BSW current [42, 155].

Another important parameter in the observation of voltage oscillations is the magnitude of applied magnetic field. It is seen from the $V - t$ curves in Fig. 4.20(b) and Fig. 4.20(c) that the external magnetic field causes a significant change in the line shape of voltage oscillations, and the oscillations undergo a significant change due to the increase in magnetic field. We address two different regimes in the $V - t$ curves in Fig. 4.20(b) and Fig. 4.20(c): The first one is regular sinusoidal voltage oscillations with low amplitude (i.e., $\sim 0.2 \mu\text{V}$) and the second one corresponds to the regime which resembles the variation of BSW drive with relatively large amplitude (i.e., $\sim 0.6 \mu\text{V}$). We suggest that, in the first regime, the

motion of flux lines makes regular transitions between ordered and disordered states, and that the second regime is related to the motional re-organization of flux lines due to the continuous dynamic annealing of the BSW current during the time evolution of sample voltage. Therefore, the corresponding states annealed by the BSW current can lead to increase in measured dissipation and fluctuations with time. The abrupt rise in the sample voltage after regular oscillations can be due to sudden increase in the fraction of the moving flux lines. Note that the first voltage jump (or drop) occur at ~ 38 s and ~ 43 s for $H = 16$ mT and $H = 20$ mT, respectively (see Figs. 4.20(b) and 4.20(c)). The difference can be attributed to the increase in the Lorentz force acting on flux lines, as the magnitude of external magnetic field is increased from 16 mT to 20 mT.

The $V - t$ curves in Figs. 4.18-4.20 demonstrate that the voltage oscillations are quite symmetric and follow the polarity change of the BSW drive. Since we used symmetric BSW currents, there should be an equality between flux exit and flux entry during regular oscillations of flux lines (or current induced flux lines).

Recently, Kalisky *et al.* [156] observed peculiar spatiotemporal oscillations in the vortex matter of single crystalline sample of $\text{Bi}_2\text{Sr}_2\text{CaCu}_2\text{O}_{8+x}$ (BSCCO) generated in the absence of external ac magnetic field. Oscillatory behavior in space and time of the magnetic induction has been explained in terms of flux wave phenomenon which appears near the order-disorder phase transition under suitable conditions. Barness *et al.* [157, 158] pointed out that the oscillatory temporal relaxation observed in single crystalline sample of BSCCO involves ordinary flux

creep and annealing transient vortex states. It is assumed that the magnetic diffusion equation governs the relaxation process evolving in the BSCCO sample.

The magnetic diffusion equation can be described by the Maxwell equations:

$$\partial B / \partial x = -\mu_0 J, \quad (5.1)$$

where J is the current density and μ_0 is the magnetic permeability of free space, and

$$\partial B / \partial t = -\partial E / \partial t, \quad (5.2)$$

where $E = R_F J \exp(-U/k_B T)$ is the electric field, $R_F = R_N(B/B_{c2})$ is the flux flow resistivity, and U is the pinning potential [156-158]. Assuming a logarithmic current density (J) dependence of U ,

$$U(J) = U_0 \ln\left(\frac{J_c}{J}\right), \quad (5.3)$$

one can get easily

$$\frac{\partial B}{\partial t} = \frac{1}{\mu_0} \frac{\partial}{\partial x} \left[D_f \frac{\partial B}{\partial x} \right] \quad (5.4)$$

for the relaxation process in one dimension [156-158]. Here $D_f = R_F (J/J_c)^n$ is the diffusion coefficient with $n = U_0/k_B T$. Barnes *et al.* [156] showed that, under

suitable conditions, the coupling between the annealing of disordered state and conventional flux creep could produce the oscillatory behavior of magnetic induction in time. Their experimental studies reveal that the oscillations appearing in magnetic induction can be related to periodic transformations in the vortex matter between ordered and disordered states.

A similar analysis can be done for the electric diffusion equation and the same Maxwell equations (Eq. 5.1 and Eq. 5.2) can be reduced to

$$\frac{\partial E}{\partial t} = f(E) \frac{\partial^2 E}{\partial x_2^2} \quad (5.5)$$

where $f(E) = \frac{1}{\mu_0} \left[\frac{\partial E}{\partial J} \right]$. In this case, we suggest that combination of electric diffusion equation with conventional flux creep theory and the logarithmic current dependence of pinning potential can give similar time dependent oscillatory behavior of electric field (or voltage) for the time intervals corresponding to the positive and negative cycles of the BSW current with long P_1 values, i.e., $0 \leq t < P_1/2$, and $P_1/2 \leq t < P_1$, respectively.

The voltage oscillations in the YBCO/Ag sample can be described by an empirical expression

$$V(t) = A + B \sin(\omega t + \phi), \quad (5.6)$$

where A and B are the constants, ω is the frequency and ϕ is the phase angle. The bold solid lines in Figs. 4.18-4.20 are the best fits of Eq. 5.6 to the experimental

data. We note that the fitting procedure was performed for each period of repetitive voltage oscillations separately. As is seen from the $V-t$ curves given in corresponding figures, there is a reasonable agreement between the experimental data and calculated curves. Further, the curve fitting shows that the phase angle ϕ generally takes different values for the observed repetitive oscillations. Table 5.1 shows the values of phase angle ϕ found from the experimental $V-t$ data given in Fig. 4.18. The phase angle ϕ takes negative values for all period values of BSW current and tends to decrease from first period to the final one.

Table 5.1 The phase angles ϕ obtained by fitting Eq. 5.6 to the $V-t$ data in Fig. 4.18.

$T = 89 \text{ K}, H = 0 \text{ mT}, I = 15 \text{ mA}$			
	BSW $P_1 = 10 \text{ s}$	BSW $P_1 = 14 \text{ s}$	BSW $P_1 = 20 \text{ s}$
Period of response (P)	Phase Angle (ϕ)	Phase Angle (ϕ)	Phase Angle (ϕ)
P ₁	-1.40 $\pi/2$	-0.72 $\pi/2$	-0.52 $\pi/2$
P ₂	-1.20 $\pi/2$	-0.76 $\pi/2$	-0.60 $\pi/2$
P ₃	-1.40 $\pi/2$	-0.76 $\pi/2$	-0.62 $\pi/2$
P ₄	-1.66 $\pi/2$	-0.86 $\pi/2$	-0.64 $\pi/2$
P ₅	-1.84 $\pi/2$	-0.94 $\pi/2$	-0.68 $\pi/2$
P ₆	-2.08 $\pi/2$	-0.98 $\pi/2$	-0.64 $\pi/2$
P ₇	-2.28 $\pi/2$	- $\pi/2$	-0.70 $\pi/2$
P ₈	-2.50 $\pi/2$		
P ₉	-2.72 $\pi/2$		

The phase angles ϕ found from the best fits of Eq. 5.6 to the experimental data in Fig. 4.19 exhibit similar behavior. Table 5.2 shows the variation of ϕ with each

period of response. The $V - t$ curves in Figs. 4.18 and 4.19 are measured at zero field. We suggest that the current-induced flux line system is prepared within a certain time interval (i.e., P_1) of a corresponding cycle. For each cycle, the initial conditions in preparing the flux line system are determined by the former one and so on. Therefore, it is natural to expect such a phase difference between successive voltage oscillations.

Table 5.2 The phase angles ϕ obtained by fitting Eq. 5.6 to the $V - t$ data in Fig. 4.19.

$T = 89 \text{ K}, H = 0 \text{ mT}, I = 16 \text{ mA}$	
BSW $P_1 = 20 \text{ s}$	
Period of response (P)	Phase Angle (ϕ)
P_1	$- 0.54 \pi/2$
P_2	$- 0.58 \pi/2$
P_3	$- 0.60 \pi/2$
P_4	$- 0.64 \pi/2$
P_5	$- 0.68 \pi/2$

However, the best fits of Eq. 5.6 to the experimental $V - t$ data in Fig. 4.20 are obtained when the phase angle ϕ takes approximately constant values for each period of response (Table 5.3). This implies that the phase angle ϕ does not change much in time along the whole relaxation process. It is seen from the Table 5.3 that the value of the phase angle ϕ is essentially independent of the applied magnetic field. The physical descriptions is as follows: The order parameter in the

intergranular region of the YBCO/Ag sample is easily suppressed by the external magnetic field and some of the flux lines penetrate into the grains along the easy motion channels and some of them are pinned inside the grains. We note that, in the presence of external magnetic field and at this temperature ($T = 89$ K), the grains are not fully superconducting islands. Therefore, the motion of flux lines can give a regular and ordered response to the change in the polarity of BSW current, and, thus, the initial and final conditions in preparing the flux line system corresponding to each cycle can remain nearly constant in time.

Table 5.3 The phase angles ϕ obtained by fitting Eq. 5.6 to the $V - t$ data in Fig. 4.20.

$T = 89$ K, BSW $P_1 = 10$ s, $I = 4$ mA			
	$H = 10$ mT	$H = 16$ mT	$H = 20$ mT
Period of response (P)	Phase Angle (ϕ)	Phase Angle (ϕ)	Phase Angle (ϕ)
P ₁	- 0.42 $\pi/2$	- 0.40 $\pi/2$	- 0.38 $\pi/2$
P ₂	- 0.44 $\pi/2$	- 0.40 $\pi/2$	- 0.40 $\pi/2$
P ₃	- 0.42 $\pi/2$	- 0.42 $\pi/2$	
P ₄	- 0.40 $\pi/2$		
P ₅	- 0.38 $\pi/2$		
P ₆	- 0.36 $\pi/2$		
P ₇	- 0.36 $\pi/2$		
P ₈	- 0.36 $\pi/2$		
P ₉	- 0.36 $\pi/2$		

5.2.3 Relationship between voltage oscillations and charge density waves

The oscillations of voltage response generally follow the period of the BSW driving current. Typical examples for the FFT of $V - t$ curves in Figs. 4.18(a)-4.18(c) are shown in Figs. 5.6(a)-5.6(c). The fundamental periods ($P_{V_{osc},FFT}$) obtained from FFTs are 9.89 s, 14.10 s and 19.72 s, which are in good agreement

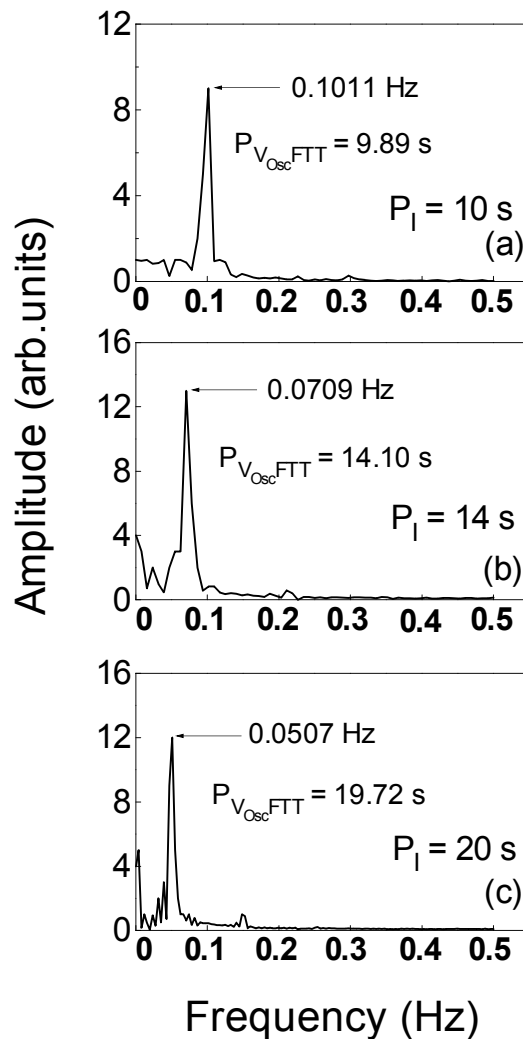


Figure 5.6 Fast Fourier Transform (FFT) of the $V - t$ curves given in Fig. 4.18(a) – 4.18(c). The fundamental frequency is marked on each curve. The fundamental period $P_{V_{osc}, FFT}$ found from FFTs is given for each curve with the period of applied BSW currents.

with the periods of the BSW drive, i.e., $P_1 = 10, 14$ and 20 s, respectively. These findings suggest the presence of a dynamic physical case, which resembles the sliding charge-density waves (CDWs) by an external drive [2, 49, 153, 155]. The regular voltage oscillations may be described as the transit of periodic vortex density fluctuations [2, 49, 153, 155]. It has been suggested that the system of weakly pinned vortices resembles the pinned CDW state [2, 49, 153, 155]. Experimental studies on CDW revealed that, in a current or voltage controlled experiment, coherent current or coherent voltage oscillations appear across the sample after a threshold value of the driving current or voltage [159-166]. In the present study, we suggest that a physical mechanism concerning the density fluctuations of flux lines (or self magnetic field (SMF) lines) can be introduced as a possible mechanism for coherent voltage oscillations. Such coherent density fluctuations of flux lines (or SMF lines) can develop along the YBCO/Ag sample and can result in similar effects as in the case of the CDW's.

5.3 Magnetovoltage Measurements

Systematic experimental studies have been made to understand the physical mechanisms responsible for the hysteresis effects in the magnetoresistance of superconducting materials [51, 55-57, 103, 167-173]. The hysteretic effects in magnetoresistance measurements appear mostly in the clockwise direction as the external magnetic field is swept up and down [51 – 57, 167-173]. Generally, the low and high field strong irreversibilities observed in polycrystalline HTSC samples are interpreted in terms of flux trapping developing in both intergranular

and intragranular regions [51 – 57, 167-173]. Ji *et al.* [53] proposed an analytical model, so called two-level critical state model, by calculating the macroscopic and local fields for ordered and disordered polycrystalline HTSC samples. In this model, it was assumed that the flux dynamics is maintained by percolative paths through the grains. The model explains the microwave losses in granular materials and also describes the magnetic hysteresis effects. Furthermore, a model for high field magnetoresistance of granular samples was developed by Beloborodov *et al.* [174], which gives a reasonable agreement with the experimental results concerning the negative magnetoresistance observed in granular superconducting Al sample [175]. Recently, Palau *et al.* [176] showed that the irreversibility effects arise from the return field from grains into the grain boundaries. Balaev *et al.* [177] reported that the broadening of the resistive transition of polycrystalline composite samples of YBCO+CuO and its magnetoresistance measured at very low magnetic fields could be explained well by the Ambegoakar-Halperin model [178]. Zuo *et al.* [179] considered a similar model to explain the resistive transition and magnetoresistance effect observed in an organic superconductor (κ -(BEDT-TTF)₂Cu[N(CN)₂]Br).

We note that the transport critical current density J_c of polycrystalline high T_c superconductors has been found strongly hysteretic at low applied magnetic fields [135, 136, 179]. The intragranular flux-trapping model was developed to calculate $J_c(H)$ and fit the experimental $J_c - H$ data in both YBCO and BSCCO ceramic superconductors [101, 181, 182]. However, these models have disregarded the magnetization of the intragranular medium. In those studies, it was assumed that

the superconducting grains are embedded in non-superconducting host, without any intergranular shielding effects. Mahel and Pivarc [54] used the two level magnetic system model [53] to explain the hysteresis effects in magneto-resistance measurements of HTSCs under low magnetic fields in transport and magnetic measurements at different temperatures. Chen and Qian [183] reported irreversible behavior of the critical current density $J_c(H)$ and magnetovoltage $V(H)$ of $\text{YBa}_2\text{Cu}_3\text{O}_{7-x}$ at low magnetic fields ($H < 50$ mT). The hysteresis effects in those measurements were attributed to trapped flux in the loop comprised between superconducting grains and weak links. On the other hand, the peculiar high field hysteresis effects observed in granular type-II superconductors were explained mainly in terms of flux trapping evolving inside the grains [51, 53-57, 101, 102, 183-185].

In this study, the experimental $V - H$ data of YBCO/Ag were mainly interpreted and analyzed by considering the two-level magnetic system. The general behavior of $V - H$ curves was also examined by considering the method proposed by Balaev *et al.* [54-57]. By using this model, it is possible to distinguish the contribution from both intergranular region or intragranular region to the measured dissipation in $V - H$ curves.

5.3.1 Hysteresis effects in $V - H$ curves and intra- and inter-granular flux trapping

In our measurements, the $V - H$ curves demonstrate two distinct regimes for the field increase branch (FIB) in forward region. First, rapid increase in the measured voltage at low magnetic fields; second, at moderate field values, a saturation in the measured voltage (see Figs. 4.21– 4.29). Upon cycling the external magnetic field, all $V - H$ curves exhibit clockwise hysteresis effects which can be correlated to the two-level magnetic system.

To a first approximation, the initial rapid increase in $V - H$ curves corresponds to the destruction of the highly ramified weak-link structure between the superconducting grains. The external magnetic field with the critical fields of weak-link structure controls predominantly the coupling states between the grains [51, 52, 53-57].

It is well known that polycrystalline bulk HTSC samples show typical weak-link behavior which can be easily destroyed even at small external magnetic fields. A weak-link structure is generally assumed to behave like a type-II superconductor with its own penetration depth, H_{c1}^W , H_{c2}^W and edge (surface like) screening current flowing along the edge of the junction [52]. It should be noted that irreversibilities are related to the flux trapping in the junction network. The critical magnetic fields H_{c1}^W and H_{c2}^W can be obtained from low-field

magnetization measurements ($M - H$) [51, 52]. H_{c1}^W represents the characteristic magnetic field at which the first flux penetrates the sample through the weak links. For $H > H_{c2}^W$, the weak link structure is completely destroyed by the external magnetic field. As H is increased above H_{c2}^W , the flux lines would penetrate the superconducting grains. For $0 < H \leq H_{c2}^W$, it is quite normal to expect that the flux lines evolve in the form of Josephson type, whereas, for $H > H_{c2}^W$, the flux lines penetrated into the grains will evolve gradually from Josephson to Abrikosov-type with a reduced size [52, 55].

In the $V - H$ curves, the expected resistive response of a granular sample depends on the magnitude of transport current and also the external magnetic field. At low enough applied currents less than the critical current I_c , zero resistance state is satisfied along the sample if $H < H_{c1}^W$ and no dissipation is observed in the $V - H$ curves. In this case, it can be assumed that the sample behaves like a quasi-single superconducting slab and the shielding current circulates around periphery of the sample within the penetration depth λ_L . As H is increased with a certain sweep rate dH/dt , the flux lines driven by the Lorentz force associated with the transport current will penetrate the sample gradually from its surface into grain boundaries and sample pores, so that it results in an increase in the measured dissipation. At low magnetic field values, the flux motion is inhibited by the screening currents flowing between the grains surrounding by the intergranular region of the sample. When the first weak-link is broken by the flux lines in Josephson character, the critical current density increases in the neighboring area of the sample and disrupts the other weak-links as a cooperative phenomenon which we do not

observe in our magnetic measurements. Thus, the density of flux lines per unit area will increase over the weak link structure and flux motion will end in highly superconducting grains which resist strongly against the flux penetration [52]. In this process, the measured dissipation increases rapidly until the external magnetic field reaches the Josephson de-coupling field H_{c2}^W of the weak-link network. If the external magnetic field is less than the first critical field of grains ($H_{c1,g}$), since $H_{c1,g} \gg H_{c2}^W$, further increase in the applied magnetic field will not produce any extra dissipation because most of the grains are disconnected from each other and the intergranular region of the sample is in normal state for of $H \geq H_{c2}^W$. It can be assumed that, at relatively low magnetic fields, the normal state resistance of a type-II superconductor is independent of the applied magnetic field [169]. This implies that the resistance of the intergranular region will not change until the external magnetic field exceeds $H_{c1,g}$. We note that low-field $M - H$ measurements reveal that H_{c1}^W and H_{c2}^W have values in the order of a few 0.1 mT and ~ 1 mT, respectively, at liquid helium temperatures [51, 52]. These junction parameters are temperature dependent and increase with decreasing temperature.

The number of the flux lines is controlled by the sweep rate of external magnetic field dH/dt which is an important parameter for the evolution of $V - H$ curves [51]. The lowest dH/dt value used in our measurements is 0.50 mT/s and the range of external magnetic field is between 0 – 60 mT. Therefore, the penetration rate of flux lines from the sample surface to its interior will be extremely large and the weak-link network will be destroyed within a very short time, i.e., $t < 2$ s. If the grains become de-coupled, a measurable voltage dissipation is observed.

The $V - H$ curves of undoped YBCO (see Fig. 4.30) reveal that the superconducting state is not destroyed up to a critical field H_c^{up} when H is increased (for the FIB). For the FDB, the sample recovers the superconducting state at a critical magnetic field value H_c^{down} when H is decreased. The zero voltage dissipation (for the FDB branch) is a measure of re-formation of the coupling between the superconducting grains. The values of H_c^{up} and H_c^{down} depend on the magnitude of transport current. For instance, for $I = 30$ mA, H_c^{down} is ~ 42 mT in the $V - H$ curve in Fig. 4.30 for undoped YBCO, whereas, H_c^{down} of $V - H$ curve in Fig. 4.28 for the YBCO/Ag sample is ~ 10 mT. This suggests that the flux pinning properties in the intergranular region of YBCO are weakened by adding Ag into the superconducting structure, and enhances the formation of isolated superconducting grains in sample.

It can be deduced from the detailed discussion (see section 5.1) on the $I - V$ curves measured by using both the standard and reverse procedures that the other parameter which affects the evolution of the $V - H$ curves is the addition of Ag into the structure. The experimental $I - V$ curves demonstrate that the weak-link structures in the intergranular region and also on the surface of the YBCO sample are weakened by introducing Ag. It is seen from the comparison of the $V - H$ curves for YBCO/Ag (Fig. 4.28) and undoped YBCO (Fig. 4.30) that the presence of Ag in the superconducting structure causes a marked decrease in hysteresis effects. In addition, although the instabilities in the $V - H$ curves of undoped YBCO are quite small, the voltage drops and plateau regions in both of decreasing branches (FDB and RDB) become more significant for the YBCO/Ag sample.

The long-lived plateau regions in the decreasing branches of the $V - H$ curves of YBCO/Ag imply that the number of flux lines joining the motion does not change and the dynamic process locks to a state for a long time, although the Lorentz forces increases. However, an opposite case is observed in the $V - H$ curves of undoped YBCO sample. This means that number of the pinning centers in the junction network of undoped YBCO is greater than that of YBCO/Ag. In the case of undoped YBCO sample, the flux lines do not lock to a state for a long time and move locally from one pinning regime to another. Thus, the dynamic process associated with the motion of flux lines in undoped YBCO is forced to change its state gradually within a short time.

It is seen from the $V - H$ curves that the long-lived plateau regions in the decreasing branches of YBCO/Ag become more significant as dH/dt is increased from 0.50 to 2.60 mT/s. This implies that the number of the mobile flux lines does not change for a while and a constant flow rate of flux lines evolves although the external magnetic field is continuously varied. In this process, the drop in the sample voltage is a measure of the drop in the number of flux lines, and, also, of flux pinning. We suggest that high dH/dt values make locally the correlated flux motion unstable. However, at low values of dH/dt , the flux lines find enough time to change their states gradually and, therefore, sharp drops or jumps are not observed in the $V - H$ curves. At this point, it should be emphasized that the same physical mechanisms responsible for the step wise structure of the $I - V$ curves also control the evolution of the $V - H$ curves.

The strong irreversibilities in observed low-field magnetization measurements can be taken as an indication of flux trapping in the junction network. In granular samples of HTSCs, it is generally argued that the superposition of external magnetic field and local magnetic fields (induced by a magnetic dipole moment of neighbor superconducting grains in the inter-grain boundaries) determine the specific character of magnetovoltage measurements [51, 53-57]. For the FIB in the forward region (FR), when the external magnetic field is increased with a given dH/dt , the superconducting grains will show a negative diamagnetic response to the variation of H . Within the description of two-level magnetic system, the effective field B_i averaged over the local fields in the intergranular region will be greater than the value H [53-57]. On the other hand, for the FDB, when H is decreased, the diamagnetic response of superconducting grains will be positive and the effective field B_i will be less than the value H . Therefore, the dissipation measured for the FIB and FDB will give the result of $V(H^+) > V(H^-)$ which is the origin of the hysteresis effects observed in $V - H$ curves [53-57]. Thus, we can correlate nearly absence of irreversible behavior in the $V - H$ curves at relatively high fields (see Fig. 4.21-4.23) to the equality of effective fields (B_i) evolving in the intergranular region for the FIB and FDB. At this point, we note that the same discussion on the irreversible behavior of $V - H$ curves is essentially valid for when the polarity of external magnetic field is reversed.

We now return to our $V - H$ data and analyze the hysteresis effects in more detail within the two-level magnetic system proposed by Balaev *et al.* [55]. Figure 5.7 shows the current and magnetic field sweep rate dependences of the hysteresis

width (ΔH) as a function of H^- . These $\Delta H - H^-$ curves were extracted from the $V - H$ data in Figs. 4.21-4.23. Every extracted data point in the $\Delta H - H^-$ curves corresponds to a constant value of measured voltage in the forward region of the $V - H$ curves (see Fig. 2.10). It is seen from Fig. 5.7(a) that all curves collapse nearly on a single curve at low field values of H^- . The departure from the single curve starts at $H^- = 6.5, 15$ and 22 mT for $dH/dt = 0.50, 1.30$ and 2.60 mT/s, respectively. We note that, for all sweep rates above these values of H^- , ΔH depends on the magnitude of transport current.

According to Eq. 2.19, the current dependence of ΔH can be taken as an indication of the contribution of the magnetization of intergranular region (M_i) to ΔH . However, it is seen from Fig. 5.7 that the temperature ($T = 88\text{K}$) at which the measurements were done is close to T_c . At $T \lesssim T_c$, the Josephson coupling energy between the grains should decrease and, thus, the flux trapping capability of the junction network should decrease accordingly. In addition, the presence of Ag atoms in the structure causes the formation of normal regions at the grain boundaries or S-N-S junctions and can reduce enormously the Josephson coupling energy between grains. Further, as mentioned above (and in Chapter 2), at a given temperature, low driving currents and low magnetic field values, which are comparable to the junction parameters, are required to observe the current dependence of ΔH .

It appears that current dependent ΔH presented in Fig. 5.7 is a contradiction to the intra- and inter-granular flux trapping model proposed by Balaev *et al.* [55]. We

suggest that, at $T \lesssim T_c$ where the superconducting fluctuations are high, the hysteretic behavior of the $V-H$ curves should be controlled mainly by the flux

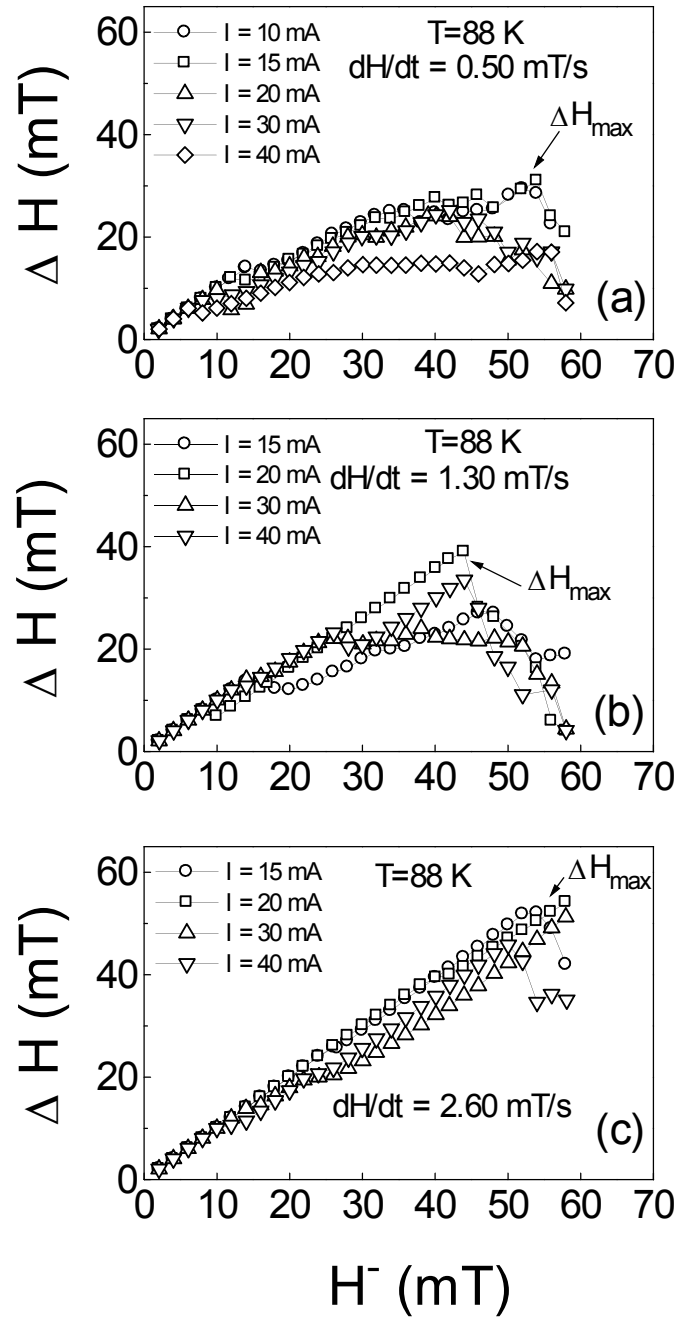
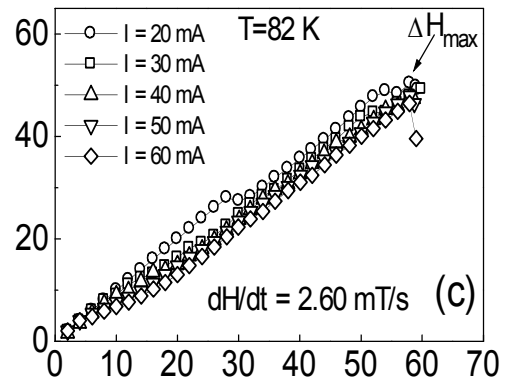
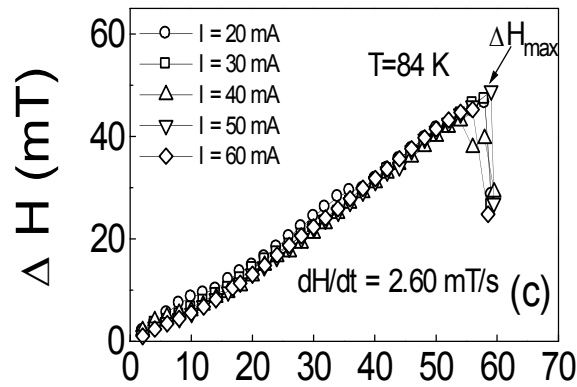
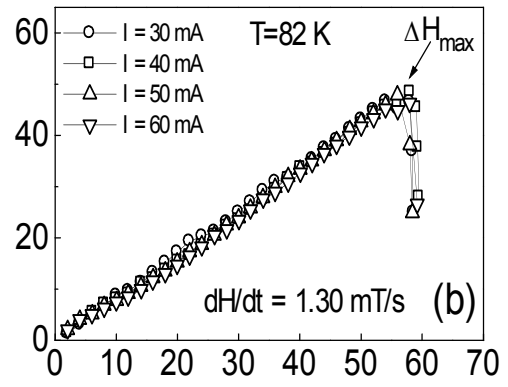
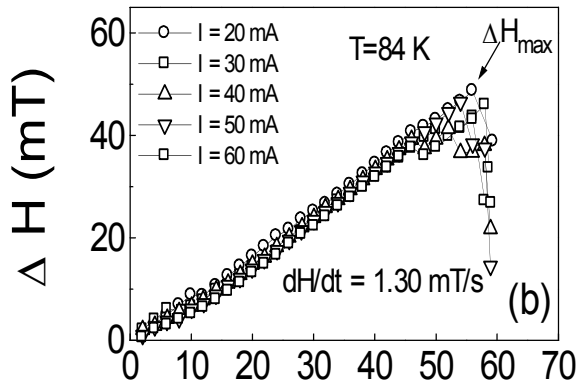
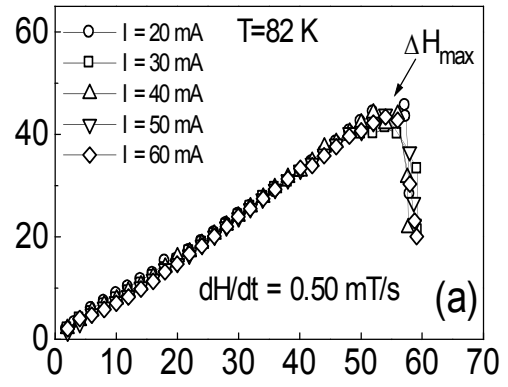
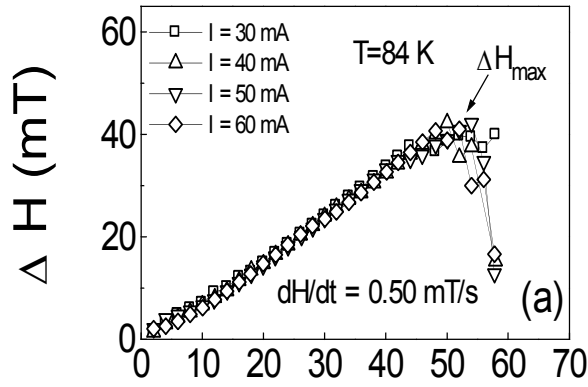


Figure 5.7 $\Delta H = f(H^-)$ curves of the YBCO/Ag sample determined at $T = 88$ K for different current values and magnetic field sweep rates of **a)** $dH/dt = 0.50$ mT/s **b)** $dH/dt = 1.30$ mT/s **c)** $dH/dt = 2.60$ mT/s. The data were extracted from the $V-H$ curves in Figs. 4.21-4.23.

pinning in grains which are not fully superconducting regions. In this description, the transport current can affect the flux lines pinned inside the grains and reinforce the flux motion through them. Therefore, a current dependence of ΔH should be expected.

Another parameter which makes ΔH current dependent is the sweep rate of external magnetic field (dH/dt). At low values of dH/dt , some of the flux lines find enough time to penetrate into the grains with the help of Lorentz force and keep their motion through the weak pinning channels by following reversible paths upon cycling the external magnetic field. However, as dH/dt is increased from 0.50 to 2.60 mT/s, the ΔH becomes approximately current independent (see Fig. 5.7(c)). We suggest that, at high dH/dt values, the flux penetration is prevented by the localized shielding currents circulating around the grains (negative diamagnetic response) in parallel to the rate of variation of external magnetic field. The penetrated flux lines can be pinned by the pinning centers inside the grains and can not find enough time to move through the grains. Thus, a relative increase in the flux pinning can evolve as compared to that observed at low values of dH/dt , which can cause relatively large irreversibility effects in the $V-H$ curves (see Fig. 4.23).

Figures 5.8 and 5.9 show that $\Delta H = f(H^-)$ data extracted respectively from the $V-H$ curves given in Figs. 4.24-4.26 and Figs. 4.27-4.29 collapse on the same curve and are practically independent of the transport current, but depends on dH/dt . Inspection of Eq. 2.15 and the current independence the $\Delta H = f(H^-)$



H^- (mT)

H^- (mT)

Figure 5.8 $\Delta H = f(H^-)$ curves of the YBCO/Ag sample determined at $T = 84$ K for different current values and magnetic field sweep rates **a)** $dH/dt = 0.50$ mT/s **b)** $dH/dt = 1.30$ mT/s **c)** $dH/dt = 2.60$ mT/s. The data were extracted from the $V - H$ curves in Figs. 4.24-4.26

Figure 5.9 $\Delta H = f(H^-)$ curves of the YBCO/Ag sample determined at $T = 82$ K for different current values and magnetic field sweep rates **a)** $dH/dt = 0.50$ mT/s **b)** $dH/dt = 1.30$ mT/s **c)** $dH/dt = 2.60$ mT/s. The data were extracted from the $V - H$ curves in Figs. 4.27-4.29.

curves reveal that the flux trapping in grains dominates the evolution of the $V - H$ curves. We suggest that the contribution from the pinning of junction network to the hysteresis loops at $T = 84$ and 82 K is negligible. Further, the transport current does not affect the flux lines pinned inside the grains.

Figure 5.10 shows the variation of ΔH_{\max} with dH/dt , where ΔH_{\max} corresponds to the maximum values of the $\Delta H = f(H^-)$ curves presented in Figs. 5.7-5.9.

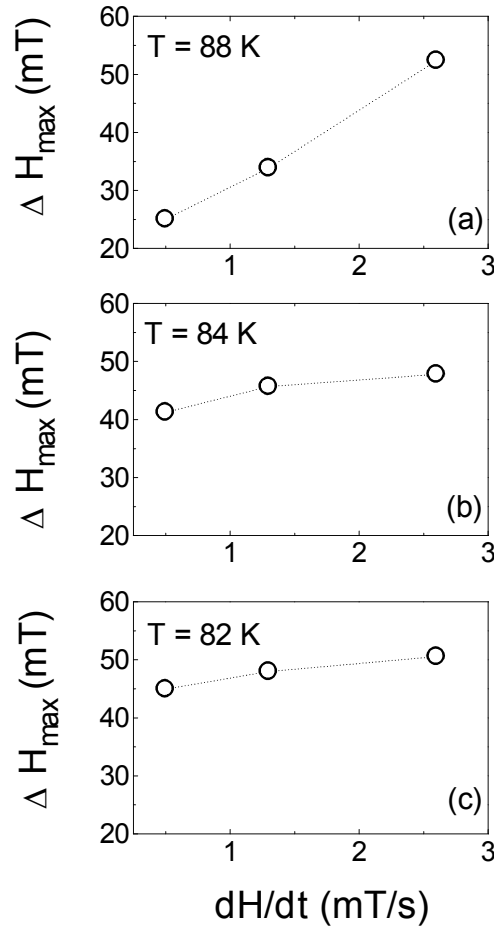


Figure 5.10 The variation of ΔH_{\max} with dH/dt determined at different temperatures: **a)** $T = 88$ K, **b)** $T = 84$ K and **c)** $T = 82$ K. ΔH_{\max} is the maximum value of the $\Delta H - H$ curves presented in Figs. 5.7-5.9.

At $T = 88$ K, ΔH_{\max} increases with increasing dH/dt (Fig 5.10(a)). However, this significant dependence of ΔH_{\max} on dH/dt diminishes with decreasing the temperature from $T = 88$ to 84 K. The similarity between the $\Delta H = f(H^-)$ curves in Fig. 5.10(b) and 5.10(c) implies that the same physical mechanism controls (the flux trapping evolving inside the grains) the evolution of the $V - H$ curves measured at $T = 82$ and 84 K.

Figure 5.11 shows the variation of ΔH with H^- for the undoped YBCO sample determined at different transport currents. The data were extracted from the $V - H$ curves in Fig. 4.30. It is seen that all data points fall on the same curve for $H^- \gtrsim 25$ mT, except those for $I = 30$ mA. The $\Delta H = f(H^-)$ curve determined for $I = 30$ mA follow the same curve when $H \geq 42$ mT. At low currents ($I = 30, 40$ and 50 mA), there is a current dependence of ΔH . We attribute this dependence to the flux pinning in the junction network and also to the contribution of the magnetization of intergranular region M_i to ΔH . Since ΔH is a measure of the difference between the forward and backward magnetizations (see Eqs. 2.18 and 2.19), the magnetic states evolved for $I = 30$ mA should be different up to $H \sim 42$ mT as compared to that observed for other current values. In this description, the diamagnetic response of the sample reaches its highest value, and the flux penetration and motion nearly disappear for $H \lesssim 42$ mT.

Finally, we comment on the general behavior of $\Delta H = f(H^-)$ curves. It is seen from Figs. 5.8, 5.9 and 5.11 that ΔH generally tends to increase linearly with increasing H^- . This implies that the net magnetization due to the difference

between forward and backward magnetizations enhances with H^- . However a decrease in ΔH with respect to H^- can be correlated to the beginning of decrease in difference between forward and backward magnetizations.

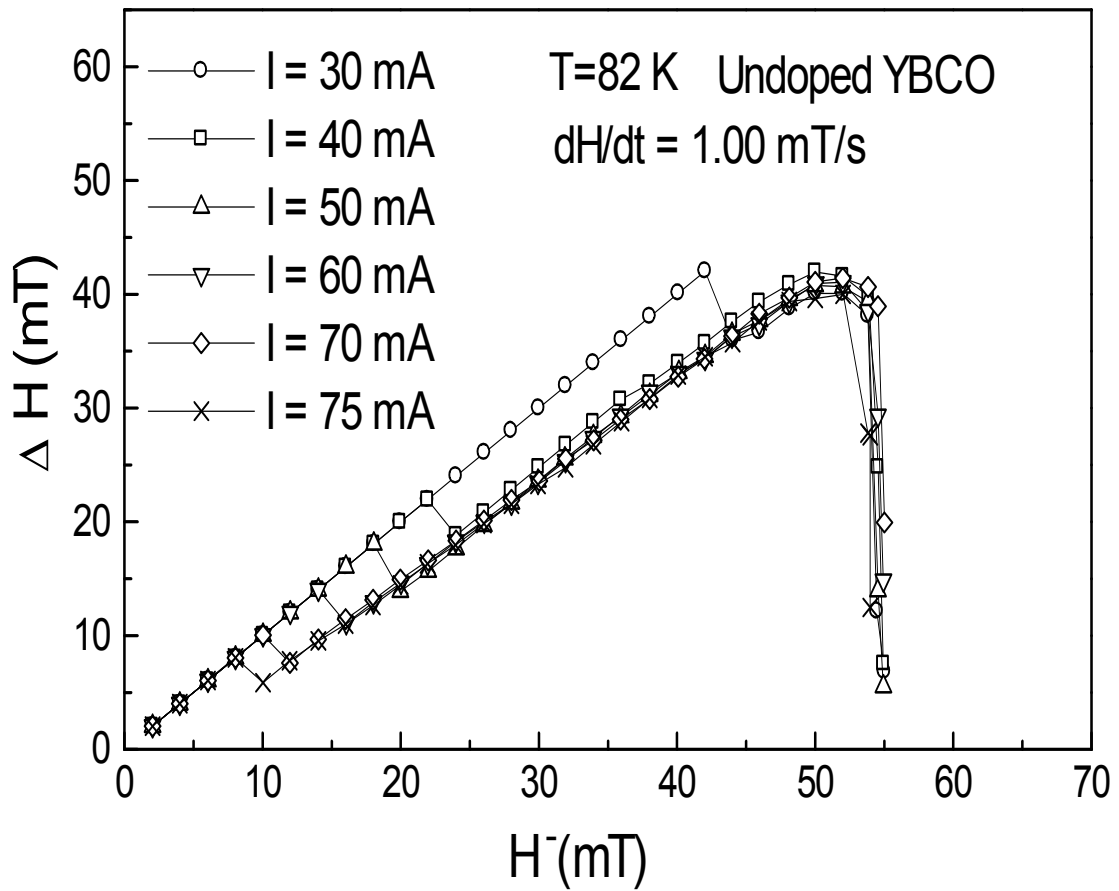


Figure 5.11 $\Delta H = f(H^-)$ curves of undoped the YBCO/Ag sample determined at $T = 82$ K for different current values and magnetic field sweep rate $dH/dt = 1.00$ mT/s. The data were extracted from the $V - H$ curves in Fig. 4.30.

CHAPTER 6

CONCLUSION

In this study, systematic transport and transport relaxation measurements were made in Ag doped polycrystalline $Y_1Ba_2Cu_3O_{7-x}$ sample (YBCO/Ag) as functions of transport current (I), temperature (T) and external magnetic field (H).

The current-voltage measurements ($I-V$ curves) with different current sweep rates (dI/dt), the transport relaxation measurements ($V-t$ curves) by using dc and bi-directional square wave (BSW) currents, and the magnetovoltage measurements ($V-H$ curves) with different sweep rates of the external magnetic fields (dH/dt) were carried out to investigate the effects of Ag-doping on the flux dynamics in YBCO. In order to understand better the flux dynamics evolving in YBCO/Ag, the results of present measurements were compared to our previous studies on polycrystalline samples of undoped YBCO and MgB_2 .

Standard and reverse procedures were used in the measurements of $I-V$ curves. In the standard procedure, the dc driving current is cycled up [current increase (CI) branch] and down [current decrease (CD) branch]; whereas, in the reverse procedure, the current is first cycled down [current decrease (RCD) branch] and, then, up [current decrease (RCI) branch]. The reverse procedure enables us to

investigate the flux motion evolving from the outer surface of the sample to its interior.

Upon cycling transport current, the $I - V$ curves of the YBCO/Ag sample exhibit hysteresis effects for both procedures and are sensitive to the variation of dI/dt . The experimental data reveal that the irreversibilities in the $I - V$ curves of undoped YBCO are more prominent than those of YBCO/Ag. Furthermore, there are no considerable hysteresis effects in the $I - V$ curve of MgB_2 , a behavior attributed to the absence of weak-link structure. We suggest that the physical origin of the rather small hysteresis effects in the $I - V$ curves of the YBCO/Ag sample can be related to the destruction of weak-link structure due to the Ag-doping into the superconducting structure. Ag destroys partly the intergranular pinning properties of YBCO ceramic by increasing grain coupling. As a consequence, the irreversibilities in the $I - V$ curves of YBCO/Ag decrease considerably. On the other hand, at moderate dissipation levels, we could not observe any difference between the data obtained by using the standard and reverse procedures. This suggests that the surface effects are also weakened by addition of Ag into the superconducting structure. The hysteresis effects in the $I - V$ curves of YBCO/Ag were explained in terms of different degree of the inhomogeneous flux motion between the current-increase and current-decrease branches.

One of the main observations in the $I - V$ curves of YBCO/Ag is the peculiar voltage jumps and drops. It was found that these instabilities depend strongly on

the magnitude of external parameters dI/dt and H . The voltage jumps and drops in $I - V$ curves disappear as dI/dt is reduced from 1.25 to 0.312 mA/s so that the $I - V$ curves become more smooth. We suggest, at low values of dI/dt , that the flux lines distribute themselves easily and find enough time to go to accessible states. It was observed that the instabilities increase significantly as the external magnetic field is increased from 10 to 20 mT. This behavior was correlated with the increase in the number of the flux lines per unit area of junction network and also to the accumulation of flux lines along the grain boundaries. Such a case can make the flux lines unstable and can reinforce the plastic motion along easy motion channels. In addition, the instabilities and short and long lived plateau regions observed in $I - V$ curves were explained in terms of plastic flow of flux lines along easy motion channels which are considered mainly as metallic silver paths in the YBCO/Ag sample.

Nonlinear transport phenomena and time effects in the YBCO/Ag sample were investigated by the time evolution of sample voltage ($V - t$ curves) on long time scales. The general behavior of the $V - t$ curves was discussed in the frame of dynamic competition between pinning and depinning mechanisms. At early times of the relaxation process, the sample voltage rises sharply and levels off within a very short time. After reducing the initial current (I_1) to a finite value (I_2), the sample voltage first decreases and levels off within a very short time. The rapid voltage drops in the $V - t$ curves observed in the quenched state were attributed to the rapid dynamic reorganization of flux lines traversing the sample edges. When the driving current (I_1) was interrupted to zero, it was observed that the measured

voltage becomes zero. This finding indicated that there is no residual voltage to be relaxed and no heating effects associated with current contacts or hot-spot in the sample. The initial voltage drop in the quenched state shows a decay exponentially, as in the case of glassy state.

Furthermore, the time evolution of the $V - t$ curves of YBCO/Ag in the quenched state is quite different from that of undoped YBCO. At high and moderate dissipation levels, the random distribution of Ag atoms in superconducting structure is one of the major reasons which affect the line shape and the general behavior of $V - t$ curves. Ag suppresses easily the superconducting order parameter along the intergranular regions and forms additional easy motion channels for the flux lines. That is why the rapid rise in the sample voltage at early times of relaxation process is observed and also the sudden drop in the sample voltage evolves in the $V - t$ curves as the initial transport current I_1 is reduced to a lower value I_2 .

We also investigated the influence of bi-directional square wave (BSW) current on the evolution of $V - t$ curves as functions of the amplitude and period of the BSW current at different temperatures and external magnetic fields. It was observed that slow transport relaxation measurements result in regular sinusoidal voltage oscillations. The symmetry in the voltage oscillations was attributed to the elastic coupling between the flux lines and the pinning centers along grain boundaries and partly inside the grains. This case was also correlated to the

equality between flux entry and exit along the YBCO/Ag sample during regular oscillations.

It was shown that the voltage oscillations can be described well by an empirical expression $V(t) \sim \sin(\omega t + \phi)$ (see Eq 5.6). We found that the phase angle ϕ generally takes different values for the repetitive oscillations. We suggest that, for each cycle observed, the initial conditions of the flux lines joining the motion are determined by the distribution of flux lines formed by the former cycle and, thus, every cycle prepares new initial condition for the next cycle. Therefore, it is natural to expect such phase difference between successive oscillations.

Fast Fourier Transform analysis of the $V - t$ oscillations showed that the oscillation period is comparable to that (P_I) of the BSW current. This finding suggests a physical mechanism associated with charge density waves (CDWs), and, indeed, the weakly pinned flux line system in YBCO/Ag resembles the general behavior of CDWs. At certain values of P_I , amplitude of BSW current, H and T , the YBCO/Ag sample behaves like a double-integrator, since it converts the BSW current to sinusoidal voltage oscillations in time.

The magnetovoltage measurements ($V - H$ curves) were carried out as functions of the transport current (I), sweep rate of the external magnetic field dH/dt , and temperature (T). Upon cycling H , all $V - H$ curves measured for different values of I exhibit a clockwise hysteresis effects. It was observed that the evolution of the $V - H$ curves depends on dH/dt . We note that the rate of number of the flux lines

penetrating into the sample is controlled mainly by dH/dt . At low values of dH/dt , the irreversibilities and instabilities together with plateau regions in the $V - H$ curves decrease markedly. However, the measured voltage dissipation is independent of dH/dt values considered in this study. At low values of dH/dt , the flux lines find enough time to change their states gradually and, therefore, instabilities such as sharp drops or jumps are not observed in the $V - H$ curves. This also explains why the hysteresis effects increase with increasing dH/dt . The hysteresis effects in the $V - H$ curves increase as the temperature is decreased from 88 K to 82 K, which can be correlated directly to the increase in the flux pinning.

The hysteresis effects in the $V - H$ curve were interpreted in terms of two-level magnetic system, which considers the superposition of the external magnetic field and the local magnetic fields in the inter-grain boundaries induced by magnetic dipole moment of neighbor superconducting grains. The general behavior of the $V - H$ curves was also examined in details by using a model proposed by Balaev *et al.* [176]. The analysis of the $V - H$ curves revealed that the irreversibilities arise mainly from the flux trapping inside the grains. Furthermore, our analysis showed that the flux trapping in the junction network has a negligible effect on the evolution of the $V - H$ curves.

The $V - H$ curves of the YBCO/Ag sample were also compared to those of undoped YBCO sample. The presence of Ag in the superconducting structure causes marked decrease in hysteresis effects. Another interesting finding is the

pronounced decrease in the number of voltage drops/jumps and plateau regions in $V-H$ curves of undoped YBCO. This implies that the addition of Ag into YBCO material leads to a decrease in flux pinning properties in the intergranular region.

Finally, many experimental observations have demonstrated that the optimum addition of Ag into YBCO improves its magnetic and transport properties. Ag does not react with decomposed phases and tends to stay on the grain boundaries as a metallic form. It is naturally expected that the addition of Ag into YBCO can cause an increase in the number of formation of superconductor – metal-superconductor (S-N-S) junctions between the grains. Thus, the coupling between grains increases, and the grain boundary resistivity decreases markedly. The improved grain connectivity of a superconducting material (i.e., HTSC cuprates) is important for practical applications. Therefore, it will be interesting to dope YBCO with other non-magnetic metallic materials such as Au, Al, Ca, etc. in different amounts. In the future, we are planning to make such studies.

REFERENCES

- [1] G. D'Anna, P.L. Gammel, H. Safar, G.B. Alers, and D.J. Bishop, Vortex Motion-Induced Voltage Noise in $\text{YBa}_2\text{Cu}_3\text{O}_{7-\delta}$ Single Crystals, *Phys. Rev. Lett.* 75: 3521-3524 (1995).
- [2] S.N. Gordeev, P.A.J. de Groot, M. Oussena, A.V. Volkov, S. Pinfold, R. Langan, R. Gagnon, and L. Taillefer, Current-induced organization of vortex motion in type-II superconductors, *Nature* 385: 324-326 (1997).
- [3] W. Henderson, E. Y. Andrei, M. J. Higgins, and S. Bhattacharya, Metastability and glassy behavior of a driven flux-line lattice, *Phys. Rev. Lett.* 77: 2077-2080 (1996).
- [4] W. Henderson, E. Y. Andrei, M. J. Higgins, and S. Bhattacharya, ac Dynamics of a Pinned Flux-Line Lattice, *Phys. Rev. Lett.* 80: 381-384 (1998).
- [5] W. Henderson, E. Y. Andrei, and M. J. Higgins, Plastic motion of a vortex lattice driven by alternating current, *Phys. Rev. Lett.* 81: 2352-2355 (1998).
- [6] Z. L. Xiao, E. Y. Andrei, and M. J. Higgins, Flow induced organization and memory of a vortex lattice, *Phys. Rev. Lett.* 83: 1664-1667 (1999).
- [7] Z.L. Xiao, E.Y. Andrei, P. Shuk, and M. Greenblatt, Equilibration and Dynamic Phase Transitions of a Driven Vortex Lattice, *Phys. Rev. Lett.* 85: 3265-3268 (2000).
- [8] Z. L. Xiao, E. Y. Andrei, P. Shuk, and M. Greenblatt, Joule heating induced by vortex motion in a type-II superconductor, *Phys. Rev. B* 64: 094511 (2001).
- [9] Z.L. Xiao, E.Y. Andrei, P. Shuk, and M. Greenblatt, Depinning of a Metastable Disordered Vortex Lattice, *Phys. Rev. Lett.* 86: 2431-2434 (2001).
- [10] Z. L. Xiao, O. Dogru, E. Y. Andrei, P. Shuk and M. Greenblatt, observation of vortex latticespinodal in NbSe_2 , *Phys. Rev. Lett.* 92: 227004 (2004).
- [11] A. Kiliç, K. Kiliç and O. Çetin, Vortex instability and time effects in $I-V$ curves of superconducting $\text{Y}_1\text{Ba}_2\text{Cu}_3\text{O}_{7-\delta}$, *J. Appl. Phys.* 93:1, (2003) *Virtual Journal of Appl. of Supercon.*, Vol 4, issue 1: (2003).

- [12] K. Kiliç, A. Kiliç, H. Yetiş and O. Çetin, Low-field transport relaxation measurements in superconducting $Y_1Ba_2Cu_3O_{7-\delta}$, *Phys. Rev. B* 68: 144513 (2003); *Virtual J. Appl. Supercon*, Vol 5, issue 8: (2003).
- [13] K. Kiliç, A. Kiliç, H. Yetiş, and O. Çetin, Transport relaxation phenomena in superconducting $Y_1Ba_2Cu_3O_{7-\delta}$, *J. Appl. Phys.* 95: 1924 (2004).
- [14] K. Kiliç, A. Kiliç, A. Altinkok, H. Yetiş, O. Çetin, and Y. Durust, Time evolution of quenched state and correlation to glassy effects, *Physica C* 420: 1-10 (2005).
- [15] Y. Paltiel, E. Zeldov, Y.N. Myasoedov, M. L. Rappaport, G. Jung, S. Bhattacharya, M. J. Higgins, Z.L. Xiao, E. Y. Andrei, P. L. Gammel and D.J. Bishop, Instabilities and Disorder-Driven First-Order Transition of the Vortex Lattice, *Phys. Rev. Lett.* 85: 3712-3715 (2000).
- [16] S. Bhattacharya and M.J. Higgins, Dynamics of a disordered flux line lattice, *Phys. Rev. Lett.* 70: 2617-2620 (1993).
- [17] T. Giamarchi and P. Le Doussal, Moving Glass Phase of Driven Lattices, *Phys. Rev. Lett.* 76: 3408-3411 (1996).
- [18] C. J. van der Beek, S. Colson, M. V. Indenbom, and M. Konczykowski, Supercooling of the Disordered Vortex Lattice in $Bi_2Sr_2CaCu_2O_{8+\delta}$ Lattices, *Phys. Rev. Lett.* 84: 4196-4199 (2000).
- [19] C. Rossel, Y. Maeno, and I. Morgenstern, Memory Effects in a Superconducting Y-Ba-Cu-O Single Crystal: A Similarity to Spin-Glasses, *Phys. Rev. Lett.* 62: 681-684 (1989).
- [20] V. B. Geshkenbein, L. B. Ioffe and A. I. Larkin, Nature of hysteresis in glass transitions of the first order, *Phys. Rev. B* 48: 9917-9920 (1993).
- [21] B. Sas, F. Portier, K. Vad, B. Keszei, L. F. Kiss, N. Hegman, I. Puha, S. Meszaros, and F. I. B. Williams, Metastability line in the phase diagram of vortices in $Bi_2Sr_2CaCu_2O_8$, *Phys. Rev. B* 61: 9118-9121 (2000).
- [22] Y. Paltiel, E. Zeldov, Y.N. Myasoedov, H. Shtrikman, S. Bhattacharya, M.J. Higgins, Z.L. Xiao, P.L. Gammel, and D.J. Bishop, Dynamic instabilities and memory effects in vortex matter, *Nature* 403: 398-401 (2000).
- [23] M. Danckwerts, A. R. Goñi, and C. Thomsen, Direct evidence for filamentary and channel vortex flow in Pb/In superconducting films, *Phys. Rev. B* 59: R6624-R6627 (1999).
- [24] A. Kiliç, K. Kiliç and O. Çetin, Vortex instability and hysteresis effects in $I-V$ curves of superconducting $Y_1Ba_2Cu_3O_{7-\delta}$, *Physica C* 384: 321 (2003).

- [25] J. A. Fendrich, U. Welp, W. K. Kwok, A. E. Koshelev, G. W. Craptree and B. W. Veal, Static and Dynamic Vortex Phases in $YBa_2Cu_3O_{7-\delta}$, *Phys. Rev. Lett.* 77: 2073 (1996).
- [26] P P. Usák, L. Jansák and M. Polák, Hysteresis of $V-I$ curve of BSCCO-2223 tape, *Physica C* 350: 139-146 (2001).
- [27] H. Yetiş, A. Kiliç, K. Kiliç, A. Altinkok and M. Olutaş, Observation of unusual irreversible/reversible effects in a macroscopic cylindrical hole drilled in superconducting Bi-Sr-Ca-Cu-O, *Physica C* 468:1435 (2008).
- [28] A. Altinkok, K. Kiliç, A. Kiliç, H. Yetiş and M. Olutaş, Transport Relaxation Measurements in Ag-Doped Superconducting Y-Ba-Cu-O, *IEEE Trans. Appl. Supercond.* 19: 2978-2983 (2009).
- [29] A. V. Samoilov, M. Konczykowski, N.C. Yeh, S. Berry, and C. C. Tsuei, Electric-Field-Induced Electronic Instability in Amorphous Mo_3Si Superconducting Films, *Phys. Rev. Lett.* 75: 4118 (1995).
- [30] Y. Liu, H. Luo, X. Leng, Z. H. Wang, L. Qiu, S. Y. Ding and L. Z. Lin, History effect in inhomogeneous superconductors, *Phys. Rev. B* 66: 144510 (2002).
- [31] Dan Goldschmidt, Critical currents and current-voltage characteristics in superconducting ceramic $YBa_2Cu_3O_{7-\delta}$, *Phys. Rev. B* 39: 9139 (1989).
- [32] A. Pautrat, Ch. Simon, J. Scola, C. Goupil, A. Ruyter, L. Ammor, P. Thopart and D. Plessis, On voltage-current characteristics and critical current in Bi-2212, *Eur. Phys. J. B* 43: 39-45 (2005).
- [33] Hyun-Sook Lee, Dong-Jin Jang, Heon-Jung Kim, Byeongwon Kang, Sung-Ik Lee, Peak effect and vortex dynamics in superconducting MgB_2 single crystals, *Physica C* 456: 153-159 (2007).
- [34] S. Y. Ding, C. Ren, X. X. Yao, Y. Sun, H. Zhang, Effect of current sweep rate on critical current of superconducting Ag-Bi-2223 tapes, *Cryogenics* 38: 809-812 (1998).
- [35] Y. H. Zhang, S. Y. Ding, H. Luo, X. F. Wu, P. Zhang, F. Y. Lin, L. Qiu, Z. Xu, X. X. Yao, Dynamic response of Ag-Bi2223 tapes in applied fields by electric transport measurement, *Cryogenics* 40: 29-34 (2000).
- [36] A. Kilic and K. Kilic, Influence of the current sweep rate on vortex dynamics in superconducting YBCO, *Physica C* 372: 1862-1864 (2002).
- [37] I. Hiltunen, A. Korpela, J. Lehtonen, R. Mikkonen, Influence of current ramp rate on voltage current measurement of a conduction-cooled HTS magnet, *Physica C* 468: 903-907 (2008).

- [38] P. Zhang, C. Ren, S. Y. Ding, Q. Ding, F. Y. Lin, Y. H. Zhang, H. Luo, and X. X. Yao, Effect of electric field relaxation on the V - I curve, *Supercond. Sci. Technol.* 12: 571 (1999).
- [39] Y. H. Zhang, H. Luo, X. F. Wu, and S. Y. Ding, Effect of flux creep on I_c measurement of electric transport, *Supercond. Sci. Technol.* 14: 346 (2001).
- [40] S. Y. Ding, H. Luo, Y. H. Zhang, Q. Ding, F. Y. Ling, P. Zhang, X. F. Wu, L. Qiu and X. X. Yao, Voltage Relaxation and Its Influence on Critical Current Measurements, *J. Supercond.* 13: 543 (2000).
- [41] X. B. Xu, L. Zhang, S. Y. Ding, X. Leng, Z. H. Wang and X. L. Wang, Dynamical hysteresis V - I curves of superconductors, *Supercond. Sci. Technol.* 18: 758-762 (2005).
- [42] A. Altinkok, H. Yetiş, K. Kiliç, A. Kiliç and M. Olutaş, Slow voltage oscillations in Ag-doped superconducting Y-Ba-Cu-O, *Physica C* 468: 1419-1423 (2008).
- [43] A. Kiliç, K. Kiliç, H. Yetiş, M. Olutaş, A. Altinkok, H. Sözeri, and O. Çetin, Flux trapping in a macroscopic cylindrical hole drilled in Bi-Sr-Ca-Cu-O, *Eur. Phys. J. B* 50: 565-569 (2006).
- [44] G. Li, E. Andrei, X. Du, Z. L. Xiao, P. Shuk and M. Greenblatt, Onset of motion and glassy dynamics of a moving vortex lattice, *J. de Physique IV* 131: 101-106 (2005).
- [45] G. Li, E. Andrei, X. Du, Z. L. Xiao, P. Shuk and M. Greenblatt, Onset of Motion and Dynamic Reordering of a Vortex Lattice, *Phys. Rev. Lett.* 96: 017009-017013 (2006).
- [46] X. Du, G. Li, E. Andrei, M. Greenblatt and P. Shuk, Ageing memory and glassiness of a driven vortex system, *Nature Phys.* 3: 111-114 (2007).
- [47] Yu. S. Karimov and A. D. Kikin, New relaxation phenomena in high- T_c ceramic superconductors, *Physica C* 169: 50 (1990).
- [48] W. Henderson, E. Y. Andrei, and M. J. Higgins, Plastic motion of a vortex lattice driven by alternating current, *Phys. Rev. Lett.* 81: 2352-2355 (1998).
- [49] S.N. Gordeev, P.A.J. de Groot, M. Oussena, R.M. Langan, A.P. Rassau, R. Gagnon, and L. Taillefer, Organisation of vortex motion in detwinned YBa₂Cu₃O_{7- δ} single crystals, *Physica C* 282: 2033-2034 (1997).
- [50] K. Kiliç, A. Kiliç, A. Altinkok, H. Yetiş and O. Çetin, Current-induced voltage oscillations in superconducting Y₁Ba₂Cu₃O_{7- δ} , *Eur. Phys. J. B* 48: 189-197 (2005).

- [51] A. Kiliç, K. Kiliç, H. Yetiş and O. Çetin, Low-field magnetovoltage measurements in superconducting YBCO, *New J. Phys.* 7: 212 (2005).
- [52] S. Senoussi, Review of the critical current density and magnetic irreversibilities in high T_c superconductors, *J. Phys. (Paris) III* 2: 1041(1992).
- [53] L. Ji, M. S. Rzchowski, N. Anand, and M. Tinkham, Magnetic-field-dependent surface resistance and two-level critical-state model for granular superconductors, *Phys. Rev. B.* 47: 470 (1993).
- [54] M. Mahel and J. Pivarc, Magnetic hysteresis in high-temperature cuprates, *Physica C* 308: 147-160 (1998).
- [55] D. A. Balaev, D. M. Gokhfeld, A. A. Dubrovskii, S. I. Popkov, K. A. Shaikhutdinov and M. I. Petrov, Magnetoresistance hysteresis in granular HTSCs as a manifestation of the magnetic flux trapped by superconducting grains in YBCO + CuO composites, *J. of Experimental and Theoretical Physics* 105: 1174-1183 (2007).
- [56] D. A. Balaev, D. M. Gokhfeld, A. A. Dubrovskii, S. I. Popkov, K. A. Shaikhutdinov and M. I. Petrov, Mechanism of the hysteretic behavior of the magnetoresistance of granular HTSCs: The universal nature of the width of the magnetoresistance hysteresis loop, *J. of Experimental and Theoretical Physics* 108: 241-248 (2009).
- [57] D. A. Balaev, A. A. Bykov, S. V. Semenov, S. I. Popkov, A. A. Dubrovskii, K. A. Shaikhutdinov and M. I. Petrov, General regularities of magnetoresistive effects in the polycrystalline yttrium and bismuth high-temperature superconductor systems, *Physics of The Solid State* 53: 922-932 (2010).
- [58] C. Leblond-Harris, R. Caillard, I. Monot-Laffez, G. Desgardin, B. Raveau, Texturing process, superconducting and mechanical properties of Ag-doped top-seeded melt-grown YBCO pellets, *Physica C* 341–348: 2439–2440 (2000).
- [59] Y. Li, J.R. Liu, X.T. Cui, Y. Cao, Z.J. Qu, Q.Y. Chen, C.W. Chu, W.K. Chu, On the role of Ag in improved $\text{YBa}_2\text{Cu}_3\text{O}_{7-\delta}$ films, *Physica C* 282–287: 653–654 (1997).
- [60] C. Harnois, G. Desgardin, I. Laffez, X. Chaud, D. Bourgault, High quality weld of melt textured YBCO using Ag doped YBCO junctions, *Physica C* 383: 269–278 (2002).
- [61] T. Puig, P. Rodriguez Jr., A.E. Carrillo, X. Obradors, H. Zheng, U. Welp, L. Chen, H. Claus, B.W. Veal, G.W. Crabtree, Self-seeded YBCO welding induced by Ag additives, *Physica C* 363: 75–79 (2001).

- [62] E. Mendoza, T. Puig, E. Varesi, A.E. Carrillo, J. Plain, X. Obradors, Critical current enhancement in YBCO–Ag melt-textured composites: influence of microcrack density, *Physica C* 334: 7–14 (2000).
- [63] M.M. Abdelhadi, Kh.A. Ziq, The behaviour of the flux flow resistance in YBCO/(Ag₂O)_x, *Supercond. Sci. Technol.* 7: 99–102 (1994).
- [64] J.Y. Matsumoto, M. Koinuma, H. Yamamoto, T. Nishimori, Electrochemical Ag doping into Yba₂Cu₃O_y, ceramics using Ag -β"-Al₂O₃ ionic conductor, *Solid State Ionics* 95: 309–314 (1997).
- [65] P.L. Villa, G. Taglieri, F. D’Orazio, F. Lucari, G. Santella, L. Catoni, S. Lozzi, Harmonic analysis of AC magnetic susceptibility of YBCO/Ag produced by chemical amorphous citrate route, *J. Magn. Magn. Mater.* 226-230: 314–315 (2001).
- [66] G. T. Goudey, K. Winsley and D. Shi, Effect of silver and silver oxide additions on the mechanical and superconducting properties of YBa₂Cu₃O_{7-δ} superconductors, *J. Appl. Phys.* 66: 3154-3159 (1989).
- [67] S. Sen, In-Gann. C. H. Chen and D. M. Stefanescu, Fabrication of stable superconductive wires with YBa₂Cu₃O_x/Ag₂O composite core, *Appl. Phys. Lett.* 54: 766-768 (1989).
- [68] J. Jung, M. A. K. Mohamed, S. C. Cheng and J. P. Franck, Flux motion, proximity effect, and critical current density in YBa₂Cu₃O_{7-δ} / silver composites, *Phys. Rev. B* 42: 6181-6195 (1990).
- [69] D. Pavuna, H. Berget, M. Affronte, J. Van der Maas, J. J. Capponi, M. Guillot, P. Lejay and I. L. Tholance, electronic properties and critical current densities of superconducting (YBa₂Cu₃O_{6.9})_{1-x}Ag_x compounds, *Solid State Commun.* 68: 535-538 (1988).
- [70] Y. Xu, W. Guan, K. Zeibig and C. Heiden, Magnetic hysteresis and critical current densities of polycrystalline REBa₂Cu₃O_{7-y}, *Cryogenics* 29: 281-285 (1988).
- [71] N. Peter, R. C. Sisk, E. W. Urban, C. Hang and M. K. Wu, Observation of enhanced properties in samples of silver oxide doped YBa₂Cu₃O_x, *Appl. Phys. Lett.* 52: 2066-2067 (1989).
- [72] M.K. Malik, V. D. Nair, A. R. Biswas, R. V. Raghavan, P. Chaddah, P. K. Mishra, G. Ravi Kumar, and B. A. Dasannacharya, Texture formation and enhanced critical currents in YBa₂Cu₃O₇, *Appl. Phys. Lett.*, 52: 1525-1527 (1988).
- [73] H. Kamerling Onnes, The Superconductivity of Mercury, *Comm. Phys. Lab. Univ. Leiden* 122 and 124: 1226 (1911).

- [74] W. Meissner, and R. Ochsenfeld, Ein neuer Effekt bei Eintritt der supraleitfähigkeit, *Naturwissenschaften* 21: 787-788 (1933).
- [75] A. A. Abrikosov, On the magnetic properties of Superconductors of the Second group, *JETP* 5: 1174 (1957).
- [76] J. R. Galaver, Superconductivity in Nb₃Ge films above 22 K, *Appl. Phys. Lett.* 23: 480-482 (1973).
- [77] J. G. Bednorz and K. A. Müller, Possible high-T_c superconductivity in the Ba-La-Cu-O system, *Z. Phys. B* 64: 189 (1986).
- [78] M. K. Wu, J. R. Ashburn, C. J. Torng P. H. Hor, R. L. Meng, L. Gao, Z. J. Huang, Y. Q. Wang, and C. W. Chu, Superconductivity at 93 K in a new mixed-phase Y-Ba-Cu-O compound system at ambient pressure, *Phys. Rev. Lett.* 58: 908-910 (1987).
- [79] Hiroshi Maeda, Yoshiaki Tanaka, Masao Fukutomi and Toshihisa Asano, A New High-T_c Oxide Superconductor without a Rare Earth Element, *Jpn. J. Appl. Phys.* Vol. 27: L209-L210 (1988).
- [80] Z. Z. Sheng, A. M. Hermann, A. El Ali C. Almasan, J. Estrada, T. Datta and R. J. Matson, Superconductivity at 90 K in the Tl-Ba-Cu-O system, *Phys. Rev. Lett.* 60: 937-940 (1988).
- [81] A. Schilling, M. Cantoni, J. D. Guo & H. R. Ott, Superconductivity above 130 K in the Hg-Ba-Ca-Cu-O system, *Nature* 363: 56 - 58 (1993).
- [82] L. Gao, Y. Y. Xue, F. Chen, Q. Xiong, R. L. Meng, D. Ramirez, C. W. Chu, J. H. Eggert, and H. K. Mao, Superconductivity up to 164 K in HgBa₂Ca_{m-1}Cu_mO_{2m+2+δ} (m=1, 2, and 3) under quasihydrostatic pressures, *Phys. Rev. B* 50 (6): 4260-4263 (1994).
- [83] J. Nagamatsu, N. Nakagawa, T. Muranaka, Y. Zenitani and J. Akimitsu, Superconductivity at 39 K in magnesium diboride, *Nature* 410: 63 (2001).
- [84] G. Wu, Y. L. Xie, H. Chen, M. Zhong, R. H. Liu, B. C. Shi, Q. J. Li, X. F. Wang, T. Wu, Y. J. Yan, J. J. Ying, and X. H. Chen, Superconductivity at 56 K in samarium-doped SrFeAsF, *J. of Phys.: Condens. Matter* 21: 142203 (2009).
- [85] C. P. Poole, H. A. Farach, R. J. Creswick, R. Prozorov, Superconductivity, *Academic Press Elsevier*, P. 42-44 (2007)
- [86] C. Kittel, Introduction to solid state physics, *John Wiley & Sons, Inc., USA*, p.339-351 (1996).
- [87] F. London, Superfluids, *Wiley, New York* (1950).

- [88] D. Shoenberg, Superconductivity, Cambridge: *Cambridge University Press*, p. 194-195 (1952).
- [89] M. Tinkham, Introduction to Superconductivity, *New-York: McGraw-Hill*, (1975).
- [90] I. A. Parinov, Microstructure and properties of high-temperature superconductors, Springer, p. 21-23 (2007)
- [91] A.C. Rose-Innes and E.H. Rhoderick, Introduction to Superconductivity, *Oxford: Pergamon Press* (1978).
- [92] V. L. Ginzburg, and L. D. Landau, On the Theory of Superconductivity, *Zh. Eksperim. I Teor. Fiz.* 20: 1064 (1950).
- [93] J. Bardeen, L.N. Cooper and J.R. Schreiffner, Theory of superconductivity, *Phys. Rev.* 108: 1175-1204 (1957).
- [94] L. N. Cooper, Bound Electron Pairs in a Degenerate Fermi Gas, *Phys. Rev.* 104: 1189-1190 (1956).
- [95] James William Rohlf, Modern Physics from α to Z, *John Wiley & Sons, Inc.* (1994)
- [96] T.P. Sheahan, Introduction to High-Temperature Superconductivity, *New York: Plenum Press* (1994)
- [97] M. Cyrot and D. Pavuna, Introduction to Superconductivity and High – T_c Materials, *World Scientific* (1992).
- [98] Y. B. Kim, C. F. Hempstead, and A. R. Strnad, Flux-Flow Resistance in Type-II Superconductors, *Phys. Rev.* 139: A1163–A1172, (1965)
- [99] P.G. De Gennes, Superconductivity of metals and alloys, *Benjamin, Newyork* (1966).
- [100] J.F. Kwak, E.L. Venturini, D.S. Ginley and W. Fu, Novel Superconductivity, *Plenum, Newyork* (1987).
- [101] E. Altshuler, J. Musa, J. Barroso, A. R. R. Papa and V. Venega, Generation of $J_c(H_e)$ hysteresis curves for granular $YBa_2Cu_3O_{7-\delta}$ superconductors, *Cryogenics* 33: 308-313 (1993).
- [102] P. Mune, F. C. Foncesa, R. Muccillo, and R. F. Jardim, Magnetic hysteresis of the magnetoresistance and the critical current density in polycrystalline $YBa_2Cu_3O_{7-\delta}$ -Ag superconductors, *Physica C* 390: 363-373 (2003).

- [103] I. Felner, E. Galstyan, B. Lorenz, D. Cao, Y. S. Wang, Y. Y. Xue and C. W. Chu, Magnetoresistance hysteresis and critical current density in granular $\text{RuSr}_2\text{Gd}_{2-x}\text{Ce}_x\text{Cu}_2\text{O}_{10-\delta}$, *Phys. Rev. B* 67:134506-134511 (2003).
- [104] K. A. Müller, M. Takashige, and J. G. Bednorz, Flux trapping and superconductive glass state in $\text{La}_2\text{CuO}_{4-y}\text{:Ba}$, *Phys. Rev. Lett.* 58: 1143–1146 (1987).
- [105] S. Pinol, V. Gomis, A. Gou, B. Martinez, J. Fontcuberta and X. Obradors, Oxygenation and aging processes in melt textured $\text{YBa}_2\text{Cu}_3\text{O}_{7-\delta}$, *Physica C* 235–240: 3045-3046 (1994).
- [106] D. Shi, D. Qu and B. A. Tent, Effect of oxygenation on levitation force in seeded melt grown single-domain $\text{YBa}_2\text{Cu}_3\text{O}_x$, *Physica C* 291, 181-187 (1997).
- [107] T. G. Chen, S. Li, W. Gao, Z. Xianyu, H. K. Liu and S. X. Dou, The oxygenation kinetics of $\text{YBa}_2\text{Cu}_3\text{O}_{7-\delta}$ -(0-30%) Ag superconductors, *Supercond. Sci. Technol.* 11: 1193-1199 (1998).
- [108] C. P. Poole, Handbook of superconductivity, *Academic Press, San Diego* (2000).
- [109] D. M. Ginsberg, Physical properties of high temperature superconductors, *IV. World Scientific, Singapore*, (1994).
- [110] A. W. Hewat, Materials and Crystallographic Aspects of High T_c -Superconductivity, *NATO ASI Series E: Applied Sciences* 263, 17 (1994)
- [111] M. F. Chisholm and S. J. Pennycook, Structural origin of reduced critical currents at $\text{YBa}_2\text{Cu}_3\text{O}_{7-\delta}$ grain boundaries, *Nature* 351: 47-49 (1991).
- [112] J. Rosenblatt, A. Raboutou, P. Peyral, et al., Intragranular and intergranular transitions in Y-Ba-Cu-O ceramics, *Rev. Phys. Appl.* 25: 73-78 (1990)
- [113] T. Petrisor, A. Giurgiu and L. Ciontea, Magnetic field dependence of critical current in YBCO- Ag composite system, *Appl. Supercond*, 1: 1219-1225 (1993)
- [114] N. Wu, H. H. Zern and C. Chen, Low-temperature melt growth of $\text{YBa}_2\text{Cu}_3\text{O}_{7-x}$ / silver composites in partial vacuum, *Physica C* 241: 198-207, (1995)
- [115] D. F. Lee, X. Chaud and K. Salama, Transport current density in bulk oriented-grained $\text{YBa}_2\text{Cu}_3\text{O}_x$ / silver composites, *Physica C*, 181: 81-87, (1991).
- [116] B. Dwir, M. Affronte, and D. Pavuna, Evidence for enhancement of critical current by intergrain Ag in YBaCuO-Ag ceramics, *Appl. Phys. Lett.*, 55: 399-401, (1989)

- [117] M. Majaros, F. Hanik, M. Polak, M. Kedrova, Transport critical current densities In Y–Ag–Ba–Cu–O superconductors, *Modern Physics Letters B* 3: 981-986, (1989)
- [118] J. Lin and Z. Teng-Ming Chen, Percolation and electrical resistivity in the $\text{YBa}_2\text{Cu}_3\text{O}_7 - \text{Ag}$ composite system, *Phys. B - Condensed Matter* 81: 13-17 (1990).
- [119] I. Dhingra, B. K. Das and S.C. Kashyap, Flux dynamics of YBCO/Ag composite, *Bull. Mater. sci.* 17, no:2: 153-162, (1994)
- [120] S. Jin, T. H. Tiefel, R. C. Sherwood, M. E. Davis, R. B. Van Dover, W. G. Kammlott, R. A. Fastnacht and H. D. Keith, High critical currents in Y-Ba-Cu-O superconductors, *Appl. Phys. Lett.* 52: 2074-2076, (1988).
- [121] J. Joo, J.G. Kim and W. Nah, Improvement of mechanical properties of YBCO–Ag composite superconductors made by mixing with metallic Ag powder and AgNO_3 solution, *Supercond. Sci. Technol.* 11: 645-649, (1998).
- [122] G. Bolanos, E. Baca, J. Osorio and P. Prieto, Improvement in the properties of Ag- doped $\text{YBa}_2\text{Cu}_3\text{O}_{7-x}$ grain boundary Josephson junctions, *Phys. Stat. Sol. (b)* 220: 517-520, (2000).
- [123] B. Ropers, F. Carmona and S. Flandroiss, Phenomenological approach to the resistive transition of YBaCuO–Ag superconducting random composites, *Physica C*, 204: 71-78, (1992).
- [124] L. Ganapathi, A. Kumar and J. Narayan, Properties of $\text{YBa}_2\text{Cu}_3\text{O}_{7-\delta}$ composite superconductors, *J. Appl. Phys.*, 66: 5935-5939, (1989).
- [125] P. Jr. Rodrigues, L. Ghivelder, P. Pureur and S. Reich, Resistive transition and fluctuation conductivity in YBaCuO–Ag nonrandom composites, *Physica C*, 211: 13-21 (1993).
- [126] P. Knoll and S. Reich, Morphological and magnetic effects of compaction pressure on $\text{YBa}_2\text{Cu}_3\text{O}_{7-x}$ silver nonrandom composites, *J. Appl. Phys.* 71:1035-1037, (1992).
- [127] S. Reich and I. Felner, Nonrandom ceramic superconductor-metal composites, *J. Appl. Phys.* 67: 388-392, (1990).
- [128] T. D. Dzhafarov, Diffusion in High-Temperature Superconductors, *Phys. Status Solidi (a)*, 158, 335-358, (1996).
- [129] H. Salamati, A.A. Babaei-Brojeny, M. Safa, Investigation of weak links and the role of silver addition on YBCO superconductors, *Supercond. Sci. Technol.* 14: 816-819 (2001).

- [130] Ch. Zhang, A. Kulpa and A. C. D. Chaklader, *Physica C* 252,67 (1995).
- [131] A.K. Gangopadhyay, T.O. Mason, Solubility of Ag in $\text{YBa}_2\text{Cu}_3\text{O}_{6+y}$ and its effect on superconducting properties, *Physica C* 178: 64-70 (1991).
- [132] J. Joo, J.P. Singh, R.B. Poeppel, A.K. Gangopadhyay, T.O. Mason, Effect of silver solubility on microstructure and superconducting properties of $\text{YBa}_2\text{Cu}_{3-x}\text{Ag}_x\text{O}_{7-\delta}$ superconductors, *J. Appl. Phys.* 71: 2351-2355, (1992).
- [133] F. Habbal and W.C. H. Joiner, Hysteresis in the flux flow characteristics of a type-II superconductor associated with the presence of normal metal precipitates, *Journal of Low Temp. Phys.* 32: 239-261 (1978).
- [134] M.C. Hellerqvist, D. Ephron, W.R. White, M.R. Beasley and A. Kapitulnik, Vortex Dynamics in Two-Dimensional Amorphous $\text{Mo}_{77}\text{Ge}_{23}$ Films, *Phys. Rev. Lett.* 76: 4022-4025 (1996).
- [135] J. E. Evetts and B. A. Glowacki, Relation of critical current irreversibility to trapped flux and microstructure in polycrystalline $\text{YBa}_2\text{Cu}_{3-x}\text{Ag}_x\text{O}_7$, *Cryogenics* 28: 641-649 (1988).
- [136] K. Kwasnitza and Ch. Widmer, Hysteretic effects in the flux-flow state of granular high- T_c superconductors, *Physica C* 171: 211-215 (1990).
- [137] T. S. Orlova, A.N. Kudymov, B.I. Smirnov, D.J. Miller, M.T. Lanagan, and K.C. Goretta, Electric field effects on the conductivity of highly textured $\text{Bi}_2\text{Sr}_2\text{CaCu}_2\text{O}_y$ superconductors, *Physica C* 253: 194-198 (1995).
- [138] B. I. Smirnov, T.S. Orlova, A.N. Kudymov, M.T. Lanagan, M.P. Chudzik, N. Chen and K.C. Goretta, Electric field effect in $(\text{BiPb})_2\text{Sr}_2\text{Ca}_2\text{Cu}_3\text{O}_x$ superconductor bars, *Physica C* 273: 255-260 (1997).
- [139] A. I. Larkin and Yu. N. Ovchinnikov, Nonlinear conductivity of superconductors in the mixed state, *Sov. Phys. JETP* 41: 960-965 (1975).
- [140] A. M. Campbell and J. E. Evetts, Flux vortices and transport currents in type-II superconductors, *Adv. Phys.* 21: 199-428 (1972).
- [141] S. Bhattacharya and Mark J. Higgins, Flux-flow fingerprint of disorder: Melting versus tearing of a flux-line lattice, *Phys. Rev. B* 52: 64-67 (1995).
- [142] A.E. Koshelev, Numerical simulation of thermal depinning for a two-dimensional vortex system, *Physica C* 198: 371-377 (1992).
- [143] A. V. Gurevich and R. G. Mints, Self-heating in normal metals and superconductors, *Rev. Mod. Phys.* 59: 941 (1987).

- [144] Z. L. Xiao, E. Y. Andrei, and P. Ziemann, Coexistence of the hot-spot effect and flux-flow instability in high- T_c superconducting films, *Phys. Rev. B* 58: 11185 (1998).
- [145] A. Kiliç, K. Kiliç, S. Senoussi, Grain size dependence of the current-voltage characteristics and critical current density in the self-field approximation, *J. Appl. Phys.* 84: 3254-3262 (1998).
- [146] M. Tinkham and C.J. Lobb, Physical Properties of the New Superconductors, *Solid. State Phys.* 42: 91-134 (1989).
- [147] A. Altinkök, Glassy State Behavior in Ceramic Superconductors, *Msc. Thesis*, A.I.B.U., Bolu, 28, (2004)
- [148] A. Kiliç, K. Kiliç, A. Altinkök, M. Olutaş, unpublished results.
- [149] M. Olutaş, Flux dynamics and time effects in polycrystalline superconducting MgB₂, *PhD Thesis*, A.I.B.U., Bolu, 173, (2010)
- [150] D.C. Larbalestier, L.D. Cooley, M.O. Rikel, A.A. Polyanskii, J. Jiang, S. Patnaik, X.Y. Cai, D.M. Feldmann, A. Gurevich, A.A. Squitieri, M.T. Naus, C.B. Eom, E.E. Hellstrom, R.J. Cava, K.A. Regan, N. Rogado, M.A. Hayward, T. He, J.S. Slusky, P. Khalifah, K. Inumaru and M. Haas, Strongly linked current flow in polycrystalline forms of the superconductor MgB₂, *Nature* 410: 186-189, (2001).
- [151] A. K. Elmurodov, F. M. Peeters, D. Y. Vodolazov, S. Michotte, S. Adam, F. de Menten de Horne, L. Piraux, D. Lucot and D. Mailly, Phase-slip phenomena in NbN superconducting nanowires with leads, *Phys. Rev. B* 78: 214519-214523 (2008)
- [152] A. Altinkok, H. Yetis, M. Olutas, K. Kilic, and A. Kilic, Time effects and glassy state behaviour in superconducting YBa₂Cu₃O_{7-x}, *Physica C*, 463: 371-373, (2007).
- [153] A. Kiliç, K. Kiliç, H. Yetiş, and O. Çetin, Current dependent reorganization in superconducting Y₁Ba₂Cu₃O_{7-δ}, *Eur. Phys. J. B* 46: 177-186 (2005).
- [154] W.K. Kwok, G.W. Craptree, J.A. Fendrich, and L.M. Paulius, Dynamic instabilities in the vortex lattice of YBa₂Cu₃O_{7-δ}, *Physica C* 293: 111-117 (1997).
- [155] A. P. Rassau, S. N. Gordeev, P. A. J. de Groot, R. Gagnon, and L. Taillefer, Dynamic stability of the vortex solid state of YBa₂Cu₃O_{7-δ} single crystals, *Physica C* 328: 14-20 (1999).
- [156] B. Kalisky, M. Gitterman, B. Ya. Shapiro, I. Shapiro, A. Shaulov, T. Tamegai and Y. Yeshurun, Spatiotemporal Vortex Matter Oscillations in Bi₂Sr₂CaCu₂O_{8+δ} Crystals, *Phys. Rev. Lett.* 98: 017001-017003 (2007).

- [157] D. Barness, I. Sochnikov, B. Kalisky, A. Shaulov and Y. Yeshurun, Oscillatory magnetic relaxation in $\text{Bi}_2\text{Sr}_2\text{CaCu}_2\text{O}_{8+\delta}$, *Physica C* 468, 280-283 (2008)
- [158] D. Barness, M. Sinvani, A. Shaulov, C. Trautmann, T. Tamegai, and Y. Yeshurun, Magnetic flux oscillations in partially irradiated $\text{Bi}_2\text{Sr}_2\text{CaCu}_2\text{O}_{8+\delta}$ crystals, *J. Appl. Phys.* 105, 07E310-07e312 (2009).
- [159] Hao Jin, Hai-Hu Wen, Hai-Peng Yang, Zhi-Yong Liu, Zhi-An Ren, Guang-Can Che, and Zhong-Xian Zhao, Rigid vortices in MgB_2 , *Appl. Phys. Lett.* 83: 2626-2628 (2003).
- [160] J. Dumas, C. Schlenker, J. Markus, and R. Buder, Nonlinear Conductivity and Noise in the Quasi One-Dimensional Blue Bronze $\text{K}_{0.30}\text{MoO}_3$, *Phys. Rev. Lett.* 50: 757 (1983).
- [161] R. P. Hall and A. Zettl, Role of current oscillations in ac-dc interference effects in NbSe_3 , *Phys. Rev. B* 30: 2279 (1984).
- [162] S. N. Coppersmith and A. J. Millis, Diverging strains in the phase-deformation model of sliding charge-density waves, *Phys. Rev. B* 44: 7799 (1991).
- [163] K. L. Ringland, A. C. Finnefrock, Y. Li, J. D. Brock, S. G. Lemay, and R. E. Thorne, Scaling in Charge-Density-Wave Relaxation: Time-Resolved X-Ray Scattering Measurements, *Phys. Rev. Lett.* 82: 1923 (1999).
- [164] H. F. Hundley and A. Zettl, Shapiro-step spectrum and phase-velocity coherence in NbSe_3 in a uniform temperature gradient, *Phys. Rev. B* 33: 2883 (1986).
- [165] S. N. Coppersmith and P. B. Littlewood, Pulse-duration memory effect and deformable charge-density waves, *Phys. Rev. B* 36: 311 (1987).
- [166] S. N. Coppersmith, Phase slips and the instability of the Fukuyama-Lee-Rice model of charge-density waves, *Phys. Rev. Lett.* 65: 1044 (1990).
- [167] P. Mune, E. Govea-Alcaide, R.F. Jardim, Magnetic hysteresis of the critical current density of polycrystalline (Bi-Pb)-Sr-Ca-Cu-O superconductors: a fingerprint of the intragranular and intergranular flux trapping, *Physica C* 354: 275-278, (2001).
- [168] D. Daghero, P. Mazzetti, A. Stepanescu, P. Tura, A. Masoero, Electrical anisotropy in high- T_c granular superconductors in a magnetic field, *Phys. Rev. B* 66: 184514-184523, (2002).

- [169] C.A.M. dos Santos, M.S. da Luz, B. Ferreira, A.J.S. Machado, On the transport properties in granular or weakly coupled superconductors, *Physica C* 391: 345-349, (2003).
- [170] P. Mune, F.C. Fonesca, R. Muccillo, R.F. Jardim, Magnetic hysteresis of the magnetoresistance and the critical current density in polycrystalline $\text{YBa}_2\text{Cu}_3\text{O}_{7-\delta}$ -Ag superconductors, *Physica C* 390: 363-373, (2003).
- [171] V. V. Derevyanko, T.V. Sukhareva, V.A. Finkel, Effect of an external magnetic field and a trapped magnetic flux on the current-voltage characteristics of a granular high-temperature superconductor $\text{YBa}_2\text{Cu}_3\text{O}_{7-\delta}$, *Phys. Solid State* 48: 1455-1460 (2006).
- [172] V. V. Derevyanko, T.V. Sukhareva, V.A. Finkel, Magnetoresistance Hysteresis of Granular $\text{YBa}_2\text{Cu}_3\text{O}_{7-\delta}$ High-Temperature Superconductor in Weak Magnetic Fields, *Tech. Phys.* 53: 321-327, (2008).
- [173] T.V. Sukhareva, V.A. Finkel, Hysteresis of the magnetoresistance of granular HTSC $\text{YBa}_2\text{Cu}_3\text{O}_{7-\delta}$ in weak fields, *Phys. Solid State* 50: 1001-1008, (2008).
- [174] I. S. Beloborodov, K. B. Efetov, and A. I. Larkin, Magnetoresistance of granular superconducting metals in a strong magnetic field, *Phys. Rev. B* 61: 9145 (2000).
- [175] A. Gerber, A. Milner, G. Deutscher, M. Karpovsky, and A. Gladkikh, Insulator-Superconductor Transition in 3D Granular Al-Ge Films, *Phys. Rev. Lett.* 78: 4277 (1997).
- [176] A. Palau, T. Puig, X. Obradors, E. Pardo, C. Navau, A. Sanchez, A. Usoskin, H. C. Freyhardt, L. Fernandez, B. Holzapfel, and R. Feenstra, Simultaneous inductive determination of grain and intergrain critical current densities of $\text{YBa}_2\text{Cu}_3\text{O}_{7-x}$ coated conductors, *Appl. Phys Lett.* 84: 230 (2004).
- [177] D. A. Balaev, A. A. Dubrovskii, S. I. Popkov, K. A. Shaikhutdinov and M. I. Petrov, Magnetic Field Dependence of Intergrain Pinning Potential in Bulk Granular Composites YBCO + CuO Demonstrating Large Magneto-Resistive Effect, *J. Supercond Nov. Magn.* 21: 243-247 (2008).
- [178] V. Ambegaokar and B. I. Halperin, Voltage Due to Thermal Noise in The DC Josephson Effect, *Phys. Rev. Lett.* 22: 1364-1366 (1969).
- [179] F. Zuo, X. Su, P. Zhang, J. A. Schlueter, M. E. Kelly and J. M. Williams, Effects of inhomogeneity on the interlayer magnetoresistance in the organic superconductor κ -(BEDT-TTF) $_2\text{Cu}[\text{N}(\text{CN})_2]\text{Br}$, *Phys. Rev. B* 57: R5610-R5613 (1998).

- [180] R.L. Peterson, J.W. Ekin, Josephson-junction model of critical current in granular $\text{YBa}_2\text{Cu}_3\text{O}_{7-\delta}$ superconductors, *Phys. Rev. B* 37: 9848-9851, (1988).
- [181] K.H. Muller, D.N. Matthews, A model for the hysteretic critical current density in polycrystalline high-temperature superconductors, *Physica C* 206: 275-284, (1993).
- [182] P. Mune, E. Altshuler, J. Musa, S. Garcia, R. Riera, Hysteresis in the $J_c(B_a)$ dependence of (Bi-Pb)-Sr-Ca-Cu-O polycrystalline superconductors, *Physica C* 226: 12-16, (1994).
- [183] K.Y. Chen and Y.J. Qian, Critical current and magnetoresistance hysteresis in polycrystalline $\text{YBa}_2\text{Cu}_3\text{O}_{7-x}$, *Physica C* 159: 131-136, (1989).
- [184] J.S. Xia, S.F. Sun, T. Zhang, L.Z. Cao, Q.R. Zhang, J. Chen, Z.Y. Chen, The phenomena of negative magnetoresistance and hysteresis in $\text{Bi}_{1.6}\text{Pb}_{0.4}\text{Ca}_2\text{Sr}_2\text{Cu}_3\text{O}_y$ systems, *Physica C* 158: 477-479, (1989).
- [185] Y.J. Qian, Z.M. Tang, K.Y. Chen, B. Zhou, J.W. Qui, B.C. Miao, Y.M. Cai, Transport hysteresis of the oxide superconductor $\text{Y}_1\text{Ba}_2\text{Cu}_3\text{O}_{7-x}$ in applied fields, *Phys. Rev. B* 39: 4701-4703, (1989).

CURRICULUM VITAE

Name-Surname : Atılın ALTINKÖK
Permanent Address : Abant İzzet Baysal University, Faculty of Arts and Sciences, Department of Physics, 14280 Bolu / Türkiye
Degree and date to be conferred : Ph.D., 2011
Place and Date of birth : Silivri / Türkiye, 10 January 1980
Secondary education : Silivri Lisesi, İstanbul, 1997

<u>Collegiate institutions attended</u>	<u>Dates</u>	<u>Degree</u>	<u>Date of degree</u>
Abant İzzet Baysal University, Department of Physics	1997–2001	B.S	25.06.2002
Abant İzzet Baysal University, Department of Physics	2002–2004	M.S	10.09.2004
Abant İzzet Baysal University, Department of Physics	2004–2011	Ph.D.	19.09.2011

Publications

In SCI Journals

1. A. Altinkok, K. Kiliç, A. Kiliç, H. Yetis, M. Olutas
“Transport Relaxation Measurements in Ag-Doped Superconducting Y-Ba-Cu-O” IEEE Transactions on Applied superconductivity vol 19, 2978, (2009).
2. M. Olutas, H. Yetis, A. Altinkok, A. Kiliç, K. Kiliç

- “Hysteresis Effects in Magnetovoltage Measurements in Superconducting MgB₂” IEEE Transactions on Applied Superconductivity vol 19, 2744, (2009).
3. A. Altinkok, H. Yetiş , K. Kiliç, A. Kiliç, M. Olutaş
“Slow voltage oscillations in Ag doped superconducting Y-Ba-Cu-O” Physica C 468, Issues 15-20, 1419 (2008)
 4. H. Yetiş , A. Kiliç ,K. Kiliç, A. Altinkok, M. Olutaş
“ Observation of unusual irreversible/reversible effects in a macroscopic cylindrical hole drilled in superconducting Bi-Sr-Ca-Cu-O Physica C 468, Issues 15-20, 1435 (2008)
 5. M. Olutaş, H. Yetiş, A. Altinkok, A. Kiliç, K. Kiliç
“Transport relaxation measurements and glassy state effects in superconducting MgB₂” Physica C 468, Issues 15-20, 1447 (2008)
 6. A. Altinkok, H. Yetiş, M. Olutaş, K. Kiliç and A. Kiliç
"Time effects and glassy state behaviour in superconducting Y₁Ba₂Cu₃O_{7-x}" Physica C 463, 371 (2007)
 7. H. Yetiş, A. Altinkok, M. Olutaş, A. Kiliç and K. Kiliç
"Flux Dynamics and magnetovoltage measurements in a macroscopic cylindrical hole drilled in BSCCO" Physica C 463, 445 (2007)
 8. A. Kiliç, K. Kiliç, H. Yetiş, M. Olutaş, A Altinkok, H. Sözeri, O. Çetin
“ Flux Trapping in a macroscopic cylindrical hole drilled in Bi-Sr-Ca-Cu-O” Eur. Phys. J. B, 50, 565 (2006)
 9. A. Altinkok, H. Yetiş, M. Olutaş, K. Kiliç, A. Kiliç, and O. Çetin
"Coherent Voltage Oscillations in Superconducting Polycrystalline YBa₂Cu₃O_{7-δ} " Journal of Phys. Conf. Ser. 43 698 (2006)
 10. M. Olutaş, H. Yetiş, A. Altinkok, H. Sözeri, K. Kiliç, A. Kiliç, and O. Çetin
"Flux Dynamics and Time Effects In a Carved Out Superconducting Polycrystalline Bi-Sr- Ca-Cu-O Sample" Journal of Phys. Conf. Ser. 43 631 (2006)
 11. H. Yetiş, A. Altinkok, M. Olutaş, K. Kiliç, A. Kiliç, and O. Çetin
"Magnetovoltage Measurements and Field Sweep Rate Dependence in Superconducting Polycrystalline YBCO" Journal of Phys. Conf. Ser. 43 635 (2006)
 12. K. Kiliç, A. Kiliç, A. Altinkok, H. Yetiş, O. Çetin and Y. Durust
“Time evolution of quenched state and correlations to glass effects” Physica C 420, 1, (2005).
 13. K. Kiliç, A. Kiliç, A. Altinkok, H. Yetiş and O. Çetin

"Current-induced voltage oscillations in superconducting "YBa₂Cu₃O_{7-δ}" Eur. Phys. J. B, 48, 189, (2005).

Oral and Poster Presentations

1. "I – V Curves and Time Effects in polycrystalline Superconducting MgB₂" International Symposium on Boron, Borides and Related Materials, Istanbul, TURKEY, September (2011)
2. "Voltage Oscillations in Silver Doped YBa₂Cu₃O_{7-x}" American Physical Society (APS) March Meeting, Dallas, USA, March (2011).
3. "Time Dependent Transport Properties of Superconducting MgB₂" American Physical Society (APS) March Meeting, Dallas, USA, March (2011).
4. "Time Dependent Effects in Transport Measurements and Absence of Anisotropic Behavior in Polycrystalline MgB₂", 2009 APS March Meeting, Pittsburgh, Pennsylvania, USA, March (2009).
5. "Hysteresis Effects in Ag-Doped Superconducting Y-Ba-Cu-O", 2009 APS March Meeting, Pittsburgh, Pennsylvania, USA, March (2009).
6. "New transport measurements in Ag doped Superconducting YBCO" XV. International Summer School Nicolas Cabrera 100 years of Liquid Helium, Madrid, Spain, September, (2008).
7. "Low-field Magnetovoltage Measurements in Superconducting MgB₂" XV. International Summer School Nicolas Cabrera 100 years of Liquid Helium, Madrid, Spain, September, (2008).
8. "Enhancement in flux pinning in superconducting Bi-Sr-Ca-Cu-O" Applied Superconductivity Conference, ASC 2008, Chicago, USA, August, (2008).
9. "Transport relaxation measurements in Ag-doped superconducting Y-Ba-Cu-O" Applied Superconductivity Conference, ASC 2008, Chicago, USA, August, (2008).
10. "Hysteresis effects in Magnetovoltage Measurements in Superconducting MgB₂" Applied Superconductivity Conference, ASC 2008, Chicago, USA, August, (2008).
11. "Slow voltage oscillations in Ag-doped superconducting Y-Ba-Cu-O" 20th ISS 2007, Thusukuba/JAPAN, October, (2007).
12. "Observation of unusual irreversible/reversible effects in a macroscopic cylindrical hole drilled in superconducting Bi-Sr-Ca-Cu-O" 20th ISS 2007, Thusukuba/JAPAN, October, (2007).

13. “Transport relaxation measurements and glassy state effects in superconducting MgB_2 ” 20th ISS 2007, Thusukuba/JAPAN, October, (2007).
14. “Time Effects and Glassy State Behaviour in Superconducting $\text{YBa}_2\text{Cu}_3\text{O}_{7-x}$ ” 19th ISS 2006, Nagoya/JAPAN, October, (2006).
15. “Flux Dynamics and Magnetovoltage Measurements in Macroscopic Cylindrical Hole Drilled in BSCCO” 19th ISS 2006, Nagoya/JAPAN, October, (2006).
16. “Coherent Voltage Oscillations in Superconducting Polycrystalline EUCAS' 05, Vienna Austria, September (2005).
17. “Magnetovoltage Measurements and Field Sweep Rate Dependence in Superconducting Polycrystalline YBCO” EUCAS' 05, Vienna Austria, September (2005).
18. “Flux Dynamics and Time Effects In a Carved Out Superconducting Polycrystalline Bi-Sr-Ca-Cu-O Sample” EUCAS' 05, Vienna Austria, September (2005).
19. “Organization of Flux Lines and Transport Relaxation Measurements in Polycrystalline Superconducting $\text{YBa}_2\text{Cu}_3\text{O}_{7-d}$ ” ITÜ, 12th Statistical Physics Days, Istanbul, July (2005).

Summer Schools and Workshops

1. “XV International Summer School Nicolas Cabrera 100 years of Liquid Helium”, INSTITUTO DE CIENCIA DE MATERIALES, Madrid, Spain, September, (2008).

Work Experience

2002 – Working in Abant İzzet Baysal University, Department of Physics as a research assistant.